DESIGN AND MODELING OF UHF PARTIAL DISCHARGE SENSORS: FE-BASED PD SIGNAL PROPAGATION IN HIGH VOLTAGE SYSTEMS

A Dissertation

by

AHMAD NAIF ABDELAZIZ DARWISH

Submitted to the Graduate and Professional School of
Texas A&M University
in partial fulfillment of the requirements for the degree of

DOCTOR OF PHILOSOPHY

Chair of Committee,	Haitham Abu-Rub
Co-Chair of Committee,	Hamid A. Toliyat
Committee Members,	Chanan Singh
	Robert Nevels
	Reza Tafreshi
Head of Department,	Miroslav Bigovic

December 2021

Major Subject: Electrical Engineering

ABSTRACT

The determination of whether high voltage (HV) devices suffer from high levels of partial discharge (PD) has received significant attention to ascertain the safety of neighboring utilities and achieve economic satisfaction. Such HV devices include gas-insulated switchgear (GIS), power transformers, rotating electric machines, and power transmission lines. Albeit such capital assets are rarely damaged due to their high robustness, such devices can still experience significant degradation, primarily due to PD events. Therefore, monitoring high voltage systems against PD has become of paramount significance. This has contributed to developing a plethora of PD-based detection techniques, including acoustics, optical, electromagnetic (using Ultra-high frequency sensors and high-frequency current transformers), and chemical techniques.

The recent advances in ultra-high frequency-based (UHF) techniques have led to the utilization of such techniques in PD detection for many high voltage devices like GIS, transformers, and power cables. This is attributed to the superior immunity and high sensitivity of UHF techniques in detecting, localizing, and classifying different PD defects. UHF detection was predominantly concerned with implementing antennas or sensors to detect PD activities and localizing PD defects based on the time-of-flight (ToF) or the time-difference-of-arrival (TDoA) in GIS and power transformers. The work done hitherto covered either simplified models of disconnecting parts inside GIS enclosures or addressed a single disconnecting part at a time. This work, on the other hand, analyzes EM waves due to multiple disconnecting parts simultaneously.

First, this work utilizes CIGRE sensitivity verification recommendations to overcome the treeing issue associated with partial discharge and properly analyze EM waves inside two different GIS structures. A $145kV$ L-structured GIS model was implemented in COMSOL multi-physics, and EM wave propagation has been analyzed. Moreover, a $550kV$ Siemens π model GIS has also been implemented and analyzed. The obtained results have been compared with experimental results to verify the model's accuracy. It has been shown that GIS systems are very complex structures for propagating electromagnetic waves due to the multiple barriers existing within such devices.

Hence, many reflections and signal attenuation are experienced by electromagnetic waves.

Then, a disk-cone (DISCONE) planar class of antennas has been optimized, implemented, and tested against partial discharge. A size-reduction technique, which utilizes the structural symmetry of the antenna, has also been proposed and discussed to reduce the cost of implementation and improve the antenna's directivity. The experimental results largely agree with the simulation results verifying the modeling accuracy. A maximum gain of $6.25dBi$ has been achieved using the proposed antenna, and 47% size-reduction has been accomplished without significant performance degradation. After testing the antenna performance, the device has also been tested against PD activities within ceramic insulators and induction machines. The obtained results show that the antenna can be used to obtain different PD signatures, and hence, PD defect classification can be easily performed.

DEDICATION

To my beloved parents,

Gentle and strong souls who taught me to always trust Allah, unbounded love and support at every single stage of my life, and limitless inspiration to be self-assuredness

&

To my Siblings

This humble work is a sign of my love to you!

ACKNOWLEDGMENTS

First and foremost, I would like express my highest appreciation to Allah, the most Gracious, the most Merciful, for providing me with the patience, strength, and belief to successfully complete this long-lasting journey.

I would like to express my gratitude to my advisors, Professor Haitham Abu-Rub and Professor Hamid Toliyat for the support and guidance throughout my Ph.D. studies. Their tireless efforts, valuable insights, high commitment to excellence on research, and the several invaluable opportunities given to me helped me out to reach my goals. They gave me the full freedom to explore my own ideas which have helped developing an independent researcher which can tackle and solve real-life problems.

My special thanks go to Professor Robert Nevels for his unbounded support throughout my graduate studies. He has always been available and happy to help me in exploring the different aspects of UHF detection techniques. His suggestions has also helped me to improve the achieved outcomes during my graduate studies. I also would like to express my appreciation to Dr. Chanan Singh and Dr. Reza Tafreshi for giving their valuable time to be part of my committee. I highly appreciate their feedback and valuable comments and suggestions.

Next, my thanks goes to Dr. Shady Khalil for his continuous support and guidance which helped achieve my goals. Special thanks also goes for my old colleague and friend, Yousuf Abo-Rahama who have always been glad to help me strengthen my knowledge in antenna design. His outstanding suggestions, continuous support, and deep fundamental understanding to the microwaves and antennas fields have saved me limitless time. I am also thankful to my collegue, Fransisco Espinal who helped me in the testing of the proposed UHF antenna, which comprise a significant part of my PhD thesis.

The completion of this work would not have been possible without the help and support from Professor Ayman El-Hag who helped me test the UHF sensor in an actual high voltage environment in the University of Waterloo. Also, Special thanks go to Dr. Graeme Coapes from Siemens who

provided me with actual GIS data to verify the accuracy of the implemented FE models.

My life as a graduate student has been enriched by my fellow graduate students from which I learnt a lot. I would like to express my appreciation for Anas Karaki, Saad Muaddi, Mohamed Massoudi, Qasim Khan, Faisal El-Ghannam, Farid Naghavi, Bryton Praslicka, Mesaad Albader, Shima Hasanpour, Dorsa Talebi, Ajay Kumar Morya, Yuming Chen, and Amir Negahdari.

I would like to express my thanks to the department of Electrical and Computer engineering faculty and staff. The world-class education I received from the courses I took have definitely helped me not only in completing the PhD work, but also in strengthening my knowledge in a plethora of different fields.

CONTRIBUTORS AND FUNDING SOURCES

Contributors

This work was supervised by a dissertation committee consisting of Professor Haitham Abu-Rub, who served as an advisor, Professor Hamid A. Toliyat, who served as a co-advisor, Professor Robert Nevels, and Professor Chanan Singh of the Department of Electrical and Computer Engineering, as well as Professor Reza Tafreshi of the Department of Mechanical Engineering.

The work summarized in Section 4 was completed by the student in collaboration with Dr. Graeme Coapes from Siemens who provided the experimental data. The work presented in Section 5 and Section 6 were completed by the student in collaboration with Dr. Ayman El-Hag of the Department of Electrical and Computer Engineering in the University of Waterloo. All other work for the dissertation was completed by the student under the advisement of Professor Haitham Abu-Rub and Professor Hamid A. Toliyat of the Department of Electrical and Computer Engineering.

Funding Sources

The work done in this dissertation was made possible in part by funding from QNRF under grant number [10-0101-170085]. The statements made herein are solely the responsibility of the author. This work was also supported in part by Siemens, UK, and Texas A&M Engineering Experiment Station (TEES).

NOMENCLATURE

GIS	Gas-Insulated Switchgear
UHF	Ultra-high Frequency
EM	Electromagnetic
ANN	Artificial Neural Networks
RF	Random Forest
AdaBoost	Adaptive Boosting
FFT	Fast Fourier Transform
SVM	Support Vector Machine
PD	Partial Discharge
HV	High Voltage
MV	Medium Voltage
TE	Transverse Electric
TM	Transverse Magnetic
TEM	Transverse Electromagnetic
SF_6	Sulfur HexaFluoride
GTEM	Gigahertz Electromagnetic Test Cell
CPW	Co-Planar Waveguide
FMP	Free Mean Path
TEV	Transient Earth Voltage
FEA	Finite Element Analysis
FDTD	Finite Difference Time-Domain
HPLC	High Performance Liquid Chromatography

DGA	Dissolved Gas Analysis
BT	Bush Type
MT	Metal Flange Type
PCA	Principal Component Analysis
RFE	Recursive Feature Elimination
AF	Antenna Factor
DE	Double Exponential
μ	Material Permeability
ϵ	Material Permmitivity
A	Magnetic Potential
E	Electric Field Intensity
σ	Material Conductivity
c	Speed of Light
v	Propagation Velocity
f_c	Cutoff Frequency
S	Poynting Vector
Q	Total Charge
P	Radiated Power
p	Electric Dipole Moment
V	Electric Potential
Z_0	Characteristic Impedance
k	Wavenumber
n	Normal Unit Vector
α	Number of Ionizing Collisions
N_e	Total Number of Electrons

N_{ec}	Total Number of Liberated Electrons

TABLE OF CONTENTS

Page

LIST OF FIGURES

FIGURE Page

LIST OF TABLES

TABLE Page

1. INTRODUCTION

As per the "IEC," partial discharge (PD) can be defined as a localized dielectric breakdown in a portion of a solid, fluid, or gaseous insulator. Such breakdown takes place when the electric field stress across an insulator exceeds the dielectric strength of the insulator, partially bridging the gap between the electrodes [1]. Different medium voltage (MV) and high voltage (HV) power equipment have different PD defects. These defects can be classified based on the location of occurrence as corona discharge, surface discharge, and internal discharge. Corona discharge occurs in the presence of sharp edges or coarse surfaces of electrodes in MV or HV equipment. The existence of corona discharge contributes to the enhancement of electric field at these tips due to the accumulation of charges. Surface discharge arises when current flows through a conductor due to a high voltage difference between two electrodes. When the current flows along with one of the electrodes, charges might accumulate at the sharp edges, causing a breakdown on the surface of the insulator [2]. Internal discharge usually takes place inside oil-filled MV and HV power devices. Such discharge usually occurs due to small cavities inside the insulation material [2, 3].

1.1 Problem Statement

With the rapid development of UHF-based detection techniques in PD applications over the past few decades, a deeper understanding of the generated electromagnetic (EM) wave behavior due to PD is demanded to better accommodate and utilize UHF sensors for PD detection. This gives rise to questions such as: What is the impact of different disconnecting parts, or barriers, in GIS on the propagating EM waves due to PD? Are there any other low-cost yet wideband UHF sensors that can efficiently detect, localize, and classify PD defects? Would it be possible to apply any techniques to reduce the size of existing sensors without significant degradation of the sensors' performance? In this work, finite element analysis (FEA) is used to model a GIS and investigate the impact of EM wave behavior in such a device due to PD. On the other hand, disk-cone (Discone) antennas have been utilized for PD applications. To the best of the author's knowledge, utilizing

such antennas for PD applications has not yet been covered. The planar Discone antenna proposed in this work has been reduced in size using the structural symmetry of the antenna.

In this thesis, accurate FE models for different GIS structures, including L-Structures and extended-T (or π-structures), are built and analyzed. Models' results are initially compared with existing analytical and experimental data to verify the modeling accuracy. Then, an extensive EM wave propagation analysis is carried out to improve the utilization of UHF antennas in detecting PD activities within such capital assets. On the other side, a new class of CPW-fed annular monopole antennas to detect PD activities is proposed and analyzed. A size-reduction technique has been proposed to reduce the sensors' size by 47% without degrading the performance of the sensors. Finally, classical machine learning algorithms are used to classify different classes of PD defects in ceramic insulators. The impact of 2 dimensionality-reduction techniques, namely PCA and RFE, is presented and discussed.

1.2 Motivation

Thus far, around 85% of the seldom recorded GIS failure is attributed to the phenomenon of PD. GIS devices are costly systems usually designed and built to operate for over 25 to 30 years. Thus, when implemented, careful management and continuous monitoring to avoid any potential factors contributing to the failure of such capital assets are of paramount significance. Protecting GIS devices against PD activities has been given great attention for decades.

Many endeavors have been recently carried out to build FE and FDTD models to improve PD detection techniques in GIS devices. Most existing models are, nonetheless, using a simple dipole to model the PD current pulsation. Such a model does not take into account the known treeing effect associated with PD activities. In this work, CIGRE sensitivity verification recommendations are utilized to overcome the treeing problem.

Finally, UHF-based detection techniques are amongst the most commonly known and used techniques in PD detection. This is attributed to the high sensitivity and low noise of such techniques. Nonetheless, the lightweight constraint imposed on some antennas makes it challenging to use UWB, high gain antennas such as horn, and log-periodic antennas for general purpose PD

detection. To illustrate, PD detection of ceramic insulators in overhead transmission lines requires the use of lightweight antennas that can be easily carried and placed next to the insulators to monitor such devices against PD activities. The use of heavy antennas for such an application might not be feasible. Thus, this work proposes a planar antenna (CPW fed Monopole Antenna) to detect PD activities for overhead transmission lines. The proposed antenna size has also been reduced by around 47% without degrading the antenna performance. The proposed reduced-size antenna has a UWB, high directivity, and high gain based on the obtained simulated and experimental results.

1.3 Novelty

- Modeling GIS enclosures using FEA to understand and analyze EM wave behavior due to different disconnecting parts such as disconnecting switches, L-structure, extended-T structures, and relative angle between PD source and sensors.

- Utilizing CIGRE sensitivity verification recommendations (CSVR) as a mean of analyzing EM wave behavior rather than as a sensitivity testing method. CSVR have been utilized in this work to inject PD-like pulses into the GIS and overcome the treeing effect of PD pulses which cannot be easily modeled.

- Optimizing Dicone antennas (which have already been used in wireless communication applications) to operate over the UHF range to utilize them for PD applications.

- Utilizing the structural symmetry of the Discone antenna to reduce its size without a major degradation on its performance.

- Investigating the impact of different dimensionality reduction techniques such as PCA and RFE on different classification metrics of different ceramic insulators' PD defects.

1.4 List of Research Items

1.4.1 Patent

1. A. darwish, S. Refaat, H. Abu-Rub, and H. A. Toliyat, “CPW-Fed Annular Monopole Antenna for Partial Discharge Detection,” PCT patent filed (11/05/2020), QF Ref 2019-062-02.

1.4.2 Peer-reviewed Journal Articles

1. A. Darwish *et al.* “PD Signal Attenuation in 550 kV GIS: Impact of Different Barriers on the Propagation of Electromagnetic Waves” (Submitted).

2. A. Darwish *et al.* “A Size Reduction Methodology for Structurally Symmetrical PD-Based Wideband UHF Antennas” (Submitted).

3. Q. Khan, S. S. Refaat, H. Abu-Rub, H. A. Toliyat, M. Olesz and A. Darwish, "Characterization of Defects Inside the Cable Dielectric With Partial Discharge Modeling," in IEEE Transactions on Instrumentation and Measurement, vol. 70, pp. 1-11, 2021, Art no. 3502911, doi: 10.1109/TIM.2020.3027925.

4. A. Darwish, S. S. Refaat, H. Abu-Rub and H. A. Toliyat, "PD Signal Propagation in GIS: Ultra-High Frequency Detection-Based Modeling," in IEEE Sensors Journal, vol. 20, no. 16, pp. 9417-9426, 15 Aug.15, 2020, doi: 10.1109/JSEN.2020.2988840.

5. A. Darwish, S. S. Refaat, H. A. Toliyat and H. Abu-Rub, "On the Electromagnetic Wave Behavior Due to Partial Discharge in Gas Insulated Switchgears: State-of-Art Review," in IEEE Access, vol. 7, pp. 75822-75836, 2019, doi: 10.1109/ACCESS.2019.2921089.

1.4.3 Conference Proceedings

1. A. Darwish, A. H. El-Hag, S. S. Refaat, H. Abu-Rub, H. A. Toliyat, “Impact of RFE and PCA Dimensionality Reduction Techniques on the Classification of Ceramic Insulators PD Defects,” CEIDP, 2021 (Accepted).

2. A. Darwish, S. S. Refaat, H. Abu-Rub and H. A. Toliyat, "Partial Discharge Signal Propagation in Three-Phase Gas-Insulated Switchgear: CIGRE Recommendations-Based Analysis," 2020 IEEE Energy Conversion Congress and Exposition (ECCE), Detroit, MI, USA, 2020, pp. 5091-5097, doi: 10.1109/ECCE44975.2020.9236286.

3. . M. Massaoudi, A. Darwish, S. S. Refaat, H. Abu-Rub and H. A. Toliyat, "UHF Partial Discharge Localization in Gas-Insulated Switchgears: Gradient Boosting Based Approach," 2020 IEEE Kansas Power and Energy Conference (KPEC), Manhattan, KS, USA, 2020, pp. 1-5, doi: 10.1109/KPEC47870.2020.9167534.

4. A. Darwish, A. H. El-Hag, S. S. Refaat, H. Abu-Rub, H. A. Toliyat, “PD Signal Propagation Delay in Gas Insulated Switchgear,” ISE, 2019.

5. D. Nascimento, S. S. Refaat, A. Darwish, Q. Khan, H. Abu-Rub, and Y. Lano, “Impact of Void Size and Location on XLPE Cables on the Event of Partial Discharge,” 2019 Workshop on Communication Networks and Power Systems (WCNPS), 2019.

6. O. Abu-Rub and A. Darwish, "Partial Discharge Localization in Gas-Insulated Switchgear using Various Learning Algorithms," 2019 2nd International Conference on Smart Grid and Renewable Energy (SGRE), Doha, Qatar, 2019, pp. 1-6. **(Best Paper Award)**

7. A. Darwish, S. S. Refaat, H. Abu-Rub, H. A. Toliyat and Q. Khan, "Partial Discharge Signal Propagation in T-Structured GIS," 2019 IEEE Conference on Electrical Insulation and Dielectric Phenomena (CEIDP), Richland, WA, USA, 2019, pp. 632-636.

2. LITERATURE REVIEW *

2.1 On the Electromagnetic Wave Behavior Due to PD in Gas-Insulated Switchgears: State-of-Art Review

The rapid growth of gas-insulated switchgear as a compact, efficient, and reliable device has recently been given great attention. Albeit gas-insulated switchgear can seldom suffer from failure due to its high resiliency and robustness, some severe damages have been experienced by such devices, mainly because of partial discharge. Thus, monitoring such accidents has become a vital part of power reliability. The ultra-high frequency techniques have recently shown superior performance in detecting and classifying electromagnetic waves produced by partial discharge. This is mainly due to the excellent immunity to the noise of the ultra-high frequency detection techniques compared with the very-high frequency counterparts. This chapter of the thesis highlights the mathematical aspects of the electromagnetic waves generated by partial discharge. It also delivers an overview of the electromagnetic wave behavior in the complex structure of gas-insulated switchgear and outlines the essential characteristics of the internal and external partial discharge detection methods using ultra-high frequency techniques.

2.1.1 Introduction

The determination of whether power utilities suffer from high levels of PD is an essential factor contributing to the safety of neighboring utilities, economic and customer satisfaction, and the avoidance of regulatory fines. Thus, careful management of such capital assets has become an essential objective for different power firms [4]. PD occurs when the electric field stress inside an insulator exceeds its breakdown strength due to the high applied voltage. Ionization of atoms could take place, producing a high-frequency transient current inside the insulation material [5], [6]. Even though PDs might be initially very small, the generated current pulsations might

*Part of this chapter is reprinted with permission from "On the Electromagnetic Wave Behavior Due to Partial Discharge in Gas Insulated Switchgears: State-of-Art Review" by A. Darwish, S. S. Refaat, H. A. Toliyat and H. Abu-Rub, 2019. IEEE Access, copyright [2021] by IEEE.

gradually cause insulators' chemical decomposition, causing erosion with time. Eventually, the moving charges might bridge between the two electrodes connecting the insulator. This can cause a complete breakdown or failure of the device. Different PD sources take place inside an insulator, including but not limited to overvoltage, lightning strikes, aging, and internal manufacturing defects [7].

Different medium voltage (MV) and high voltage (HV) power equipment have different classes of PD defects. These defects can be classified as corona discharge, surface discharge, and internal discharge. Corona discharge occurs in the presence of sharp edges or coarse surfaces of electrodes in MV or HV equipment. The existence of corona discharge contributes to the enhancement of the electric field at these tips. It initiates a dramatic stress increase on the insulation material. On the other hand, Surface Discharge arises when current flows through a conductor due to a high voltage difference between two electrodes. When the current flows along with one of the electrodes, charges might accumulate at the sharp edges, causing a breakdown on the surface of the insulator. An essential factor that contributes to the event of surface discharge is that the insulation material has to have higher permittivity than the surrounding material [2]. Internal discharge usually takes place inside oil-filled MV and HV power devices. Such discharge usually occurs due to small cavities inside the insulation material with weaker dielectric strength and lower permittivity than its surroundings. Consequently, the stress caused by the electric field is more substantial around the cavity, causing ionization and breakdown of the dielectric material. Another common discharge type is caused by floating metals inside Gas-Insulated Switchgear (GIS) systems. The behavior of this type of defect is similar to that of corona discharge since the working principle is similar. When small metallic particles are located inside a GIS, charges will accumulate at the tip causing enhancement of the electric field, which might, as a consequence, cause PD [2, 3].

GIS devices are made up of an inner high voltage conductor, an insulator (usually Sulfur Hexafluoride (SF6)), an outer tank, and other high voltage components, including switches, transformers, and circuit breakers. SF6 has been widely used in many gas-insulated types of equipment due to its high insulation properties and breakdown voltage stress. The latter property is coming from

the fact that SF6 is an electronegative material that can easily capture low-energy electrons [8]. Moreover, such gaseous material could be used to detect the different types of PDs based on the characteristic of the generated decomposed materials. A review paper on the detection of PD type based on the decomposition of SF6 has been published in [9].

GIS is widely used in power system utilities because of the high reliability, safety, robustness, environmental aspects, and reduced space [10, 11]. Such devices have been commercially introduced in the 1970s and are widely used in substations. Many GIS systems are getting aged nowadays, and the need to mitigate their failure has recently become of paramount importance for developers. Maintenance facilities have shifted from time-based monitoring to condition-based monitoring, where different diagnostic techniques for the detection of different defects such as PDs are used [12, 13]. Around 85% of the failures of HV and MV equipment are mainly attributed to PDs [14]. This highlights the significance of giving PD analysis more attention to improving power reliability. The most common types of defects found in GIS includes protrusions, floating metals, particle on a spacer surface, and void on a solid spacer [14, 15].

Different offline and online non-conventional techniques have been developed to detect and localize PD in the last few decades. Such techniques include chemical, acoustic, optical, and electrical methods. These techniques are developed based on the formation of ozone, emission of acoustic waves, production of light due to ionization, and the radiation of electromagnetic (EM) waves, respectively. Each of the techniques mentioned above has its benefits and drawbacks. Chemical techniques, which can be either offline or online, rely on collecting products or gases emitted due to the PD defect. Two different methodologies are widely used for chemical detection: high-performance liquid chromatography (HPLC) and dissolved gas analysis (DGA). Chemical methods suffer from the lack of localization of the defect despite their high sensitivity. Moreover, it does not work appropriately unless a sufficient amount of expelled products or gases are collected, increasing the required detection time [16]. Acoustic techniques are mainly online techniques. They locate PDs based on the acoustic signal amplitude and phase delay. This method relies on detecting mechanical waves produced by the rapid energy release due to the vaporization

of the insulating materials. The main disadvantage of this method is that it might give a false location for PD defects due to the interferences from the environment [17, 18]. Optical techniques, which are also mainly online techniques, show superior performance in PD detection and localization since they have excellent immunity to various electromagnetic interferences coming from the environment. Optical techniques rely on intrinsic interferometers. Nevertheless, such techniques suffer from random polarization causing fringe fading issues [17, 19].

Electrical techniques are widely used and depend on non-invasive methods. Non conventional electrical methods can be classified into two main categories, namely the usage of high-frequency current transformer (HFCT) and Ultra-High Frequency (UHF) sensors. The two techniques are usually classified as online techniques. HFCTs are devices capable of detecting the current pulses using inductive coils along with ferromagnetic cores. Such devices are widely used to detect PD in cables by connecting the HFCT around the grounding cable. They are used to detect signals with a frequency spectrum of around 3MHz to 30MHz. The main drawback of the use of HFCT is the fast attenuation of high-frequency signals due to the low pass filtering behavior of cables [20]. UHF techniques, which are based on detecting signals covering frequencies from 0.3GHz to 3GHz, are widely used in detecting PD in GIS devices. In such devices, when a PD occurs, EM waves will be radiating due to the acceleration and deceleration of charges. Such EM waves contain the Transverse Electro-Magnetic (TEM) mode as well as other higher-order modes of propagation [20].

Collinson and Jennings also proposed a third electrical technique to overcome some of the drawbacks associated with the UHF, HFCT, and the conventional PD measuring techniques [21]. The basic idea of the technique, called Transient Earth Voltage (TEV), is that an induced pulse-like EM wave is to be generated at the metallic tank of GIS in the event of PD. Thus, the usage of a non-intrusive sensor mounted on the outer surface of the GIS tank is possible. Nevertheless, such a technique suffers from the high external noise collected with the produced EM waves due to PD [21].

Understanding the behavior of the emitted EM waves in GIS is problematic since the GIS pro-

vides a highly complex structure to the propagating signals. This is mainly due to the multiple resonances created inside the GIS tank in addition to the different discontinuity types [22]. Although electrical techniques have relatively good immunity to noise, they have a limited ability to locate the exact position of PD [23].

2.1.2 Partial Discharge Mechanisms and Models in GIS

2.1.2.1 Partial Discharge Mechanisms

In GIS, the phenomenon of partial discharge is mainly governed by two mechanisms, namely Townsend and Streamer. Depending on the size of the discharge, either Townsend or both mechanisms governs the PD phenomenon. For any of the mechanisms above to occur inside a GIS, an ionized electron exists between any two electrodes with a potential difference. Electron ionization could be defined as releasing an electron from a molecule producing a positive ion and a negative ion. Many factors could cause the ionization process to take place including, but not limited to light exposition, thermal effects, or solar radiations [24].

- **Townsend Mechanism**.

When free electrons reside between an anode and a cathode, an electric field is applied at the free electrons forcing them to accelerate towards the anode due to the applied force based on coulomb's formula. Due to this force, the electrons start to gain kinetic energy while moving between the two electrodes. If electrons collide with some other atoms with enough kinetic energy, new ionized electrons are released, leaving positive ions. Due to this process, the number of electrons reaching the anode is larger than the number of liberated electrons at the cathode. Hence, the electric current starts to increase [24]. If the temperature is fixed, the electron's accumulation is proportional to the applied electric field and the free mean path (FMP). FMP is defined as the effective distance an atom can travel between 2 consecutive collisions and is inversely proportional to the pressure [25].

Under the applied electric field, electrons will be moving towards the anode. They leave positive charges behind, forming an avalanche. The positive ions will be accelerating towards the

opposite side (the cathode) but at slower velocities than electrons since they are heavier in weight. When the positive ions reach the cathode and collide with it, new moving electrons will be generated. The total number of electrons excited due to the Townsend mechanism is:

$$N_e(x) = N_{ec}e^{\alpha x}, \tag{2.1}$$

where N_e is the total number of electrons located at a distance x from the cathode, N_{ec} is the number of liberated electrons in addition to the generated electrons due to the bombardment of positive ions with the cathode, and α is the Townsend first ionization coefficient. α could be defined as the number of ionizing collisions that can take place during the movement of an electron [25], [26]. It is a strong function of the applied electric field, and its value is usually obtained experimentally. Figure 2.1 shows the Townsend mechanism due to the excitation of an initial electron located at the cathode $(x = 0)$, which traveled a distance d to reach the anode. The total number of electrons that reaches the anode is $e^{\alpha d} - 1$ new electrons (excluding the originally excited electron) based on (2.1).

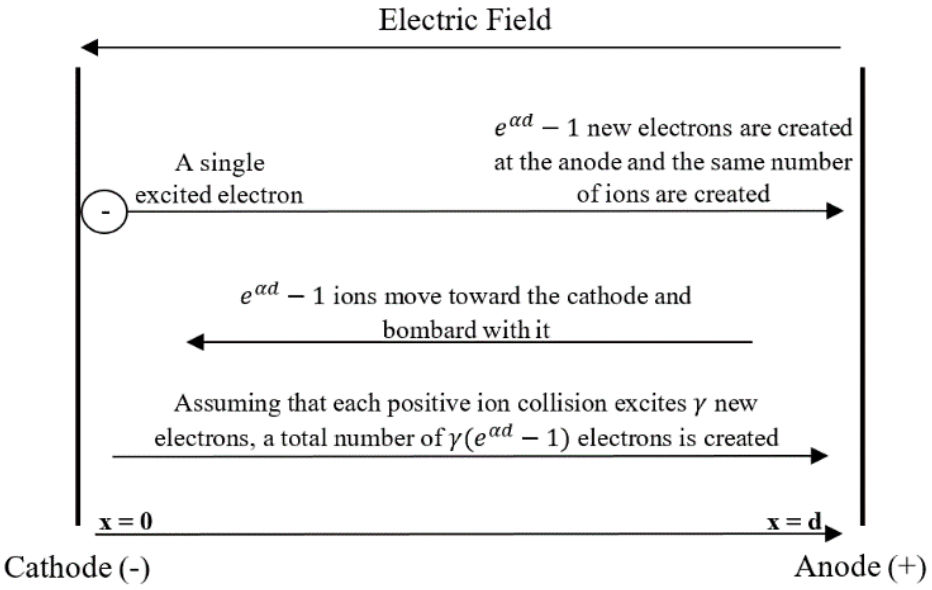

Figure 2.1: Summary of Townsend mechanism process.

- **Streamer Mechanism**.

When gaps between electrodes get larger, the Townsend mechanism can no longer explain the behavior of the avalanche, and the breakdown is not attributed only to the ionization process. However, there is also the space charge and the formulation of photons. When avalanche breakdown takes place in large gaps or voids, positive and negative charges distort the electric field forcing electrons to move towards the tip of the avalanche, and positive ions towards the tail [27]. In addition, the created photons enhance the discharge phenomenon by imposing new electrons to produce new avalanches ahead of the original one. The Streamer mechanism can be divided into three subcategories based on the gap length, namely Streamer inception, Streamer propagation, and Leader propagation. If a sufficient number of electrons are excited due to ionization, space charge, and photoionization, Streamer inception occurs. The field, in this case, is weakly non-uniform. On the other hand, Streamer propagation takes place when the gap gets larger. The most important characteristic of this type is that the field is strongly inhomogeneous. Finally, Leader propagation usually takes place when the gap gets very large [25] – [28]. No further details on the categories of Streamer mechanism are given in this chapter, but readers can refer to [25] – [28] for more details.

Protrusion defect is one of the most common types of defects found in GIS devices. In [29], a finite difference time domain (FDTD) model for the protrusion defect has been proposed as a relatively long needle with a very sharp tip to improve the electric field intensity. Consequently, the avalanches are formed at the tip, as shown in Figure 2.2. When the voltage applied at the needle is positive, electrons in the avalanche are concentrated at the non-uniform electrode, whereas the positive ions are on the other side. This distribution makes the effective gap length looks smaller since the positive ion concentration looks like an extension to the non-uniform electrode. Thus, lower voltage is required for the flashover [26]. A similar concept could also be applied to the floating metal since charge concentration will be higher at the sharp tips of floating metals. For the case of floating metals, the PD will have a sharper pulse, and broader frequency spectrum based on an experiment carried out in [30].

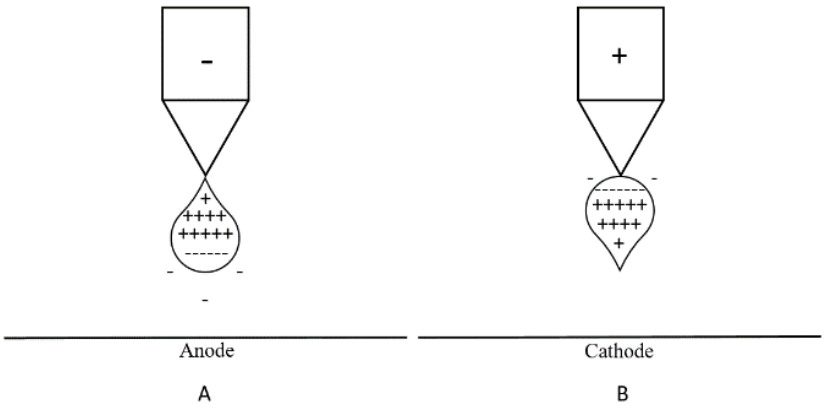

Figure 2.2: Arc modeling for non-uniform gaps (protrusion defect model). A) negatively charged protrusion B) positively charged protrusion.

2.1.2.2 Partial Discharge Models

PD measurements have been widely used to assess the different power equipment and components, including power transformers, cables, and switchgear devices. During the event of PD, electrons experience acceleration and deceleration. This behavior results in electromagnetic wave radiation, as will be discussed in section 2.1.3. Inside the complicated structure of GIS, EM waves experience high degrees of reflections and attenuation [22]. Consequently, the EM waves travel along with the GIS in multiple paths, making it difficult to predict the exact behavior of such signals.

Different types of defects generate different PD pulses. Nevertheless, most of these generated pulses have a short time-domain representation. Such pulses have a relatively large bandwidth because of the inverse relationship between time domain and frequency domain representation of a signal, as shown in Figure 2.3 [4, 2, 31]. Although the Gaussian pulse with larger width initially has higher spectral energy than its counterpart, the spectral intensity started to attenuate at a lower frequency, as depicted in Figure 2.3(b).

PD pulses could mainly be modeled using one of the following equations [32]:

- Gaussian pulse:

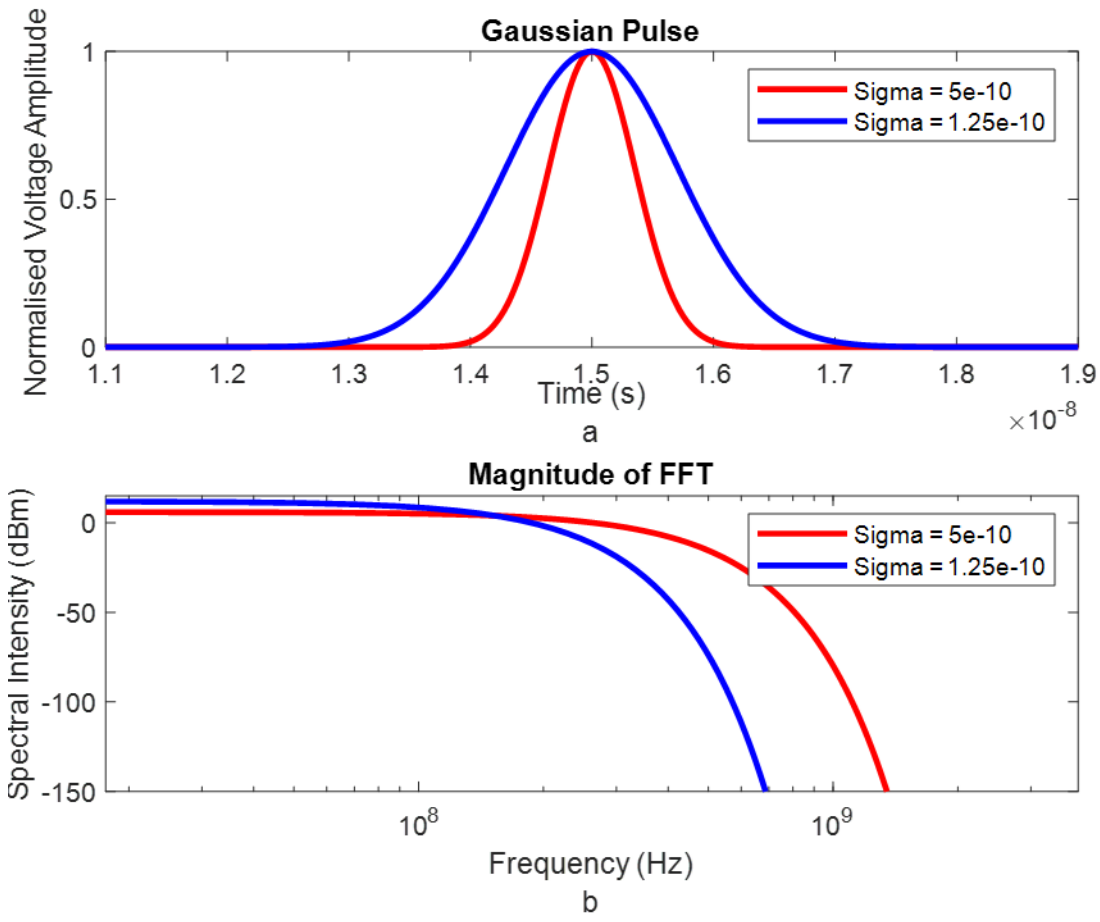

Figure 2.3: a) Time domain and b) frequency domain representation of a Gaussian pulse.

$$G_0(t) = I_0 e^{\frac{-t^2}{2\sigma}}, \tag{2.2}$$

where I_0 is the pulse amplitude, σ is a parameter that determines the pulse width. Equation (2.2) can also be represented as [29]:

$$G_1(t) = I_0 e^{-\frac{(t-b)^2}{c^2}}, \tag{2.3}$$

where b is the center of the pulse, and c is used to determine the width of the pulse.

- Wanninger pulse:

$$W(t) = \frac{I_0}{T} e^{-\frac{(1-t)}{T}}, \tag{2.4}$$

where T is used for the determination of the pulse width.

- Double exponential pulse:

$$DE(t) = I_0[(1+\alpha t)^{-\alpha t} - (1+\beta t)^{-\beta t}], \tag{2.5}$$

where α and β are constants used to determine the shape of the pulse. Figure 2.4 shows an example of the three pulses.

PD due to a defect in a GIS cannot be modeled as a simple hardwiring since the wavelength of the UHF EM waves can be comparable to the size of the equipment. Thus, modeling the PD defect

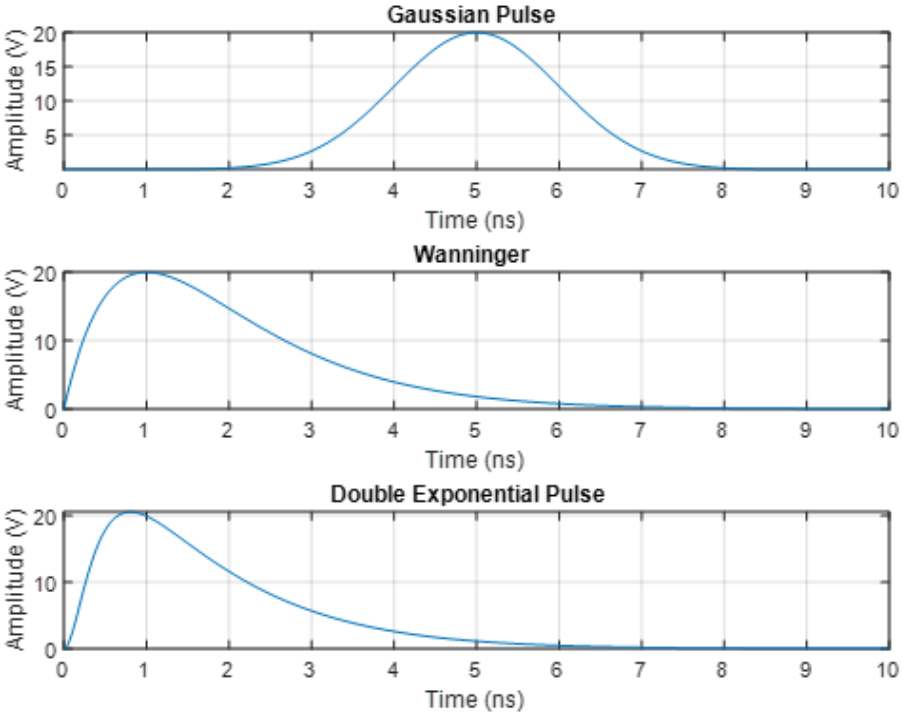

Figure 2.4: a) Gaussian pulse, b) Wanninger pulse, and c) Double exponential pulse.

as a dipole antenna can provide a better approximation since the gap size is usually much smaller than the size of the equipment [33].

2.1.3 Electromagnetic Wave Radiation due to Partial Discharge

The phenomenon of partial discharge is responsible for the emission of electromagnetic waves as it imposes electrical forces on electrons. The main goal of this section is to elucidate the radiation action of EM waves due to partial discharge.

2.1.3.1 Electromagnetic Wave Radiation due to a Point Charge and the Larmor's Formula

Static charges can either act as sources or sinks for the electric field. Nevertheless, they do not emit EM waves because no magnetic field is created when there is no flowing current [34]. Moreover, charged particles moving at a constant velocity do not radiate EM waves in the radial direction away from the charge [2]. An essential condition for the radiation of the electromagnetic waves is the decaying behavior of the EM energy, which has to be a function of the squared of the distance from the source to satisfy the Poynting vector [35].

On the other hand, the acceleration and deceleration of charged particles emit EM waves. Consider a positively charged particle that starts accelerating in SF6 from rest at point X until it reaches point Y. Then, the particle stays at a constant velocity, as shown in Figure 2.5. When the charged particle is at point X, or an arbitrary point after point Y, no EM waves will be emitted, as mentioned earlier. On the other hand, while the particle is accelerating, the electric field lines will experience a 'kinking' effect to maintain the continuity condition of the electric field (since the electric field is due to the same charge). The formed 'kinks' create disturbance in the emitted field, causing radiation. The radiation is a consequence of the E_r component of the kinked electric field shown in Figure 2.5. It should be noted that there is no E_r field component along the direction of motion, which explains why no EM waves are radiating along the direction of motion. With the assumption that the charged particle is moving at a constant velocity after point Y, the electric and magnetic fields radiation are given by [36]:

$$\mathbf{E}_t = \frac{Q\mu_0}{4\pi}\frac{a\sin(\theta)}{\rho} = \frac{Qa\sin(\theta)}{4\pi c^2 \rho \epsilon_0}, \tag{2.6}$$

$$\mathbf{H}_t = \frac{Q}{4\pi c}\frac{a\sin(\theta)}{\rho}, \tag{2.7}$$

where Q is the charge of the particle, a is the retarded acceleration, c is the speed of light, θ is the

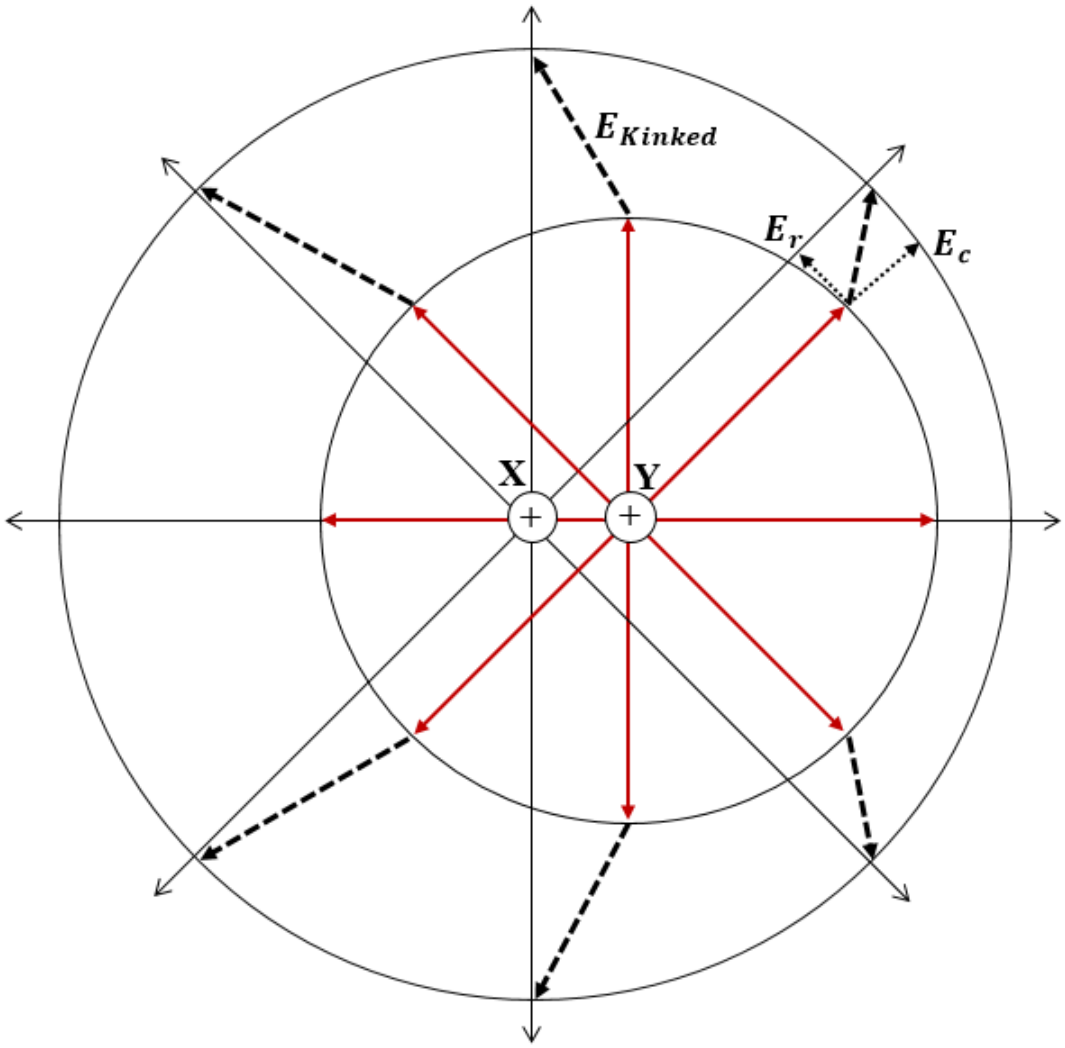

Figure 2.5: EM wave radiation due to an accelerated charge.

angle between the acceleration direction and the observation point, μ_0 is the permeability of air, and ρ is the distance traveled by the electric field after some time (t). It should be noted that μ_0 is used since the permeability of air and SF_6 are identical from the practical point of view. The radiated electric field behavior of an accelerated charge is similar to that of a dipole based on (1.6) and (1.7). That is, the radiation pattern of accelerated or decelerated particles could be modeled as a donut, or toroidal radiation pattern [35]. The Poynting vector could be directly computed using **E** and **H** as:

$$\mathbf{S} = \mathbf{E}_t \times \mathbf{H}_t = \epsilon_0 c \mathbf{E}_t^2 = \frac{Q^2 a^2}{16\pi^2 \epsilon_0 \rho^2 c^3} \sin(\theta) \tag{2.8}$$

where ϵ_0 is the permittivity of air. Finally, the loss in the total energy can be found by integrating **S** over all directions. This would give the Larmor's Formula which is given by:

$$P = \frac{Q^2 a^2}{6\pi c^3 \epsilon_0} \tag{2.9}$$

where P is the total radiated power during to an accelerated/decelerated charged particle [37].

2.1.4 Electric Dipole Model of Short Gaps

When an insulating void defect exists inside the spacer of a GIS, the electric dipole moment is created. The creation of dipoles is attributed to the fact that a small distance separates charges of opposite directions. Indeed, the apparent charge detected using the conventional methods is not the actual charge (Q) but instead, it is related to Q.d, where d is the gap length.

The electric dipole can radiate electromagnetic waves based on the Hertz vector, and the electric field is given by [38, 39]:

$$\mathbf{E}_x = \frac{\mu_0 p}{2\sqrt{2e}\pi^{1.5} t_0^2 D} f\left(\frac{t - \frac{y}{c}}{t_0}\right), \tag{2.10}$$

where $f\left(\frac{t-\frac{y}{c}}{t_0}\right) = \sqrt{2e}\left(\frac{t-\frac{y}{c}}{t_0}\right) e^{-((t-y/c)/t_0)^2}$, $p = Q.d$ is the electric dipole moment, t_0 is a constant that depends on the Gaussian pulse width, D is the distance between the dipole and the origin, and e is the electron charge. Equation (2.10) shows that the radiation field intensity is inversely

proportional to the pulse width. Moreover, the radiated EM wave is a function of time and a single coordinate component.

2.1.5 Electromagnetic Wave Behavior inside GIS Enclosures

Insulation spacers and screws were used in the past to connect the compartments of GIS. Thus, the outer tanks of GIS do not provide perfect grounding for EM waves since tanks are not perfect coaxial waveguides. In the event of PD, such configuration would result in leakage of EM waves outside the tank [10]. The apertures act as slot antennas allowing the electric field to propagate outside the tank at resonance frequencies. Recently, the use of basin-type insulators with an outer metallic cover is prevalent. Such spacer type provides better grounding for the GIS tank, prevents spacer corrosion with air, and reduces EM waves from leaking outside the tank in the event of PD [10, 40].

A GIS is a complex structure with many different structural components that can affect the EM waves propagating inside the tank. Those discontinuities include ground switches and disconnectors, spacers, L-shaped and T-shaped sections, and sudden changes in the inner and/or outer conductor diameter(s). In PD, the relative angle between the PD source and the antenna placement affects the EM wave behavior. Understanding the impact of the discontinuities mentioned earlier on EM waves has thus become of paramount importance, especially if the UHF techniques are used in the detection of PD events [22].

2.1.5.1 Relative Angle between PD Source and Antenna Position

A detailed mathematical derivation for the EM wave behavior due to PD has been carried out in [41]. The intensity of the electric field inside a simple GIS with no discontinuities depends on the dimensions of the coaxial waveguide, the magnitude of the PD, and the angular position between the PD source and the sensor. The angular position affects the higher-order modes but has no impact on the transverse electromagnetic (TEM) propagation mode. TEM mode due to PD is maximum at the inner conductor and decays as we move towards the outer conductor. On the other hand, the electric field intensity of the higher-order modes approaches a minimum when the angle

between the source and the probe approaches 90°. In contrast, it is maximum when the angle is 0° [42, 43]. Moreover, the time-domain representation of the detected signal is not a Gaussian pulse as the case of the PD source. This is since the field undertakes an infinite number of paths to reach the sensor, and a small portion of the wave moves directly from the source to the sensor [41].

The impact of probes placement inside GIS tanks through the finite difference time domain (FDTD) has been extensively studied [44]. Probe couplers are sensors modeled to obtain the voltage amplitude inside the GIS enclosure. This is done by modeling each probe as a matched load with a certain length to a 50-ohm coaxial line. The probe was initially inserted at four different locations along the radial axis ($\theta = 0$), as shown in Figure 2.6. The best allocation for the probe is near the outer tank to ensure enough voltage difference between one end of the probe and the other. Moreover, suppose the transverse magnetic (TM) mode of propagation is of interest. In that case, the probe must be placed parallel to the longitudinal axis (z-axis) of the GIS since the electric field will have a component along that direction.

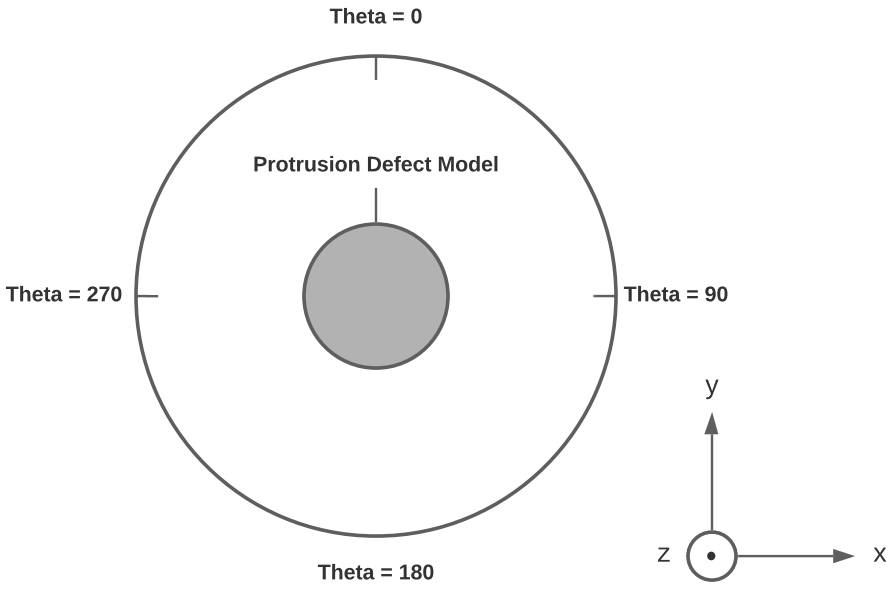

Figure 2.6: 2-D cross-section of a GIS model with protrusion defect.

2.1.5.2 L Junction

Reflections due to the radiation of EM waves during PD can largely affect signal behavior. One of the biggest obstacles to such propagating waves is the L structure. Such discontinuities disturb the phases of the EM waves, causing mode transformations under some circumstances. Different modes of EM waves experience the following transformation [45, 46]:

- If the input mode of propagation is TEM, Transverse Electric (TE21) will be created at the second port after the L-section (weakly since most of the TEM mode maintain its shape).
- If TE11 is the input, most of the signal will be reflected back in the case of horizontal excitation, and TE21 will be obtained at the output in case of vertical excitation.
- If TE21 is at the input port, TE11 is obtained at the output.

On the contrary, it has been shown in [47] that TEM mode experiences no conversion. This is attributed to the fact that the distributed constant circuit handles such waves, and thus, no conversion takes place. At the point of the L-intersection, an infinite number of modes will be generated. However, after few wavelengths, the low-frequency components retain their original characteristics. An increase in the peak electric field intensity might be experienced before the L-intersection because of the multiple reflections created by the discontinuity [47].

The impact of the L-section on the high-frequency components of EM waves has been investigated by building a 252kV GIS model and studying the effect of the L intersection on the electric field propagating in different directions [48]. PD has been excited along the radial direction, and hence, the electric field intensity is maximum along that direction. After the L structure, the electric field experiences significant attenuation due to the TE mode's reflections. Along the longitudinal direction, TM mode of propagation is detected. The L discontinuity acts as a source for TM mode, allowing it to propagate to the second part of the tank since such a mode allows the electric field to propagate in the longitudinal direction [49]. Some experimental works that were recently conducted verified that the TM mode components of the EM wave propagate after the L intersection, whether disconnecting switches are kept open or closed [50].

Finally, the effect of the L-section on the TEM and TE modes has been investigated to observe the impact of the L-structure on the low frequency and high-frequency components separately [51]. Again, the TEM mode is not largely affected by the L intersection, whereas most reflections are attributed to the TE11 mode of propagation. Moreover, the work also shows that the peak voltage right before the L section is higher than the straight GIS tank case. This is attributed to the superimposition of the reflected components of the TE11 on the incoming signals due to PD, which increases the field intensity, and thus, the detected voltage [51].

2.1.5.3 T Junction

The need to study EM waves under the influence of T structure is essential since such structures are commonly found in GIS devices. An extensive study on the effect of T structures on the low and high-frequency components of the signal propagation was carried out in [52]. EM wave behavior due to PD inside a T tank depends on the port at which the PD was generated. Figure 2.7 shows a simplified T-shaped GIS model. If the PD is generated at port 1, the high-frequency components of the detected signals at port 2 are higher than that at port 3. The experimental results show that the transmission rate of the high-frequency EM waves is about 20-30% at port 3 and about 40-50% at port 2 relative to port 1. On the contrary, TEM mode components propagate based on the distributed constant circuit. It has been experimentally shown that the transmission rate at both ports is about 60%. The transmission rate was computed based on the distributed circuit theory, and 66.67% of the signal was supposed to be transmitted, which is slightly higher than the measured value since attenuation is not considered in the theoretical calculations [52]. On the other hand, if the PD is generated at port 3, the signal would be divided equally between the other 2 ports [53].

Moreover, the propagation behavior of EM waves in the x, y, and z directions shown in Figure 2.7 is investigated to provide a better understanding of the EM signal propagation [54]. A protrusion defect is modeled as a small needle placed along the y-axis close to port 1, and a pulse is applied to the needle. The electric field intensity is dominant in the y-direction, and results show that the straight section (SS) has a greater intensity than the T section (TS). Moreover, the electric field intensity in the x-direction is minimal. The relative angle effect is also studied by investigat-

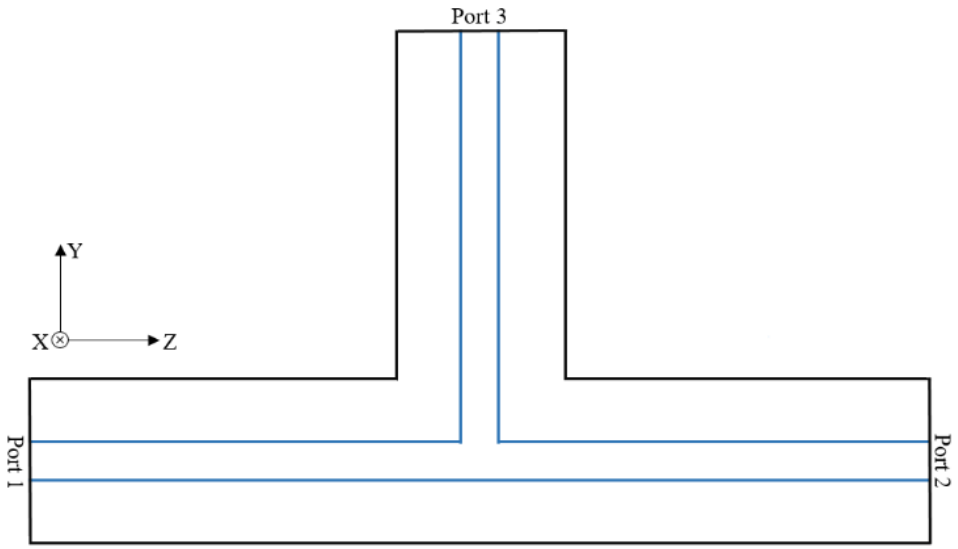

Figure 2.7: A simplified T-Shaped gas-insulated switchgear model.

ing the propagation characteristic of EM waves inside a T-shaped GIS in different circumferential angles using FDTD [55]. Figure 2.8 and Figure 2.9 summarize the attenuation characteristics measured at two different circumferential angles for both SS and the TS. As shown in Figure 2.8 and Figure 2.9, the dominant direction is always the radial direction, and the T branch energy is always higher than that of the straight branch along the z-direction since the discontinuity acts as a source to the TM mode of propagation.

The time of flight through a T structure is mainly dependent on the PD source location relative to the inner or outer conductor [56]. To illustrate, if the PD source is close to the outer tank, results might not be very accurate compared with the theoretical calculations of the time of flight. This is because a different path for the wave will be taken if the PD source is generated close to the outer tank. Finally, mode transformation also takes place in T-structures since higher-order modes are also created at the discontinuity [57, 58, 59]. Therefore, the following rules are obtained for the case where PD source is generated at port 1 (refer to Figure 2.7):

- If the input is TEM mode, the output at ports 2 and 3 are TE21.
- TE11 transforms to TE21.

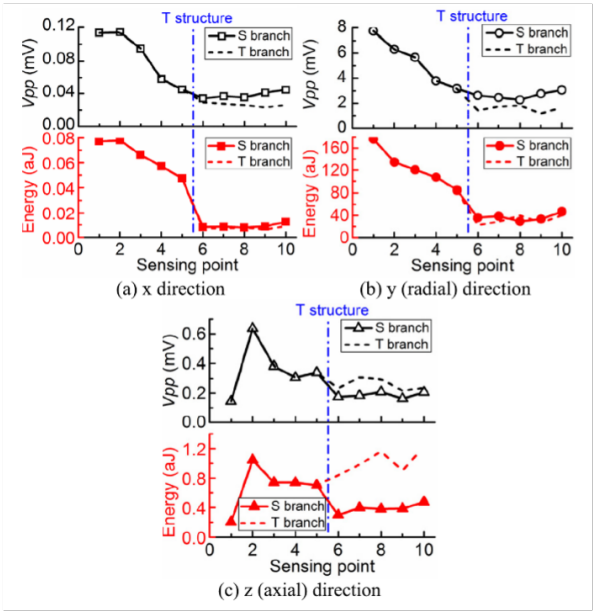

Figure 2.8: Attenuation curves for peak voltages and energy $\theta = 0$ "reprinted from [55]".

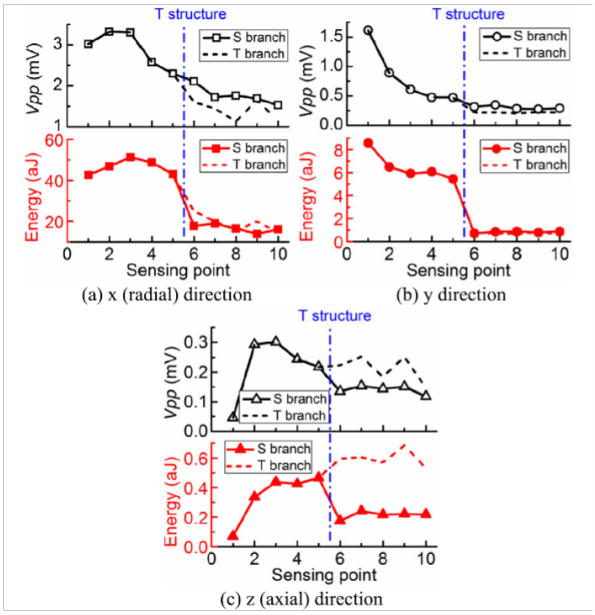

Figure 2.9: Attenuation curves for peak voltages and energy $\theta = 90$ "reprinted from [55]".

- TE21 retain its mode at both ports if the excitation is in the 45° direction. Otherwise, TE21 changes to TE11 at port 3.

If port 3 is the input of the PD source, a similar mode transformation will be obtained at port 1 and port 2. S. Okabe *et al.* [60] modeled a T section GIS and applied a protrusion defect at port 3 shown in Figure 2.7. The following are obtained (holds under the assumption that the cutoff frequency includes TE21 modes):

- If TEM mode is at the input, TE21 (0 degree) will be the dominant mode at the outputs.
- If TE11 (0 degree) is at the input, it will mostly retain its mode at the outputs.
- If TE11 (90 degrees) is at the input, TE21 (45 degrees) will be the dominant mode at the outputs.

2.1.5.4 Disconnecting Parts and Change of Diameters Ratio

Circuit breakers, switches (disconnectors), and isolators are some of the standard components comprised in GIS tanks. Such components can affect the propagation of EM waves. A GIS in the simplest form can be thought of as a coaxial cable that supports TEM and other higher-order modes [61, 62]. Nevertheless, suppose a disconnecting component of the GIS is opened for any reason. In that case, the propagating EM waves can no longer consider the GIS as a coaxial cable, but rather, it is seen as a circular waveguide (CW). CW cannot support the TEM mode of propagation since they are made of a single conducting material, and thus, a potential difference between 2 conductors cannot be achieved to get the TEM mode [61].

Solving the Helmholtz equation for E-field, the following two equations for TEM and the TE modes are obtained:

$$\frac{1}{r}\frac{\partial}{\partial r}(r\frac{\partial V}{\partial r}) + \frac{1}{r^2}\frac{\partial^2 V}{\partial \phi^2} = 0, \tag{2.11}$$

$$\frac{1}{r}\frac{\partial}{\partial r}(r\frac{\partial V}{\partial r}) + \frac{1}{r^2}\frac{\partial^2 V}{\partial \phi^2} + \frac{\partial^2 V}{\partial z^2} = -k^2 V, \tag{2.12}$$

where (2.11) is the E-field for TEM and (2.12) is the E-field for the TE mode. In these 2 equations, r, ϕ, and z are the coordinates of the cylindrical system, V is the potential function, and k is the propagation constant. It can be seen that TEM mode does not have a longitudinal component (z-direction), and the velocity of the wave is not frequency-dependent. On the contrary, TE (and TM) mode has cutoff frequencies below which waves cannot propagate [63]. The cutoff frequencies for the TE and TM modes of coaxial waveguides are calculated using the following equations [64]:

$$f_c^{\mathrm{TE}m1} = \frac{vm}{\pi(a+b)}, \tag{2.13}$$

$$f_c^{\mathrm{TM}1n} = \frac{vm}{2(b-a)}, \tag{2.14}$$

where a and b are the inner and outer radii of the coaxial cable, respectively, and m and n are integers to determine the mode of operation for the TE and TM modes, respectively.

FDTD model for a GIS with SF6 gas being in inserted series with the high voltage conductor as shown in Figure 2.10 is built [65] to understand the effect of disconnecting switches. Both high-frequency (HF) and low-frequency (LF) components were measured and simulated separately through filters. The couplers connected after the switch (UHF B, C, and D) could not detect most electromagnetic waves LF (TEM) components. EM waves can no longer see the GIS in this case as a coaxial cable, but rather a CW which does not support TEM mode of propagation [65, 66]. In addition, results show that if the gap length is increased, more TEM frequency components would be attenuated, resulting in higher energy losses. High-frequency components (TE11 mode and above), on the other hand, do not experience significant attenuation in magnitude since they can freely propagate in circular waveguides.

The effect of disconnecting switches was further studied in [64]. This is done by investigating the impact of the switch for three different classes of GIS (110kV, 220 kV, and 550kV). It has been shown that the higher is the voltage (or the larger is the GIS dimensions), the lower the attenuation of EM waves due to disconnecting switches becomes. This could be justified by the fact that the

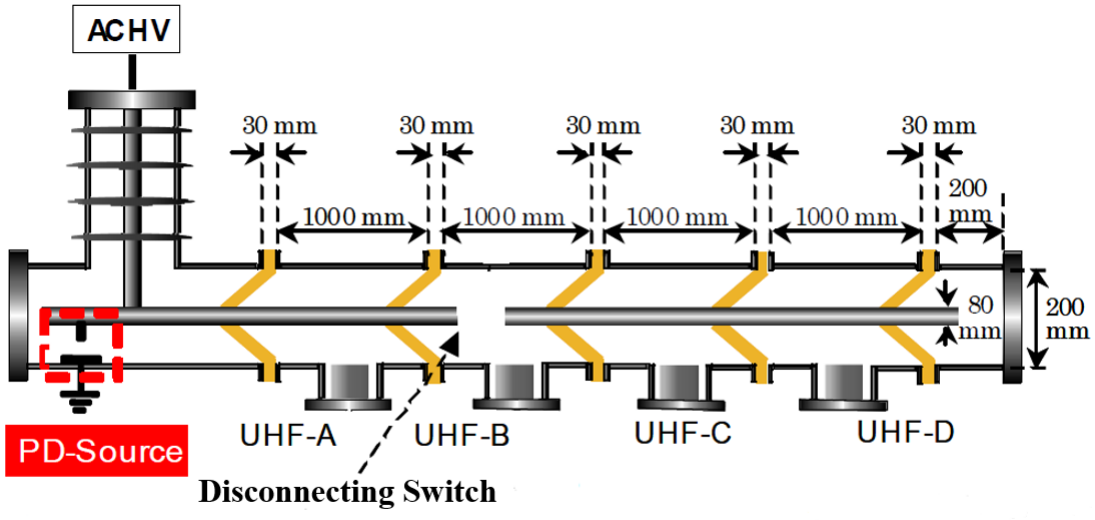

Figure 2.10: Gas-insulated switchgear model with a disconnecting switch being opened "adapted from [65]".

larger the dimensions of the GIS, the lower the cut-off frequency of the first propagating mode, the lower the TEM content, the lower the reflections due to the low order modes.

The impact of changing the diameter ratio between the inner and outer conductors was also investigated in [64]. The work has shown that EM wave energy is attenuated after the change in inner radius. Such results are expected since changing the ratio between the inner and outer conductor radii changes the characteristic impedance of the coaxial waveguide. The characteristic impedance of a lossless line is given by [67]:

$$Z_0 = \frac{60}{\sqrt{\epsilon_r}} \ln\left(\frac{a}{b}\right), \tag{2.15}$$

where a and b are the inner and outer radii of the coaxial cable, respectively.

Further investigation on the change of outer diameter was carried out in [68]. The results showed that the TEM mode of propagation experiences a minute impact due to a change in diameter, whereas the higher-order modes are reflected.

2.1.5.5 Insulating Spacers

Dielectric spacers are solid insulating components used to separate GIS compartments and provide better support between inner and outer conductors [69, 70]. However, such components enforce some constraints on the highest possible applied voltage between the two conductors of the GIS at the interfaces between the solid, gas, and electrode interface [71]. Many attempts have been proposed to optimize the shape of dielectric spacers and reduce the electric field stress, thus increasing the breakdown voltage of the GIS. Consequently, different types of insulations are proposed including, but not limited to disk type, cone type, and basin type spacers [69, 72].

To understand the impact of dielectric spacers on the generated EM waves in the event of a fault, an experimental investigation to study and analyze the intensity of the detected field after passing through basin-type insulators was carried out in [9, 73]. FDTD modeling was also used to investigate the effects of spacers further. Two types of basin-type spacers were used to analyze the impact of EM waves. As depicted in Figure 2.11, the metal type has a metallic cover surrounding the spacer to reduce the electric field leakage and provide better grounding for the tank. In contrast, the bush type does not have any metal cladding.

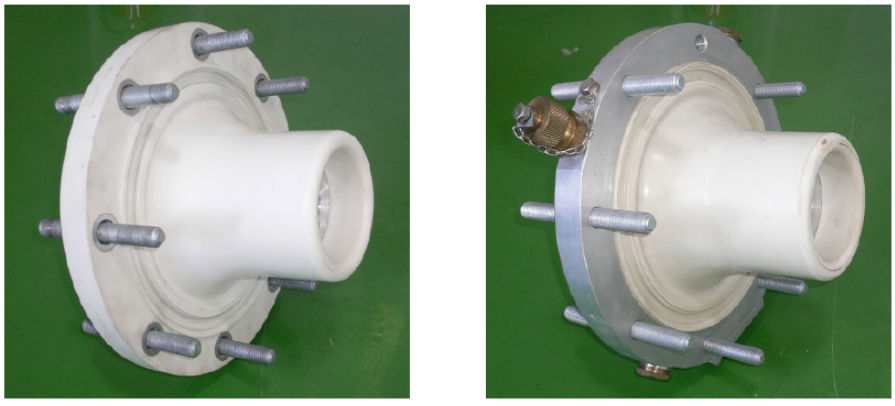

(a) Bush type (BT) (b) Metal flange type (MT)

Figure 2.11: Basin-Type Insulating Spacers "reprinted from [73]".

The main factor contributing to EM attenuation is not the permittivity difference between SF6 and the dielectric spacer. This has been investigated by initially applying low pass filtering to the EM wave to inspect the attenuation of the TEM mode of propagation [9, 73]. The results showed that the low-frequency components experienced a minimal attenuation in the amplitude as the signal propagated through the spacers. When high-pass filtering is applied to the obtained EM waves, the higher-order propagation modes experienced a considerable attenuation. As the EM wave propagates inside the tank, the higher-order modes start to decompose since different propagation modes have different velocities at which they travel. Hence, a reduction in the amplitude of the signal is experienced even in the absence of dielectric spacers [73].

A simulation model has been built to investigate the effect of the spacers on the time of flight of EM waves [74]. The simulation model results showed that EM waves could not propagate at the speed of light with the existent of spacers. The speed of propagation is inversely proportional to the square root of the relative dielectric constant [52]. Thus, the propagation with dielectric spacers with high relative permittivity would be slower than the speed of light. The results of the work also showed that EM waves traveled through the path with minimal resistance. Thus, the thickness of the spacer is the main factor that affect the velocity of the EM waves rather than its shape.

2.1.6 UHF Sensor Connection

2.1.6.1 Externally Connected UHF Sensors

Albeit internally connected UHF sensors demonstrate superior performance compared with the externally connected counterparts in both noise and sensitivity, the latter has been given much attention. This is attributed to the many challenges associated with the connection of internal sensors in already built GIS devices since such systems are concealed devices, imposing high cost and time for the integration of sensors internally [75].

For bush-type spacers, EM waves can leave the tank through the dielectric spacer [7]. S. Kaneko et al. [76] built an FDTD model for a GIS with slits formed by the bolts connecting the GIS tubes. For the induced EM waves, the slits act as slot antennas with a width equal to

the thickness of the spacer and length equal to the spacing between 2 adjacent bolts. This gives the externally connected sensors an advantage if the measured frequency of the PD event is close to the resonance frequencies of the slot antennas [75, 77]. The detected electric field intensity is maximum if the UHF is connected in the middle between 2 adjacent bolts [75, 76]. For the electric field vector to meet the boundary conditions at the aperture, the field lines have to be in the longitudinal direction parallel to the GIS tank. Thus, when connecting an external antenna to detect the produced EM waves due to PD, the E-plane of the sensor has to be fixed parallel to the GIS tank to maximize the sensitivity of the detected electric field [39, 75].

Different kinds of external sensors are used to detect the event of PD. The most commonly used types are the bi-conical log periodic antenna, Horn antenna, loop antenna, a dipole antenna, and some kinds of planar antennas, including fractal antenna, patch antenna (asymmetric and symmetric), and spiral antenna [7, 39, 75, 78, 79]. Horn antennas have higher sensitivity at high frequencies, whereas log-periodic antennas have better sensitivity at low frequencies. Loop antennas have better sensitivity at the higher frequency side of the spectrum. One of the factors that make such antennas superior compared with the other two types mentioned above is that the position of the loop antennas does not have to be precisely in the middle between bolts to get high sensitivities. Dipole antennas, conversely, have the best sensitivity as they can be directly connected to the flanges measuring both field intensity and the potential difference between the 2 flanges in the event of PD [75]. Microstrip patch antennas are small, narrow bandwidth, and cheap devices printed into a circuit board and made with a conductive material such as copper [80, 81]. Spiral antennas are a wideband circularly polarized type of antennas with a relatively low gain [82, 83]. Fractal antennas are small, multiband, broad bandwidth antennas. Although Hilbert fractal antennas are the most commonly used type of such antennas, there are also some other types like the Moore fractal antenna [78, 84, 85].

2.1.6.2 Internally Connected UHF Sensors

Recently, GIS devices are built with UHF sensors integrated internally to detect PD properly. Such sensors are usually connected in the hand-hole of GIS tanks. Consequently, there are restric-

tions on the maximum size of the internally connected antennas. Another drawback of the use of such devices is that they affect the electric field distribution inside the GIS tank [86, 87]. Moreover, if maintenance is required for one of the UHF sensors in the event of failure, changing internally connected sensors or fixing them requires more effort and time [7].

The position of the PD source can affect the behavior of the detected electric field by sensors. To illustrate, if the PD source is close to the inner conductor, TE11 mode of propagation is dominant, and thus, the detected EM wave would have a short duration. On the contrary, if the defect is on the outer tank, higher-order TE modes would be generated, increasing the duration of the detected signals [88, 89]. The increase in duration is caused by the reduction in the velocity of the higher-order modes of propagation which is given by the following equation for TE modes:

$$v_{\text{TE}} = v\sqrt{1 - \left(\frac{f_c}{f}\right)^2} \tag{2.16}$$

Where f_c is the cutoff frequency of the TE mode and f is the operating frequency. An important point to note is that if the GIS size is small, it might be difficult to differentiate whether the PD source is on the low or the high voltage conductor [88]. When the GIS size is small, the tip of the needle used to create the protrusion defect would be close to both the inner and outer conductors making it challenging to determine whether the needle is on the inner or outer conductor.

Due to the size constraint imposed on the internally connected UHF sensors, limited types of such devices could be used to detect PD. Disk type and loop type sensors are the most well-known sensors used for this purpose. The performance of the two types of UHF couplers or antennas were investigated [89]. Results show that disk-type sensors have better sensitivity for the detection of higher-order modes. Thus, if PD took place near the outer tank, disk-type sensors demonstrate superior capabilities. On the other hand, loop-type antennas are suitable at lower order frequencies, making them good candidates if PD occurred near the central conductor. Disk type antennas can either be connected internally or externally [86, 90, 91]. Extensive research has been carried out to improve disk-type antennas' performance for the detection of UHF signals. To summarize, internally and externally connected sensors deliver similar behavior for the detection

of PD [9]. However, the internally connected sensors have much higher sensitivities compared with the external counterparts [92].

2.1.7 Overview of Electromagnetic Wave Behavior in GIS

Tables 2.1 and 2.2 summarize some of the important electromagnetic aspects investigated by researchers during the event of PD in GIS.

2.2 CIGRE Sensitivity Verification Recommendations and UHF Sensitivity Analysis

The determination of whether GIS suffers from PD has been given great attention since the earliest days to contribute to such capital assets' operational safety and reliability. Traditionally, it has been proven that only apparent PD charge magnitude can be measured. Thus, no complete information about PD events can be obtained using conventional PD measurement techniques [93, 94]. Different techniques have been deployed to improve the detection and localization of PD in GIS enclosures. Among these, UHF techniques have been in use since the 1980s as they showed great suppression to noise and high sensitivity [95, 96, 97]. UHF detection techniques have been widely used for PD detection, classification, and localization of different PD defects in different high voltage equipment [98, 99]. The major drawbacks of such a technique are the limited information about the exact magnitude of PD charges since there is no direct correlation between the received RF signal strength and the PD intensity, and the difficulties associated with the installation of UHF sensors in some devices like transformers and built GIS systems [95, 99].

To overcome the issue of limited information about the magnitude of PD charge, CIGRE sensitivity verification procedure was developed and used to allocate UHF sensors in GIS enclosures optimally [95, 100]. The sensitivity verification procedure has two steps: laboratory test (step 1) and on-site test (step 2). In step 1, a transmitting antenna injects an artificial pulse similar in behavior to the actual PD pulse. The resultant electromagnetic (EM) waves are then acquired using a second receiving sensor. Such analysis is used to obtain the frequency response of UHF sensors and establish PD charge sensitivity. On the other hand, the 2^{nd} step is done on-site while GIS systems are operating to ensure that the obtained sensitivity is sufficient to detect PD during the

Table 2.1: Impact of Disconnecting Parts on EM Wave Propagation

Reference	Discontinuity Type	Utilized UHF Sensor	Covered Frequency Band	Remarks
[9] [40]	No Discontinuities	Fat Dipole (Dissymmetric) Antenna Connected Externally	0.5GHz – 3GHz	• Two types of excitations were used to model the PD accurately. Linefeed to model the TEM mode and waveguide feed to model the higher order modes. • With the use of external sensors, the cut off frequency of leaked signal is determined by rectangular waveguides. • Linear antennas placed along the axis which is parallel to the GIS is the optimal way for maximum detection efficiency.
[11] [73]	Basin-Type Spacers	- Disk Type UHF Sensors - Horn Antenna Connected Externally	Time Domain Results only	• The obtained results show that the transmission rate percentage inside the GIS is always higher when using the metal type insulating spacer if the same fault type is applied. • The use of internal and external sensors gave similar behavior with the exception that the detected field intensity is larger with internal sensors.
[22]	L-Section and T-Section	Disk-Type UHF Sensors	0-3GHz	• A Finite Element (FE) model that assumes perfect conductors and a non-dispersive insulating spacers is built in this work. • The results show that coupling is low at low frequencies and is high at high frequencies. This is explained by the fact that many sharp edges and resonances will be created at the high frequencies causing S-parameters to have such a behavior.
[33]	Bus Bar	Ideal Probes	0-3GHz	• A near field to far field transformation model has been built to study the EM wave propagation due to a PD. The obtained results were verified with the use of numerical solver, and results with high accuracy were obtained. • Insulation material can have a large impact on the low frequency components. • Bus-bar have a minimal effect on the EM waves because its size is much smaller than the wavelength.
[44]	No Discontinuities	Probe Coupler	0 – 3.5 GHz	• The longer the distance between the source of PD and the coupler, the weaker the detected electric field intensity due to dispersion effect. • When the angle between source and probe is 90 (Fig. 5), only even-number TE modes are detected in the frequency domain since TE odd modes have nodal points of intensity strength.
[46]	L-Section/ Spacer	Ideal Sensing Probes (Simulations only)	0.3 – 1 GHz	• As the distance between the consecutive spacers is increased, more resonances occur. • As the number of spacers is increased, more resonances takes place due to the increased reflections between the spacers. • TE11 mode causes the largest portion of reflection at the L-intersection.
[47]	L-Section	Ideal Sensing Probes (Simulations only)	0 – 2 GHz	• L-section caused a large reduction in the amplitude of the higher order modes. • L section causes mode transformation to EM waves propagating inside GISs.
[48]	L-Section	Ideal Sensing Probes	Time Domain Results only	• TM mode can pass through an L-intersection since the electric field in such mode can travel in the longitudinal direction.
[52]	T-Structure	Disk-Type Sensors	Time Domain Results only	• Low frequency components can propagate as in distributed circuit model, whereas TE modes experience reflections and attenuation. • Experiments performed in 2 different types of GISs to verify the obtained conclusions.
[54]	T-Structure	UHF Probes	-	• Most of the field along the y-direction (Fig. 6) will propagate to the SS. • Field along the x-direction is negligible. • Field along the z-direction mostly propagates along the TS (The TS could be thought of as a source to the TM mode of propagation).
[55]	T-Structure	Ideal Sensing Probes	0-3.5GHz	• The frequency domain spectrum shows peaks at cutoff frequencies corresponding to the different modes in all directions. In the x-direction and y-direction, the peaks appear at the different TE modes whereas TM mode peaks appear in the z-direction (Fig. 1.7).

Table 2.2: Impact of Disconnecting Parts on EM Wave Propagation (contin.)

Reference	Discontinuity Type	Utilized UHF Sensor	Covered Frequency Band	Remarks
[57]	T-Structure	Disk-Type Sensors	0.35GHz-0.75GHz	• For the case where the used cut off frequency is below the TE21 frequency bands, TE11 behaviour of T-structure is similar to that of L-structures. It should be noted that the magnitude of the transformed modes might not be the same.
[60]	T-Structure and L-Structure	UHF Sensor	-	• If TE11 was incident at an oblique angle (that is, an angle other than 0 or 90 degrees), the characteristics of the propagated field can be obtained by the superposition of the 2 aforementioned types. • Electromagnetic wave modes inside a straight GIS are preserved. Thus, one can utilize this property to distinguish between noise and generated signal due to PD inside the tank.
[64]	Disconnecting Switch and Change in Radius	Ideal Sensing Probes External Sensors	0-2GHz	• The effect of increasing and decreasing the inner radius of the GIS were similar as expected (refer to (15)). • The energy of the EM waves right before the change in characteristic impedance due to increasing/decreasing the radius is usually high due to the reflections at that point.
[65]	Disconnecting Switch	Disk-Type UHF Sensors	0-8GHz	• When disconnecting switches are open, multiple reflections on the EM waves could occur causing the peak voltage to increase before the switch (Sensor A in Fig. 9).
[75]	Spacers	Horn Antenna Dipole Antenna Loop Antenna Log-Periodic Antenna	0-3GHz	• The proposed improved dipole antenna showed superior sensitivity for voltage detection (2 times larger than the horn antenna). This could be attributed to the fact that the proposed sensor was directly measuring the potential between the 2 tubes connected via the spacer. • Noise issue could be reduced if the measured frequency band is limited to a relatively narrow band which contain the resonance frequency of the slot antenna(s).
[76]	Spacers	-	0-1.2GHz	• As the number of bolts used to connect GIS tubes increases, the number of slots also increase, increasing the resonance frequency. • Increasing the width of the slots increase the bandwidth of the antenna. • As the dielectric constant increases, the resonant frequency decreases.
[78]	-	Moore Fractal Antenna Hilbert Fractal Antenna	0-3GHz	• Both Hilbert and Moore fractal antennas have high directivity. • Moore fractal antenna has higher sensitivity and better waves reception compared with the Hilbert counterpart.
[85]	-	Stacked Hilbert Antenna Hilbert Antenna	0-1GHz	• Stacked Hilbert antenna has superior performance compared with the conventional Hilbert antenna in gain and Bandwidth. • The stacked Hilbert antenna has 2 parasitic Hilbert curves where one end is directly connected to the original Hilbert conductor and the other end is left as open circuit.
[86]	-	Asymmetrical Octagonal Monopole Antenna	0-3GHz	• The impedance matching of the proposed antenna is improved by shifting the symmetrical conventional antenna into an asymmetrical one. • Size reduction is achieved by cutting the edge of the antenna. • More resonances were obtained by etching the ground plane into ɾ shape.
[88]	-	Patch Antenna Log Periodic Antenna Waveguide Slot Antenna	0-2GHz	• The larger the antenna size, the better the sensitivity of detection. Consequently, the waveguide slot antenna showed the best measured results of the three antenna types used.
[89]	-	Disk-Type Antenna Loop-Type Antenna	0-8GHz	• Loop-type antennas are usually embedded in the insulator when used for detection of PD in GISs. • Disk-type antennas are connected internally, but close to the outer tank wall as shown in Fig.1.10.
[92] [93]	Spacer (Not main but is used)	Disk Couplers	0-6GHz	• Three different types of defects were simulated namely a metal particle attached to the central conductor, a particle attached to the outer conductor, and a particle attached to the insulator. • E-Field intensity was measured internally and externally to understand the EM wave propagation behavior. Propagation was verified to be in the longitudinal direction. • Low frequency components cannot leave the GIS tank making it hard to detect such fields externally.

operation of the GIS [100]. In both steps, the pulse used at the transmitting sensor is chosen such that the transmission coefficient between the transmitting and receiving sensors is very close to the actual signal captured by the receiving sensor due to the PD pulse. Figure 2.12 shows how the CIGRE sensitivity is experimentally set up. In contrast, Figure 2.13 [101] shows a comparison between the captured signals when an actual pulse is used and the captured signal when a transmitting sensor is used. One can see the considerable similarity between the captured signals for both cases. This, indeed, is the main reason for choosing such a technique to model PD signals and avoid dealing with dipoles that do not consider all complexities associated with the actual exact behavior of the PD pulse.

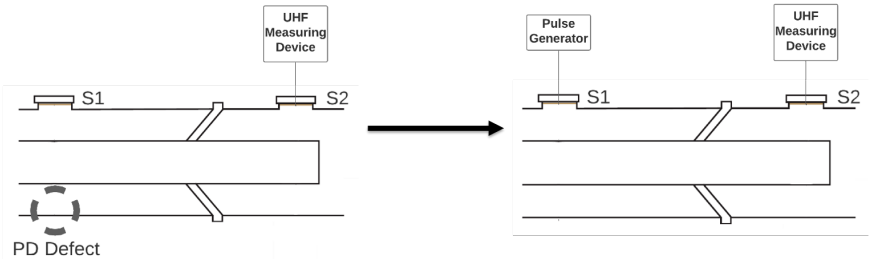

Figure 2.12: CIGRE Sensitivity Verification Recommendations Experimental Setup.

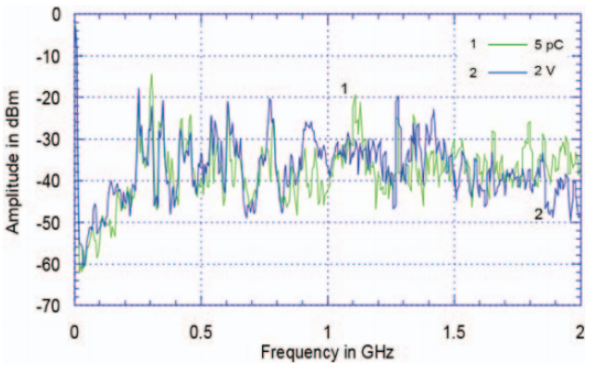

Figure 2.13: Comparison between an actual PD signal and a transmitting signal captured by a receiving sensor "reprinted from [101]".

2.3 Conclusion

Gas-insulated switchgear has become essential in power system utilities due to their higher efficiency, reliability, and smaller size. With the rapid technological growth in power systems, the need for continuously monitoring such devices has become of great importance. UHF method for the diagnostic of GIS has become widely used due to the many benefits, including the high sensitivity and excellent immunity to noise and interferences. Thus, this chapter discusses EM wave behavior due to PD detected by the UHF techniques in GIS devices. The main concluding remarks are:

- There are two types of mechanisms that govern the phenomenon of PD, namely Townsend and Streamer mechanisms. If the void or gap size is small, Townsend mechanism explains the behavior of PD. Nevertheless, if the gap size gets larger, Streamer mechanism explains the space charge and formulation of photons.
- Different types of pulse models can be used to represent PD pulses. Such models include Gaussian pulse, Wanninger pulse, and Double Exponential pulse.
- The Larmor's formula explains the radiation of the electromagnetic waves during the event of PD which is caused by the acceleration and deceleration of charged particles.
- EM radiation due to small voids or gaps can be modeled as an electric dipole.
- The angle between the PD source and coupler used to detect EM waves has a large impact on the intensity of the detected signals.
- L and T structures can cause mode transformation to the signal propagation. Such structures can also cause large attenuation and multiple reflections to EM waves.
- Disconnecting switches can change the environment of the GIS from coaxial waveguide to circular waveguide causing attenuation and reflections to the TEM mode components.
- Changing the inner or outer radii of GIS can cause reflections in the EM waves.

- Spacers do not have a large impact on the attenuation of the EM waves, but they can affect the time of flight of waves.
- Internally connected sensors have better sensitivity than the external sensors since the later receive weaker signals and are more prone to noise.

3. PD SIGNAL PROPAGATION IN GIS: ULTRA-HIGH FREQUENCY DETECTION-BASED MODELING *

A GIS has become an essential part of electrical power substations due to the associated merits of such a capital asset. Although such resilient devices can rarely suffer from failure, PD is responsible for around 85% of their recorded collapses. UHF techniques have been widely used in detecting and localization PD for a long time because of their immunity to noise and high sensitivity. Understanding electromagnetic (EM) wave behavior in GIS systems is significant for improving the utilization of UHF sensors in PD detection and for the optimal allocation of UHF antennas inside GIS systems. Thus, this chapter is devoted to building a detailed 3D FE model based on UHF detection techniques to understand the propagation behavior of EM waves inside GIS. A disk-type UHF sensor is used for acquiring EM waves inside the GIS. The sensitivity of the sensor has been obtained using a gigahertz transverse electromagnetic (GTEM) test cell. The proposed model investigates the impact of multiple disconnecting parts, including L structure, the relative angle between PD source and sensors, and disconnecting switches on the propagation of electromagnetic waves based on step 1 of the CIGRE recommendations. A simple L structured model is initially built to validate the modeled GIS, and a comparative analysis has been conducted between the built model and the experimental and analytical results from the literature.

3.1 Model Overview

An L structured GIS model is built using the Multiphysics platform of COMSOL to study the behavior of EM waves propagating inside the GIS. The inner and outer diameters of the model are 160 mm and 400 mm, respectively. A Gaussian pulse with a peak centered at 1 ns is injected using the transmitting sensor shown in Figure 3.1, whereas the receiving sensors are used to acquire EM waves. Sensors 2 and 3 are also rotated by 90 to study the impact of changing the angle between

*Part of this chapter is reprinted with permission from "PD SignalPropagation in GIS: Ultra-High Frequency Detection-Based Modeling" by A. Darwish, S. S. Refaat, H. Abu-Rub and H. A. Toliyat, 2020. IEEE Sensors Journal, copyright [2021] by IEEE.

PD source and receiving sensors on EM wave propagation. Thus, a total of 5 sensors are placed inside the GIS enclosure. Figure 3.2 shows the 3D schematic of the modeled GIS.

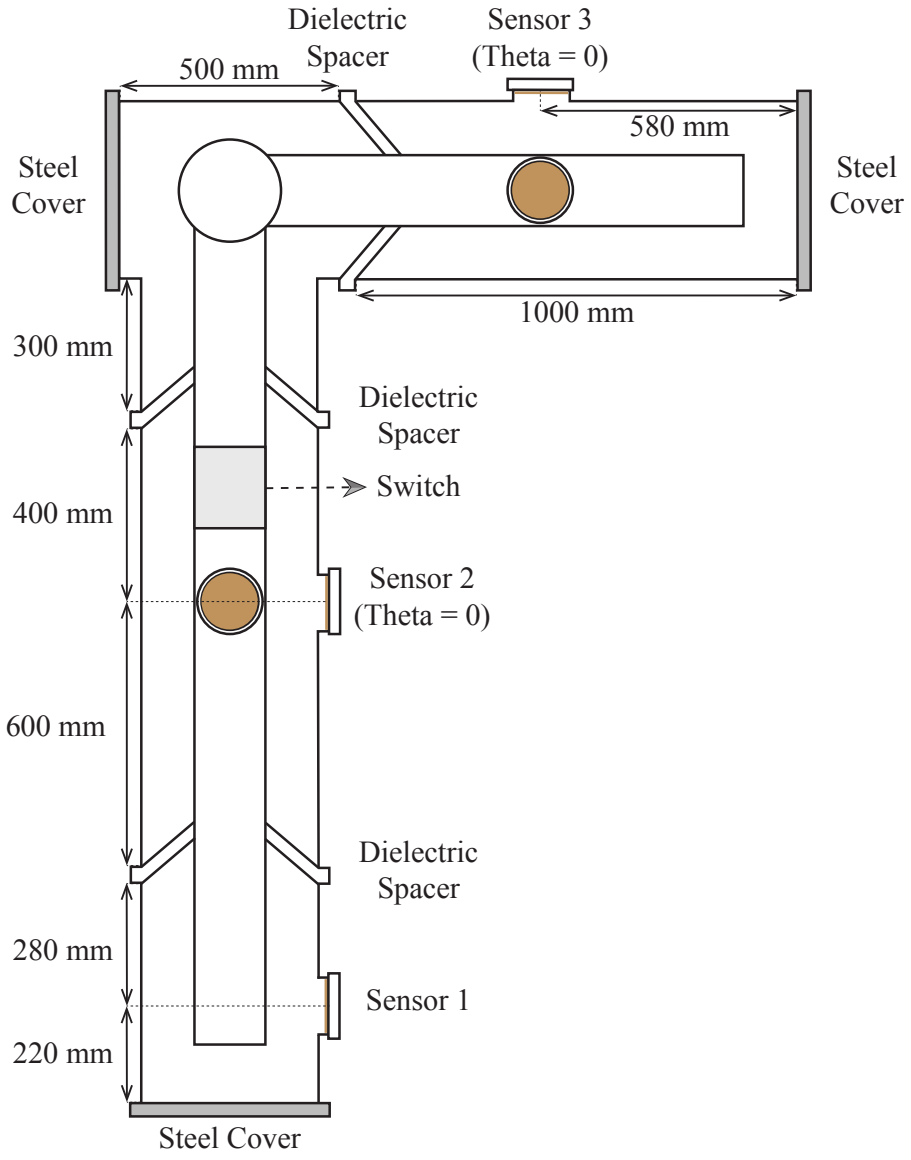

Figure 3.1: 2-Dimensional view of the proposed GIS model. SF_6, Epoxy Resin, and steel covers are modeled to account for transmission and attenuation of EM waves.

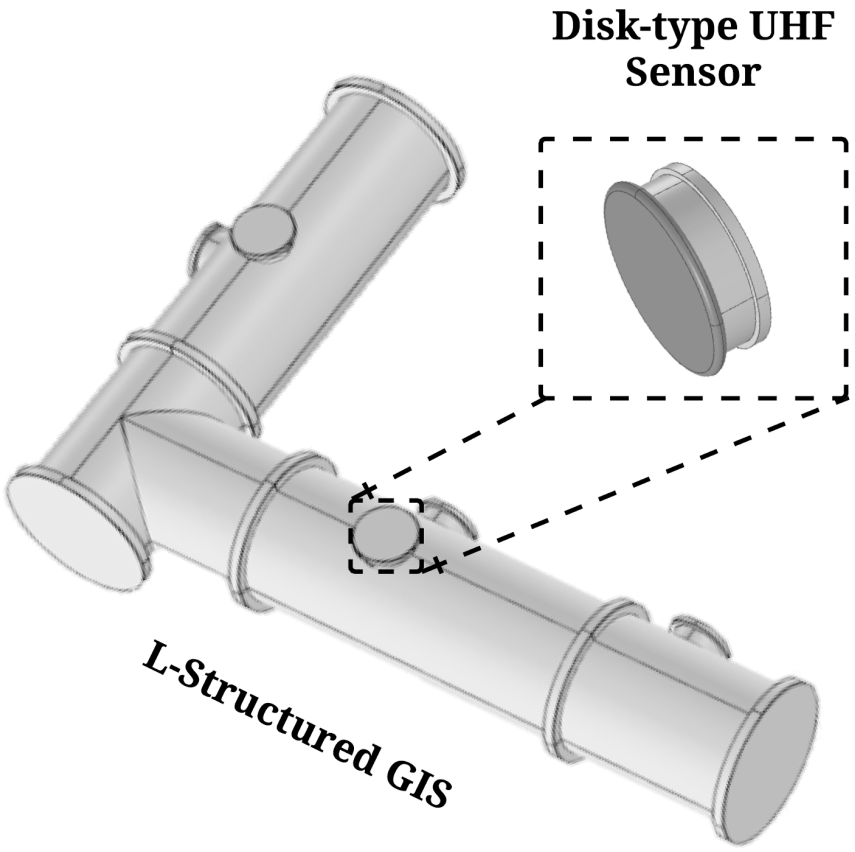

Figure 3.2: 3D schematic of the modeled GIS structure.

The used pulse is represented by the following equation [96]:

$$GP(t) = V_0 \, e^{-\frac{t^2}{2\sigma^2}} \tag{3.1}$$

The Fourier representation of this pulse is given by:

$$GP(\omega) = V_0 \, \sigma \, \sqrt{2\pi} \, e^{-0.5\omega^2\sigma^2}, \tag{3.2}$$

where V_0 is the amplitude of the pulse, and σ determines the pulse width. Figure 3.3 shows the used Gaussian pulse with its frequency representation. The time-shift impact is not shown in the

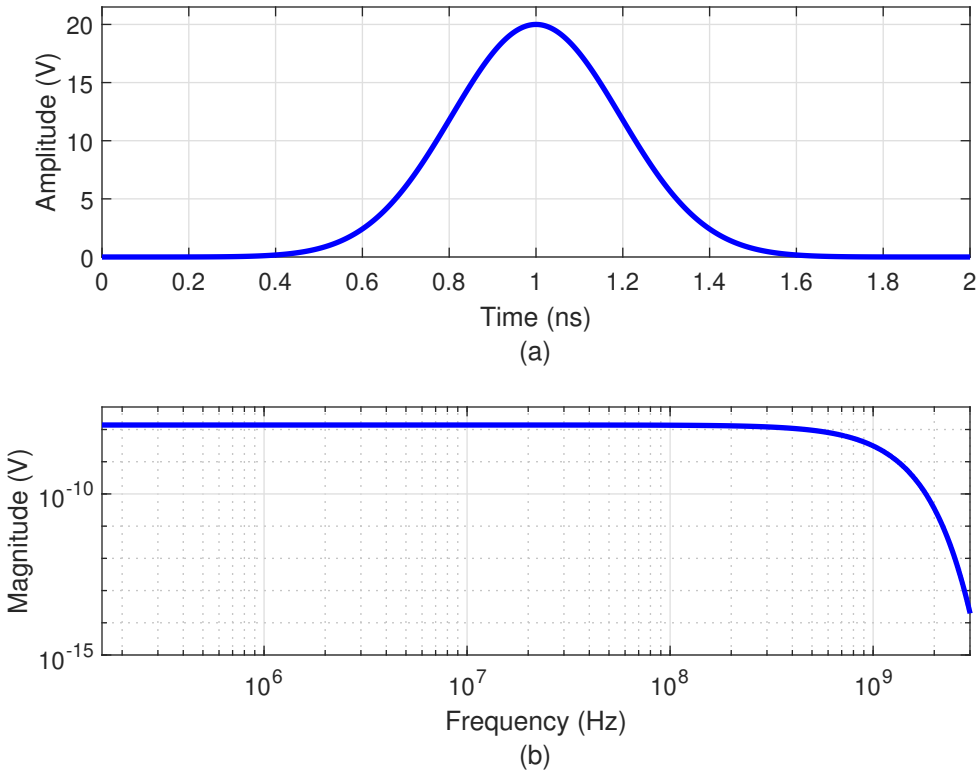

Figure 3.3: a) The used Gaussian pulse at the source (transmitting sensor). b) Frequency representation of the Gaussian pulse. It can be seen that the magnitude of the frequency-domain signal is very low since the total energy of the pulse is low.

frequency-domain representation since the magnitude of the voltage is shown.

The insulating medium, SF_6, is used to fill the space inside the structure, whereas Epoxy Resin ($\epsilon_r = 4.8$) characterizes the dielectric spacers. The inner and outer conductors are modeled as perfect electric conductors (PEC) to reduce the computation time. Electromagnetic waves inside the GIS are obtained by solving the following boundary value problem (BVP) [22, 74]:

$$\nabla \times \left(\frac{1}{\mu_r}\nabla \times \mathbf{A}\right) + \mu_0\sigma\frac{\partial \mathbf{A}}{\partial t} + \mu_0\epsilon_0\left(\epsilon_r\frac{\partial^2 \mathbf{A}}{\partial t^2}\right) = 0, \text{ in } \Omega \subseteq R^3 \tag{3.3}$$

$$\nabla \times \left(\frac{1}{\mu_r}\nabla \times \mathbf{A}\right) + j\omega\mu_0\sigma\mathbf{A} - \omega^2\mu_0\epsilon_0\epsilon_r\mathbf{A} = 0, \text{ in } \Omega \subseteq R^3 \tag{3.4}$$

$$\mathbf{n} \times \mathbf{A} = 0 \text{ over } \partial_{\text{PEC}},\ \Omega \subseteq R^3 \tag{3.5}$$

$$\begin{gathered} -\mathbf{n} \times (\frac{1}{\mu_r} \nabla \times \mathbf{A}) - \frac{\mu_0}{\mathbf{Z}_{port}} \frac{\partial}{\partial t} \mathbf{n} \times (\mathbf{n} \times \mathbf{A}) = \\ \frac{2\mu_0}{\mathbf{Z}_{port}} \mathbf{n} \times (\mathbf{n} \times \mathbf{E}_0),\ \text{over } \partial_{\text{port}}\ \Omega \subseteq R^3 \end{gathered} \tag{3.6}$$

$$\mathbf{A} = 0\ for\ \mathbf{t} \leq\ 0,\ \text{in } \Omega \subseteq R^3 \tag{3.7}$$

Equations (3.3) and (3.4) are used to solve EM wave propagation in the volume (R^3) of the GIS model. Equation (3.5) shows that no EM waves are propagating after the PEC boundaries (R^3), but rather, they get reflected. Equation (3.6) is used to calculate the intensity of EM waves received by each port along the boundary (R^2). In the above BVP, **A** represents the magnetic vector potential, **n** is a unit vector normal to the surface, $\mathbf{Z}_{\text{port}}$ represents the impedance seen at each port, $\mathbf{E}_0$ is the source electric field (for the sensor used to inject the pulse, or transmitting sensor), and $\mu, \epsilon,$ and σ represent the electric permeability, permittivity, and conductivity of the different materials, respectively. Equation (3.3) is used to obtain the time-domain results, whereas (3.4) gives the frequency-domain results. Equation (3.6) is used to obtain time-domain results. A similar equation is also used to obtain the frequency-domain results at the port.

3.2 UHF Sensor Modeling

The following section presents the modeling approach of the used disk-type UHF sensor inside the GIS [102]. The diameter of the UHF sensor is 150mm, and its height is 50mm. Tufnol $(\epsilon_r = 3.4)$ characterizes the sensor's dielectric material. PEC is used to model all metallic components of the sensor. A simplified GTEM cell model has been built to reduce the complexity and computational time of the FE solver. The simplifications made are [91]:

- Half of the GTEM has been modeled due to the symmetry of the cell.

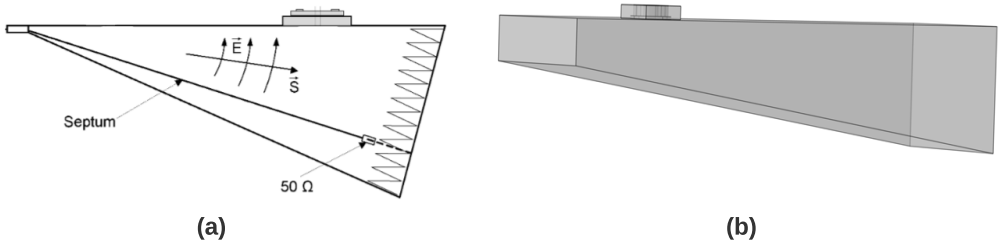

Figure 3.4: The modeled GTEM test cell. a) side-view "adapted from [103]", b) 3D modeled structure.

- Side walls of the GTEM test cell are represented by “Scattering Boundary Conditions” to absorb any incident signals and obtain a vertically polarized electric field.
- The cell length has been reduced to 2 m instead of using the full 3 m length. This assumption is made to avoid having very fine mesh size at the input of the test cell. Figure 3.4 shows the modeled GTEM [103].

A Gaussian pulse with a rise-time of 300ps is used at the input. Then, the sensitivity of the UHF sensor was obtained by calculating the antenna factor (AF) using [103]:

$$\text{AF}(f) = \frac{E(f)}{U(f)}, \tag{3.8}$$

$$\text{Sensitivity}(f) = \frac{1}{\text{AF}(f)}, \tag{3.9}$$

where $E(f)$ is the input electric field strength, and $U(f)$ is the detected voltage at the antenna terminal. Initially, time-domain signals were obtained, and FFT was then used.

Figure 3.5 shows the received voltage and sensitivity of the UHF sensor. It can be seen that the sensitivity is higher than 6mV/Vm^{-1} over 500MHz to 1500MHz, the minimum sensitivity placed by a UK technical guidance note [91]. The average sensitivity in Figure 3.5(b) is obtained over the frequency range set by the UK technical guide. By comparing the obtained frequency

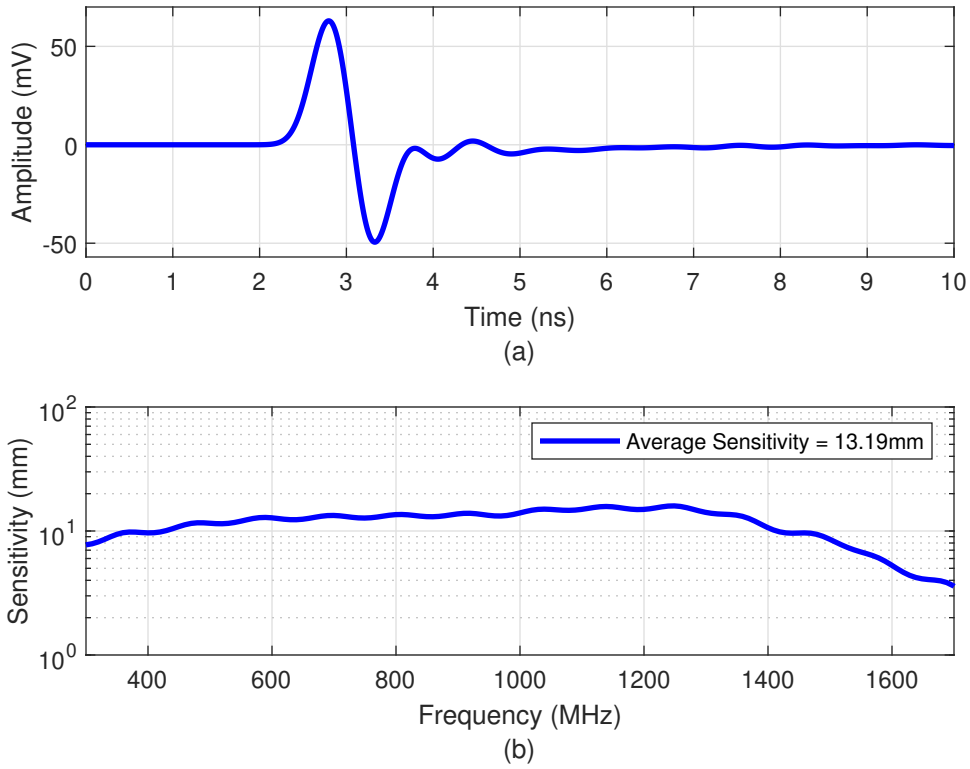

Figure 3.5: a) Voltage waveform obtained by the UHF sensor due to a Gaussian pulse input signal. The input has a rise-time of 300ps and an amplitude of 31V/m. b) The frequency response of the UHF sensor.

response with that in [102], the overall behavior is similar, with slight differences attributed to the differences in the sensor's implementation details.

3.3 Simulation Results

In this section, four different cases are modeled and discussed. The first model represents a simple L structure GIS without any disconnecting parts. The model compares the obtained results with analytical and experimental data from the literature to validate the obtained results. The second and third models are used to investigate the impact of disconnecting switch lengths and the L structure on the EM wave propagation. Finally, the fourth model is used to investigate the attenuation of EM waves as a function of distance.

3.3.1 Case I: Closed Switch

Normalized electric field distribution at three different frequencies, namely 10MHz, 400-MHz, and 1400MHz, is simulated and shown in Figure 3.6. Since the input time-domain signal is a Gaussian pulse with a very high rise-time, the frequency-domain representation of such a signal has a very low magnitude since it covers a wide frequency range (refer to Figure 3.3). The input voltage magnitude is 1.38e-8V at 10MHz, 1.085e-8V at 400MHz, and 7.4e-10V at 1400MHz. Thus, the electric field distribution is normalized with respect to 1.25e-9Vm^{-1} at 10MHz, 9.8e-10 Vm^{-1} at 400MHz, and 6.7e-11 Vm^{-1} at 1400MHz to maintain a constant multiple of magnitude for all cases. Coaxial waveguide structures support TEM mode, which is independent of frequency. Nonetheless, for TE and TM modes to propagate, the frequency of operation should exceed the associated cut-off frequencies given by the following equations [64, 96]:

$$f_c^{\mathrm{TE}m1} = \frac{v\ m}{\pi(a+b)} \tag{3.10}$$

$$f_c^{\mathrm{TM}1n} = \frac{v\ n}{2(b-a)} \tag{3.11}$$

where a and b are the inner and outer radii of the coaxial waveguide, v represents EM waves velocity, and m and n are integers that determine the mode of operation of the TE and TM modes, respectively. Based on (4.7) and (3.11), the cutoff frequencies are around 340MHz and 1235MHz for TE_{11} and TM_{11} modes, respectively. The subscripts associated with the TE and TM modes indicate the number of full-wave patterns along the circumference and the diameter of the GIS model. Moreover, Figure 3.6(a) shows that TEM mode components appear before and after the L structure and are uniformly distributed along with the GIS. This agrees with the results obtained in [22, 47, 53]. When the frequency is increased to 400MHz, some resonances are created, as shown in Figure 3.6(b). For EM waves, GIS devices act as cavity resonators due to the existence of dielectric spacers and metallic covers [22]. On the other hand, the electric field experienced large attenuation due to the L structure, which agrees with the experimental data obtained in [47] since

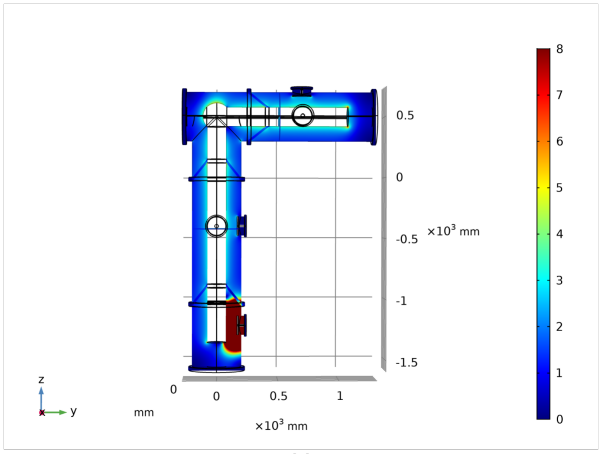

(a)

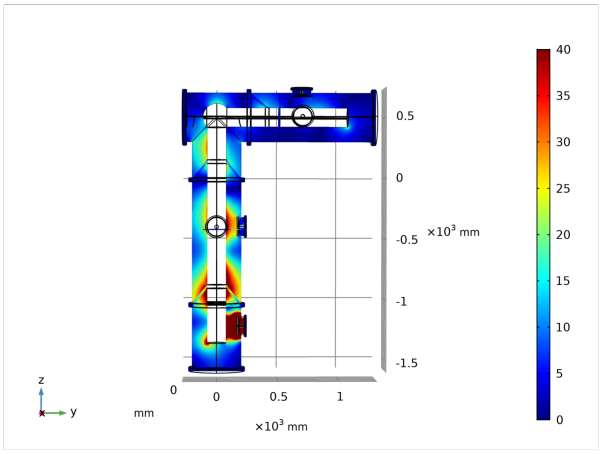

(b)

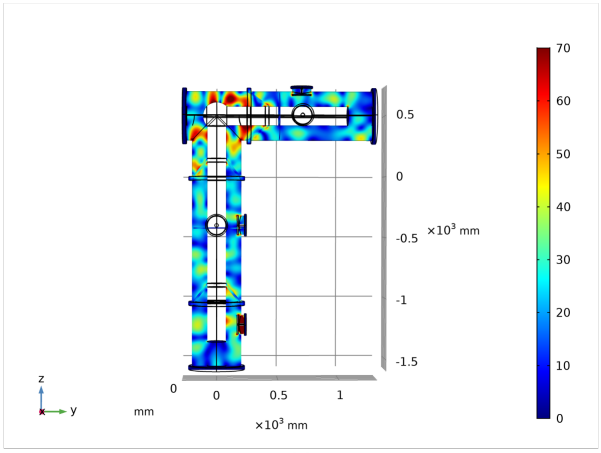

(c)

Figure 3.6: Electric field distribution inside the GIS enclosure at a) 10 MHz, b) 400 MHz, and c) 1400 MHz.

most of TE_{11} mode of propagation gets reflected due to L structures. Finally, Figure 3.6(c) shows the electric field distribution at 1400MHz where TM mode can propagate. Many resonances are created inside the GIS cavity. This behavior is attributed to the fact that the TM mode of propagation requires higher frequencies to propagate inside a coaxial waveguide. On the contrary, the electric field intensity after the L structure remained strong as TM mode has longitudinal electric field components. These components act as sources for EM waves to propagate after the L structure [22, 48].

Figure 3.7 shows the transmission coefficient, or S-parameters, between sensors 1 and 2. The figure illustrates multiple dips and peaks created as a function of frequency verified by the experimental work in [22]. Such behavior is attributed to the creation of cavity resonators, as stated earlier. The power received by sensor 2 when $\theta = 0$ and $\theta = 90$ are identical at low-frequency. TEM mode of propagation is independent of the angular position, which justifies such results. On the other hand, as the frequency approaches 340MHz, the received power by sensor 2 $(\theta = 0)$ becomes higher than that when $(\theta = 90)$. At such frequencies, TE_{11} mode can propagate inside the switchgear. TE_{11} mode is highly dependent on the angular position causing the observed behavior in the S-parameters. Nonetheless, this behavior is not observed over the whole frequency range where TE_{11} mode is dominant. Moreover, when the frequency approaches 700MHz, it becomes difficult to differentiate which sensor receives more power due to the large number of resonances created in the GIS. Such results are analytically verified in [41] using the following:

$$E_r^{\text{TEM}} = \frac{Z_0}{4\pi b \ln\left(\frac{b}{a}\right)} \ln\left(\frac{r_2}{r_1}\right) I(\omega)\, e^{-\frac{j\omega z}{v}}, \tag{3.12}$$

$$E_r^{\text{TE}_{mn}} = A_{mn} \int_{r_1}^{r_2} \frac{Z_m(u_{mn} r')}{r'} dr' \cos(m\phi) I(\omega) F_{\text{TE}}^{mn}(\omega), \tag{3.13}$$

$$E_r^{\text{TM}_{mn}} = B_{mn} \int_{r_1}^{r_2} X'_m(v_{mn} r') dr' \cos(m\phi) I(\omega) F_{\text{TM}}^{mn}(\omega), \tag{3.14}$$

where Z_0 is the characteristic impedance of the coaxial waveguide, r_1 and r_2 are variables to

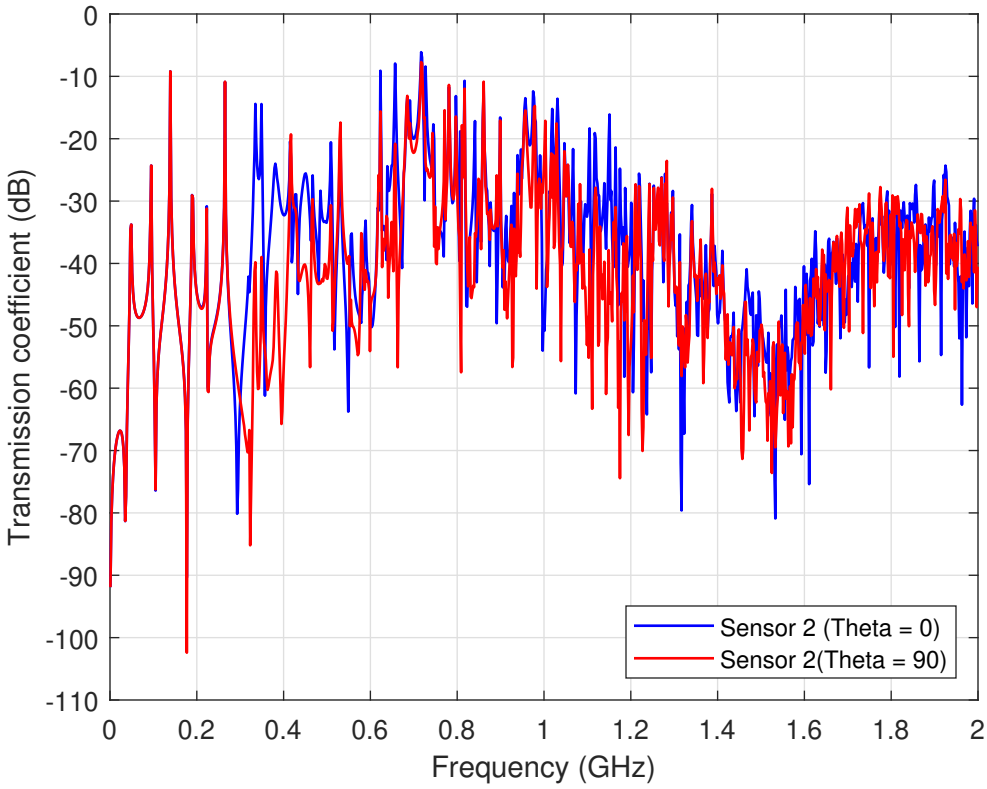

Figure 3.7: Transmission coefficient between sensor 1 to sensor 2 (S21) (Case I).

determine the radial path of PD current, $I(\omega)$ is the frequency representation of the current pulse, A_{mn} and B_{mn} are constants calculated as in [41], F_{TE} and F_{TM} are complex exponential functions of ω, u_{mn} and v_{mn} are the mode eigenvalues of TE and TM modes, respectively, and Z_n and X'_n involve some combinations of Bessel functions. The equations mentioned above verify that the higher-order modes are dependent on the angular position between PD source and receiving sensors, whereas TEM mode is not. Equation (3.13) explains the reduction on the received EM waves by sensor 2 $(\theta = 90)$ as compared with $(\theta = 0)$ for TE_{11} mode frequencies. However, when the frequency gets higher, new modes are created, and the total received power is the superposition of these modes.

Figure 3.8, on the other hand, shows the transmission coefficient between sensors 1 and 3. A large similarity between the received power by sensor 3 when $\theta = 0$ and $\theta = 90$ can be observed.

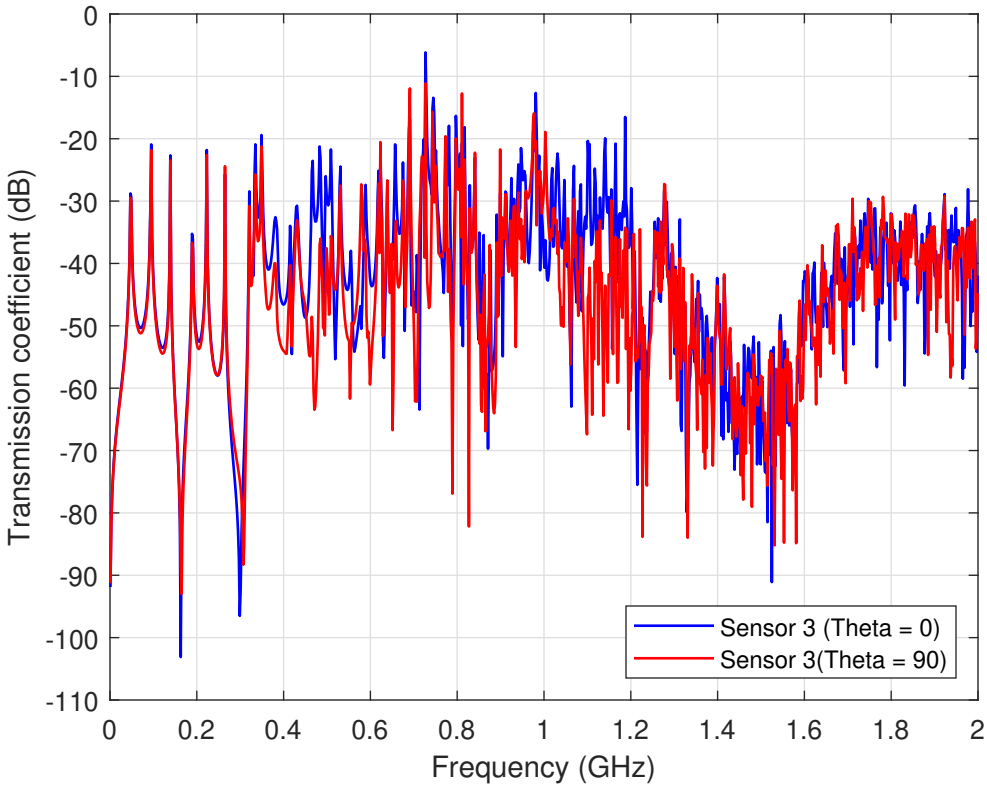

Figure 3.8: Transmission coefficient between sensor 1 to sensor 3 (S31) (Case I).

There is a smaller difference in the received power at TE_{11} frequencies as compared with Figure 3.7. This is attributed to the high reflections of TE_{11} weakening the signal after the L structure. At frequencies above 1300MHz, S31 behavior becomes very similar to S21 since TM mode is propagating.

Figure 3.9 and Figure 3.10 show that the arrival time of EM waves from sensor 1 is around 3.1ns and 8ns to sensor 2 and sensor 3, respectively. EM waves propagate at velocity of 2.964e8m/s in SF_6 and 1.369e8m/s inside dielectric spacers. Based on time calculations, EM waves arrive at sensors 2 and 3 at 3.18ns and 8.08ns, considering that waves follow the shortest path between PD source and sensors. Such results verify that waves travel in all directions away from the source. This can also be observed from Figure 3.11, showing EM waves propagation in the GIS as a function of time. When EM waves reach the L structure, they start propagating in all directions

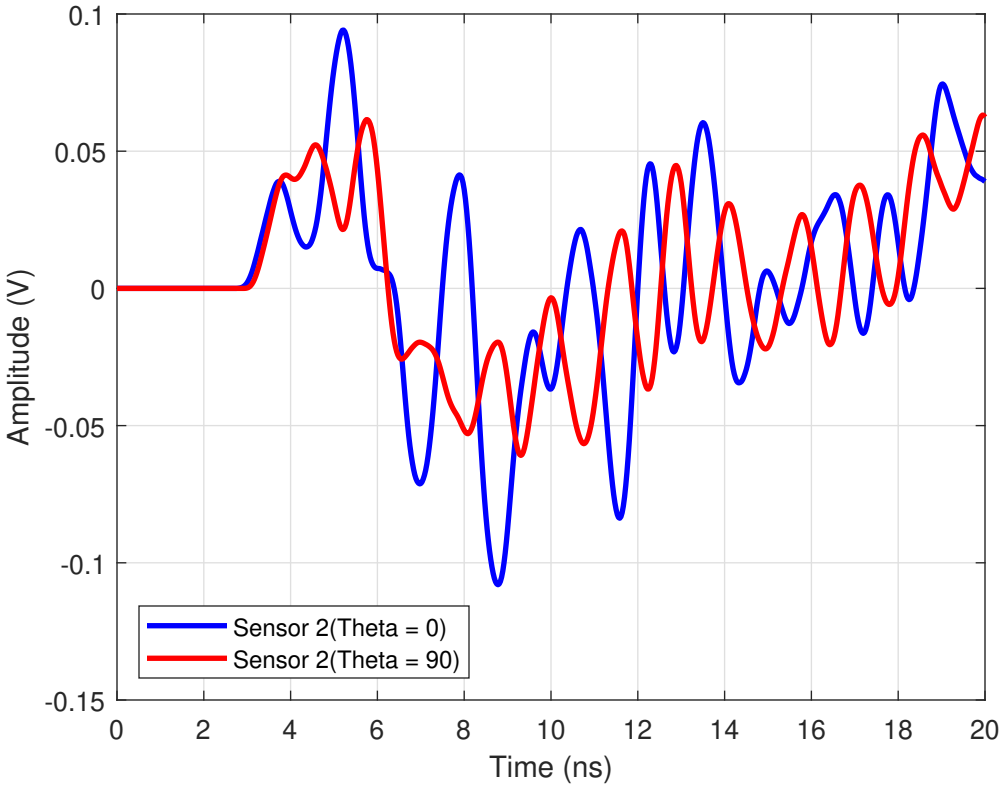

Figure 3.9: Voltage received by sensor 2 (Case I).

towards the second section of the GIS. In order to accurately calculate the arrival time of waves at sensor 3, the shortest distance is to be considered. Albeit the inner conductor has an impact on the arrival time of EM waves at sensor 3, $\theta = 0$ for this simulation case, such impact is minimal and can be ignored [4].

Although the overall behavior between the obtained results and the experimental and analytical results is similar, the obtained results' magnitudes can be different. There is no clear relation between PD magnitude, and the received RF signal intensity via UHF sensors [95]. This justifies the differences in the intensity of EM waves between the proposed model herein and the experimental data.

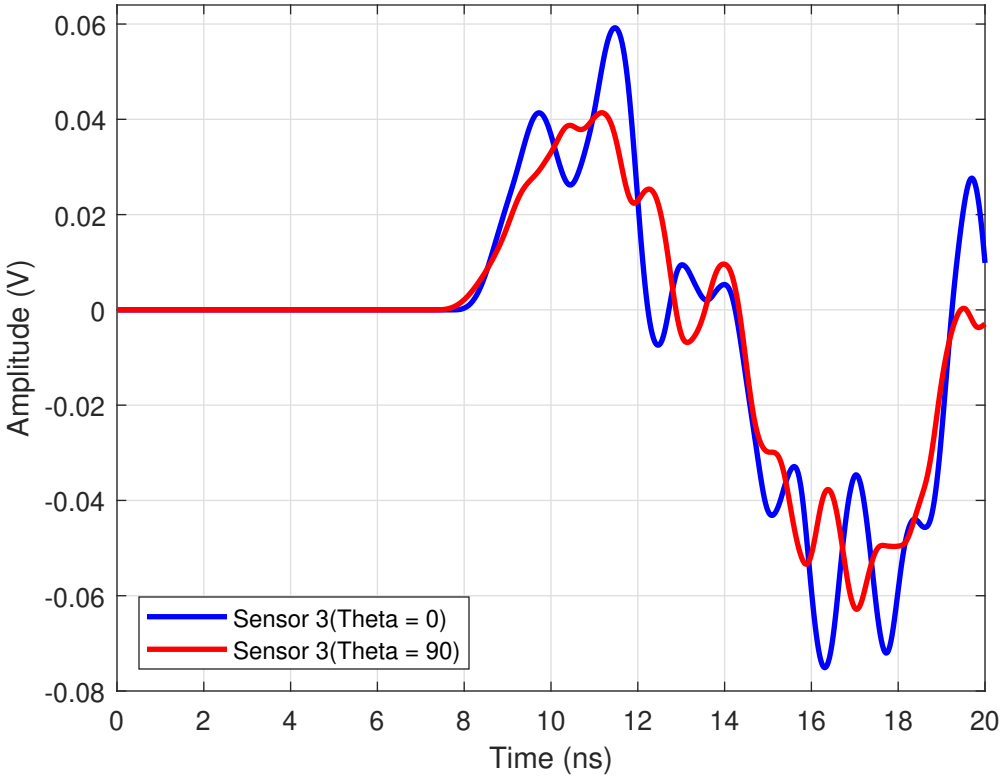

Figure 3.10: Voltage received by sensor 3 (Case I).

3.3.2 Case II: Open Switch ($Length$ =150mm)

The electric field distribution, at 10MHz and 1400MHz with a 150mm long disconnecting switch, is shown in Figure 3.12. Based on Figure 3.12(a), TEM mode is mostly attenuated because of the switch. When a disconnecting switch is open, GIS is no longer regarded by EM waves as a coaxial waveguide, but rather, it is seen as a circular waveguide that does not support low-frequency (TEM) modes. This causes a rapid attenuation to TEM waves inside the GIS after the switch. Figure 3.12(b) shows that higher-order modes can still propagate after the switch since circular waveguides support the propagation of TE and TM modes.

Figure 3.13 presents the transmission coefficient between sensor 1 and sensor 3 when the disconnecting switch is open. S21 is not shown since it is similar to that of case I (Figure 3.7). When the disconnecting switch is open, a rapid attenuation to TEM mode signals inside the GIS after

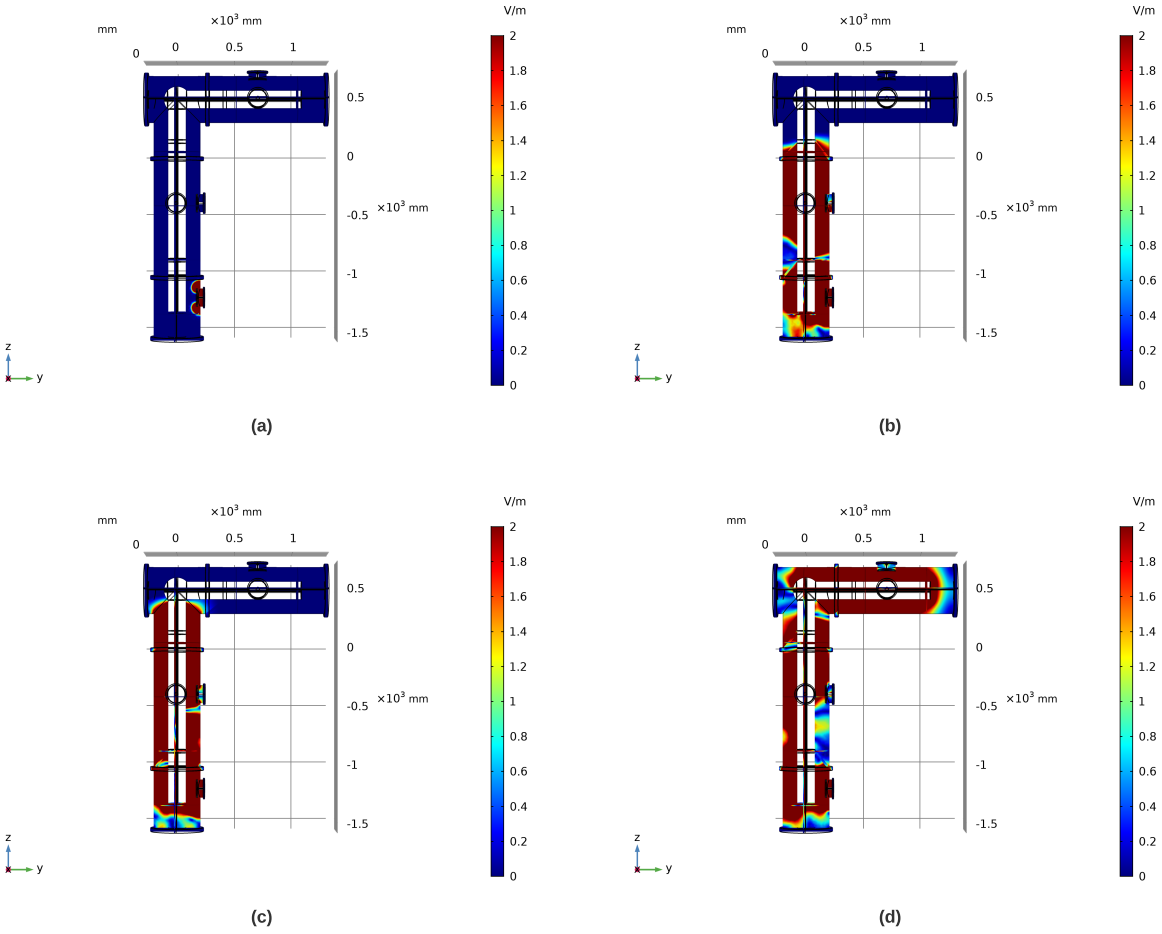

Figure 3.11: Electric field distribution inside the GIS enclosure at a) 0.5ns, b) 5ns, c) 6ns, and d) 10ns. It is clear based on the obtained results at t = 6ns that EM waves propagate in all directions once the L-structure is reached.

the open switch is observed. The main reason for that is, as explained earlier, the sudden change of the waveguide structure from coaxial to circular waveguide. This explains the attenuation of TEM waves in Figure 3.13 as compared with Figure 3.8. Higher-order frequency modes are not primarily affected since they can propagate in circular waveguides.

Figure 3.14 shows the arrival time of EM signals received by sensor 3 when the switch is open. Voltage received by sensor 3 is initially lower than the first case, whereas the arrival time of signals is identical. This shows that open disconnecting switches do not cause a complete attenuation of the TEM mode of propagation. If TEM mode is completely attenuated, the arrival time would be

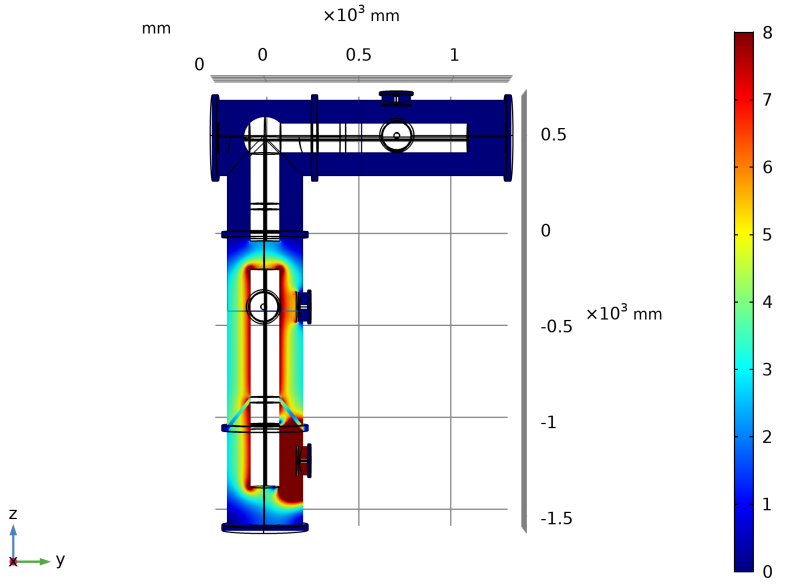

(a)

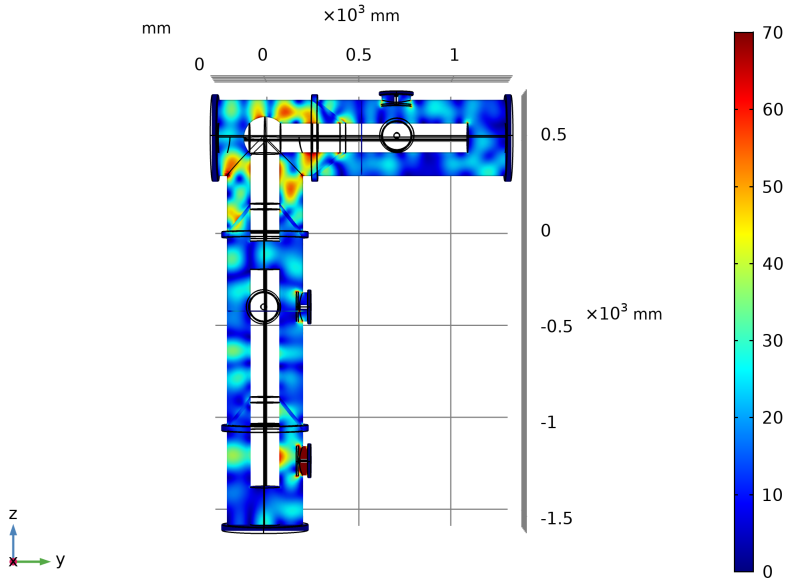

(b)

Figure 3.12: Electric field distribution inside the GIS enclosure at a) 10 MHz, b) 1400 MHz.

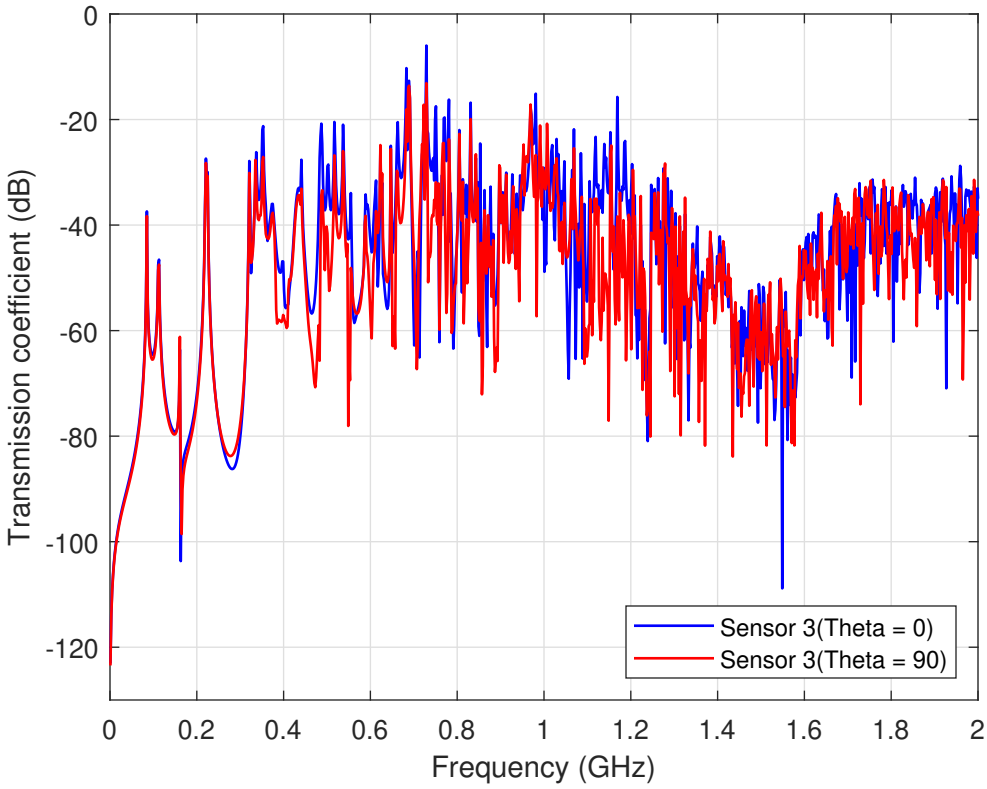

Figure 3.13: Transmission coefficient between sensor 1 and sensor 3 (S31) (Case II).

different since higher-order modes are slower than TEM. Equation (3.15) shows the propagation velocity of TE modes [96]:

$$v_{\text{TE}} = v \cdot \sqrt{1 - \left(\frac{f_c}{f}\right)^2} \tag{3.15}$$

where v is TEM wave propagation velocity, f_c is the cutoff frequency of the different modes, and f represents the frequency of operation. Based on (3.15), the higher the TE order mode, the slower the propagation velocity becomes.

3.3.3 Case III: Open Switch ($Length$ =300mm)

The voltage received by sensor 3 is shown in Figure 3.15 when the length of the switch is increased to 300mm. The received voltage amplitude is initially slightly reduced compared with

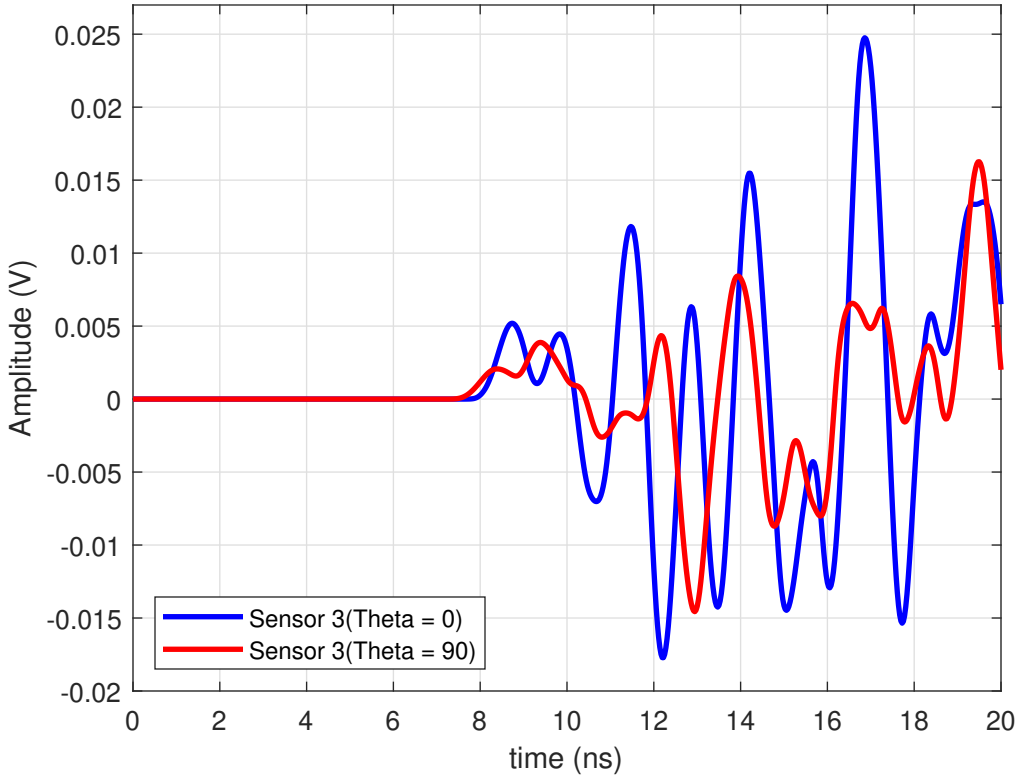

Figure 3.14: Voltage received by sensor 3 (Case II).

Figure 3.10 and Figure 3.14. TEM mode of propagation has undergone more attenuation compared to Case II. An open switch does not necessarily cause a complete attenuation to the TEM mode of propagation. Low-frequency waves would experience rapid attenuation due to open switches; however, if the length of such switches is not sufficiently large, part of TEM frequencies would be able to reach the coaxial structure and continue propagation.

3.3.4 Case IV: Sensor 3 as a Transmitting Source

In this section, the disconnecting switch is closed, whereas sensor 3 $(\theta = 90)$ is used as the input to inject the pulse. This section is used to investigate the impact of distance between PD source and sensors on the propagation of EM wave behavior. Figure 3.16 shows the transmission coefficient from sensor 3 to 1 (S13) and sensor 3 to 2 (S23). The figure illustrates that S23 is slightly higher than S13 over most of the high-frequency range. However, TEM mode shows that

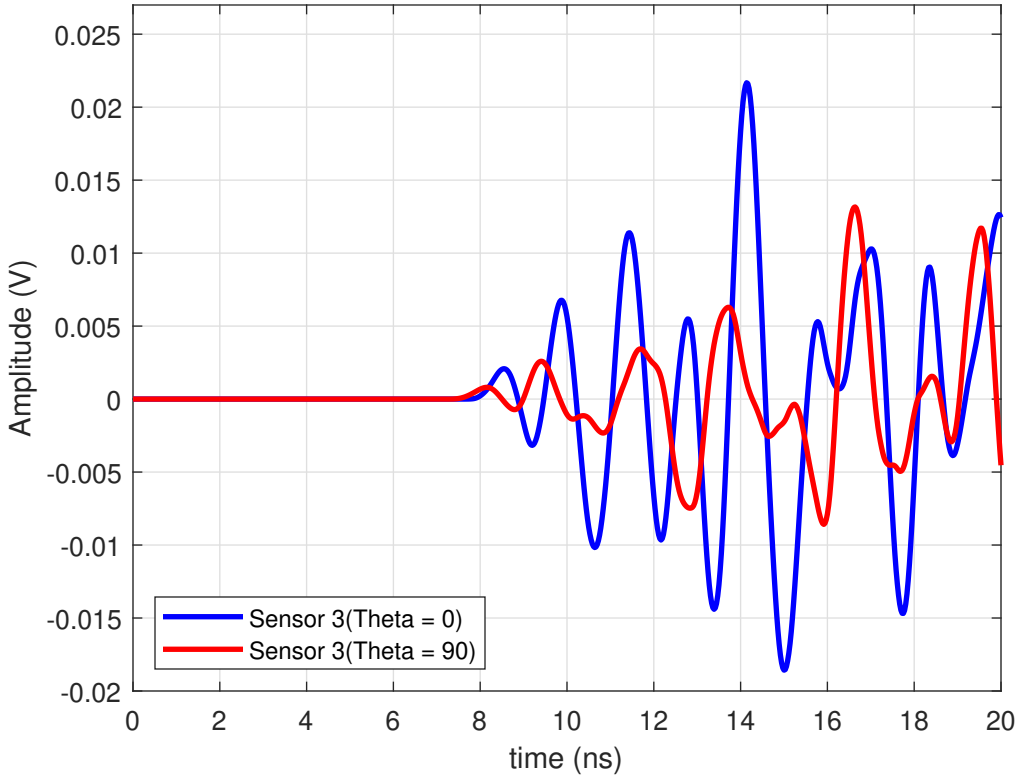

Figure 3.15: Voltage received by sensor 3 (Case III).

S13 is either identical to or higher than S23. The reason is that low-frequency components experience less attenuation as compared with high-frequency. On the other hand, the sudden reduction in S23 at around 70MHz and 210MHz is attributed to the created resonances since GIS devices comprise a complex structure for EM waves. Thus, fully understanding the exact behavior of such propagating waves is complicated. High-frequency components experience higher attenuation, causing a reduction in S13 compared with S23. This can be observed over frequencies ranging from 500MHz to 630MHz. Finally, when the frequency is above 630MHz, the large number of created resonances makes it challenging to distinguish which sensor receives higher energy.

3.4 Conclusion

Time-domain and frequency-domain results of the propagating EM waves inside a GIS were obtained using a Maxwell finite element solver. The results were compared with experimental data

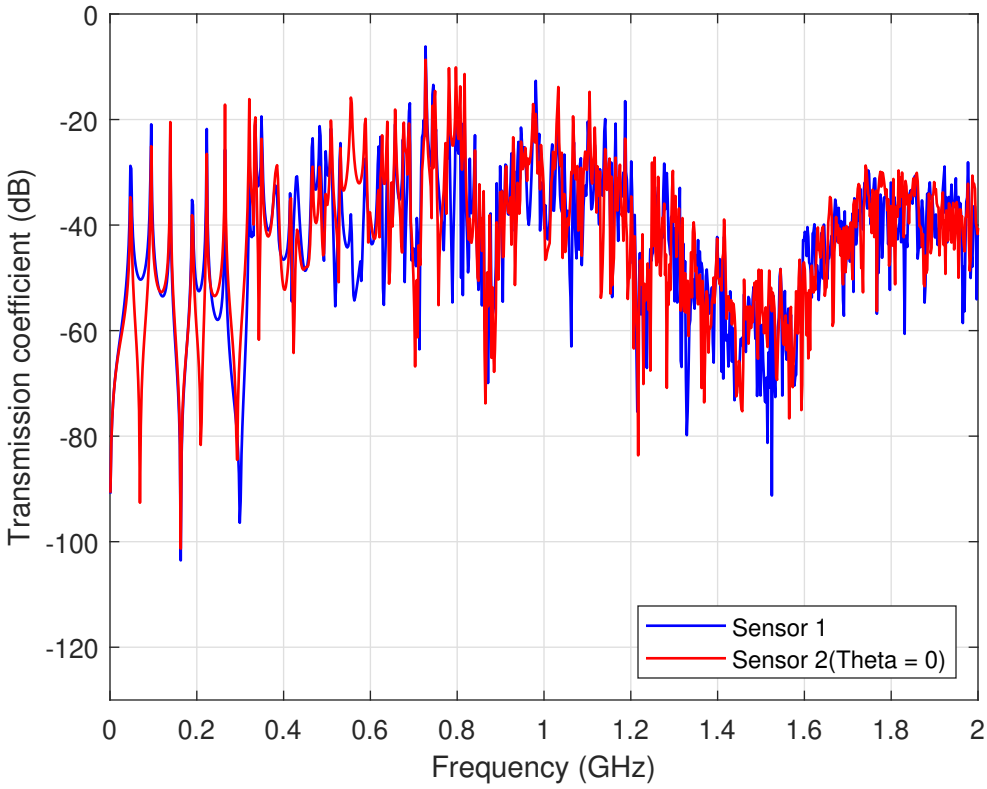

Figure 3.16: Transmission coefficients S13 and S23 (Case IV).

from the literature. Step 1 of the CIGRE recommendations were used to analyze EM waves inside GIS systems due to multiple disconnecting parts. The radiated EM waves were then collected using the rest of the UHF sensors, and results were used to analyze the propagating EM waves. The proposed model can be used to understand and analyze EM waves due to PD to better utilize UHF sensors inside GIS systems. The following concluding remarks are drawn:

- Finite element analysis can accurately model EM wave behavior inside complex structures like GIS systems.
- CIGRE recommendations are convenient for analyzing EM wave behavior in GIS, even if multiple disconnecting parts exist. Although step 1 of the CIGRE recommendations has been utilized for analyzing EM waves, step 2 can also be used similarly since the UHF detection ranges from 300MHz to 3GHz. In this frequency range, the interference with the

different components of the GIS is minimal. Nonetheless, if the low-frequency components are of interest, step 1 of the CIGRE recommendations is recommended to avoid the possible interferences that might take place inside GIS enclosures.

- PD-based UHF sensors can be modeled and calibrated using FE solvers. The calibration of sensors involves using a GTEM test cell to obtain the sensitivity of the UHF sensor.

- TEM mode propagates even in L structures, but opening a disconnecting switch can cause significant attenuation to such mode of propagation. However, disconnecting switches do not necessarily cause a complete attenuation to low-frequency EM waves unless the switches are sufficiently large.

- Opening a disconnecting switch does not have an enormous impact on the propagation of higher-order modes. This is attributed to the fact that higher-order modes can still be propagating in circular waveguides.

- Although TEM mode is independent of the angular position, higher-order modes can be largely affected. Simply put, the angular position of sensors concerning the source significantly impacts the detected waves.

- The arrival time of signals can be easily calculated for straight GIS devices. If L structures exist, direct calculations cannot give accurate results for the arrival time. In this case, the shortest path between the PD source and the sensor should be considered.

- Unlike high-frequency components, low-frequency modes experience low attenuation with distance.

- The higher the frequency of operation, the more the created resonances inside GIS enclosures, the higher the complexity of understanding EM wave behavior.

4. PD SIGNAL ATTENUATION IN 550 KV GIS: IMPACT OF DIFFERENT BARRIERS ON THE PROPAGATING ELECTROMAGNETIC WAVES

Accurate modeling of partial discharge within gas-insulated switchgear has become of paramount significance to improve the utilization of ultra-high frequency sensors within such capital assets. Providing better insight on how electromagnetic waves propagate within gas-insulated switchgear (GIS) systems provides valuable information that can be used to determine the optimal allocation of ultra-high frequency (UHF) sensors. Thus far, most existing models are not considering the full complexity of the GIS systems due to the many associated challenges and the high computational demand of such system modeling. In this work, a GIS system is modeled using the Maxwell solver of COMSOL multi-physics. CIGRE sensitivity verification recommendations are used to inject UHF signals using an internal sensor. Then, two external sensors, placed on the outer belt of dielectric spacers, are used to capture the radiated electromagnetic (EM) waves. The electric field distribution at selected frequencies is presented and discussed under two operating conditions for disconnecting switches. The modeled GIS contains many barriers, including two bends, multiple sudden changes in the outer to inner diameters ratios, six dielectric spacers, and two disconnecting switches. Time-domain simulation results are also presented to provide an insight into the attenuation properties of EM waves due to the different barriers. Finally, a comparison between simulated and measured results has been carried out to verify the modeling accuracy. The results show that GIS systems form complex structures for the electromagnetic waves, and fully understanding the propagating wave behavior can be tedious.

4.1 CIGRE Sensitivity Verification Recommendations

To bypass the limited information about the correlation between the magnitude of PD discharge and the intensity of EM waves using UHF detection techniques, CSVR have been adopted since 1999 [101]. CSVR is a two-step procedure: laboratory test (step 1) and on-site test (step 2). In step 1, a receiving sensor is initially used to capture the power associated with the EM waves due

to a PD defect placed close to a transmitting sensor while the GIS is off (Step 1 is carried out in this work) as shown in Figure 2.12. It should be noted that the captured power is frequency-dependent. Hence, multiple peaks and dips would be seen when such power is received over a particular frequency sweep.

After obtaining the received power due to the actual PD pulse, the transmitting sensor is used to inject different artificial pulses. The receiving sensor will be capturing the EM wave intensity as a function of frequency. Then, the captured power due to each artificial pulse will be compared with the actual PD pulse response. The chosen artificial pulse would give close magnitude to the actual PD pulse with a tolerance of 20% [101]. Figure 2.12 summarizes the experimental setup of step 1 of CSVR. If readers are interested in additional details about the two steps of CSVR, they are strongly encouraged to refer to [13] since a detailed experimental setup is provided.

CSVR mainly relies on the existence of internally connected sensors/antennas within the GIS. Nonetheless, this limits the usage of such sensitivity analysis to the relatively new GIS systems since old devices do not contain internally connected sensors. Thus far, most existing FE-based GIS models which utilize CSVR to study EM wave behavior within the GIS enclosures rely on internally connected UHF sensors, or ideal ports of excitation [10]. Integrating internally connected sensors to old GIS systems is not a feasible solution due to the high complications associated with opening such metallic encapsulated structures, given that a high pressurized gas (SF6) is contained within such capital assets. Moreover, GIS devices are extremely robust devices with a lifespan extending to few decades. Old GIS systems require more monitoring as compared with newly built systems. Hence, this work proposes applying CSVR using externally connected sensors as receiving sensors due to a wideband signal. Such analysis can help determine the required distance between the externally connected sensors to detect and localize PD activities within GIS devices. This can help optimize the number and location of UHF sensors within old GIS systems. In other words, applying such sensitivity analysis using externally connected sensors can improve UHF detection techniques in GIS systems.

4.2 FE Model Overview

A 550kV GIS model is used in this work to study the EM wave propagation within its enclosure. Figure 4.1 shows the π structure GIS system. Two external sensors are connected at an aperture made on the metallic belt covering the dielectric spacers, as shown in Figure 4.2. The two sensors are used to acquire the resultant EM waves due to the injected signal at the transmitting sensor. Only one external sensor has been used to acquire the propagating EM waves at the two specified locations at a time. Two disconnecting switches, located between UHF sensor A and UHF sensor B, are turned ON and OFF, and the results under the different disconnecting switches states are recorded. This has been conducted to understand the impact of opening and closing disconnecting switches on the propagating waves within the GIS enclosure.

The two external UHF sensors (UHF A and UHF B) are identical and have similar sensitivity. The layout and details of the external sensors are given in Figure 4.3. On the other hand, the dielectric material properties used in the modeling are given in Table 4.1. It should be noted that all external metallic parts of the UHF sensors (Feed point metallic body and the two external metallic extensions) were not considered in the model, as depicted from Figure 4.3(a). The coaxial lumped port used to model the feed point on the model represents the BNC connector that has been used to capture the EM signal power in the actual experiment.

External UHF sensors in GIS are usually connected over the dielectric spacers connecting the different GIS tubes. GIS structures are metallic encapsulated structures that do not allow EM waves to escape the GIS enclosure. Nonetheless, part of the propagating EM waves injected inside the GIS can escape through the dielectric spacers. Hence, external UHF sensors are usually placed on top of the dielectric spacers, as shown in Figure 4.2. In this case, the external sensors can detect part of the EM waves escaping the GIS enclosure. The main reason for placing the external UHF sensors, as shown in Figure 4.1, is to study the attenuation properties of EM waves due to the different barriers inside the GIS. This is done by obtaining the received power by each UHF sensor over frequencies ranging between 250MHz and 2GHz and comparing the obtained results.

The 3D-full Maxwell solver of COMSOL multi-physics has been used to build the GIS shown

in Figure 4.1, considering the full complexity of the structure. All inner and outer metallic components have been modeled as a perfect electric conductor (PEC) to reduce the computational time. PEC is modeled using [104]:

$$\mathbf{n} \times \mathbf{E} = 0, \tag{4.1}$$

where $\mathbf{E}$ represents the electric field intensity and $\mathbf{n}$ is a unit vector normal to the PEC boundary surface.

The time-harmonic electric field is numerically evaluated by solving the following in the do-

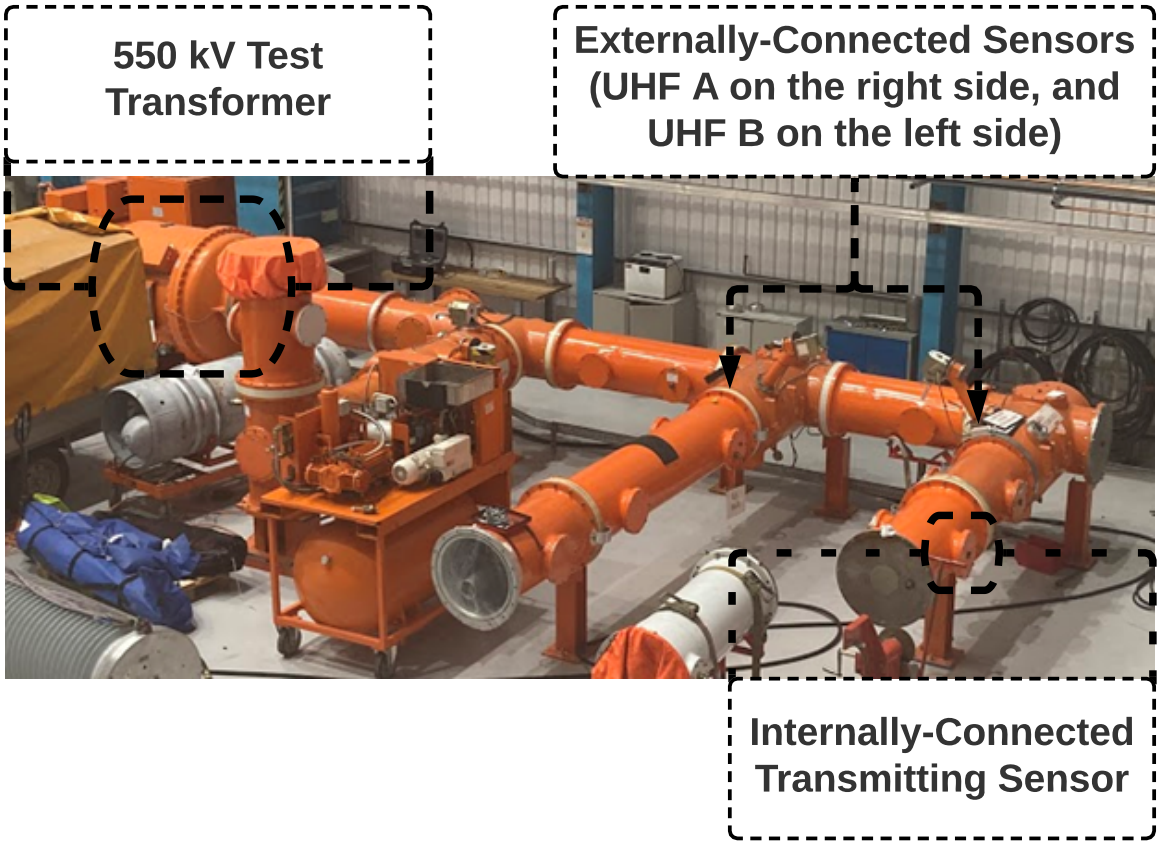

Figure 4.1: 550kV π-structure GIS System. A transmitting sensor, internally connected, is used to inject the PD-like signals whereas the 2 external sensors are used to capture the EM waves.

Figure 4.2: Externally connected sensor placement over the dielectric spacers connecting the different GIS tubes.

main R^3 [104]:

$$\nabla \times \left(\frac{1}{\mu_r} \nabla \times \mathbf{E} \right) - k_0 \left(\epsilon_r - \frac{j\sigma}{\omega \epsilon_0} \right) \mathbf{E} = 0, \tag{4.2}$$

where k_0 is the wavenumber in free space, μ_r is the relative permeability, σ is the electrical conductivity, ϵ_0 is the free space permittivity, and ϵ_r is the relative permittivity of the material. The electrical properties of the materials utilized in the model are summarized in Table 4.1.

All ports for the transmitting and receiving sensors are modeled using lumped port boundary condition using [105]:

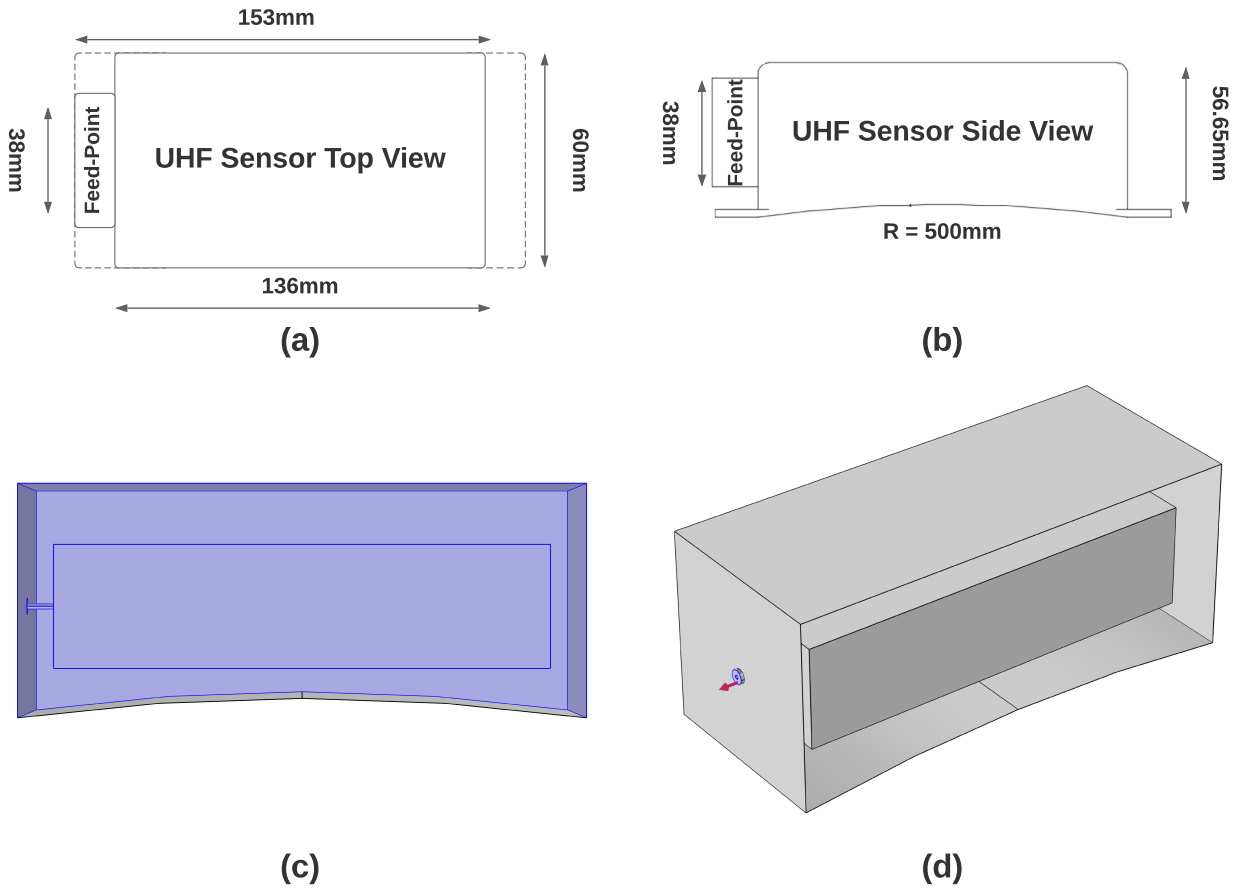

Figure 4.3: a) Top view of the external UHF sensor, b) side view of the external UHF sensor, c) 3D model of the utilized external sensor. All metallic parts are modeled using PEC (boundaries colored in purple), and d) coaxial lumped port used as a feed point (colored in purple). The used lumped port is equivalent to a BNC connector where both inner and outer conductors are modeled using PEC.

$$Z_{port} = \frac{V_{\text{port}}}{I_{\text{port}}}, \tag{4.3}$$

where Z_{port} represents the impedance seen at the port, V_{port} is the voltage measured at the port, and I_{port} is the current measured at the port. Coaxial port boundary condition has been utilized to represent the inputs and outputs to the internal and external UHF sensors. This boundary condition is used to excite or terminate an RF device with a specific impedance (50Ω in this model).

Finally, the test transformer and its section are not considered to reduce the complexity of the structure. Second-order scattering boundary condition (SBC) has been used instead to reduce the

Table 4.1: Used Electrical Material Properties in the Computational Model

Component	Conductivity (S/m)	Relative Permittivity	Relative Permeability
Insulating Gas (SF6)	2e-12*	1.00204	1
Dielectric Spacers	0	4.8	1
External UHF Sensors	0	2.6	1
UHF Sensors Connectors	0	2.1	1

reflections coming from that side. Such an assumption is valid given that the signal would mostly be attenuated by the time it reaches the test transformer and gets reflected. The agreement between measured and simulated results also verify that such an assumption does not significantly alter the results. SBC in COMSOL is modeled by:

$$\mathbf{n} \times (\nabla \times \mathbf{E}) - jk\mathbf{n} \times (\mathbf{E} \times \mathbf{n}) - \frac{1}{2jk_0} \nabla \times (\mathbf{nn} \cdot (\nabla \times \mathbf{E})) = 0, \tag{4.4}$$

where k is the material's wavenumber.

Figure 4.4 shows a schematic of the modeled GIS section and the placement of the external sensors (colored in purple in Figure 4.4(b)). A minimum number of five elements per wavelength (assuming a maximum frequency of 1.5GHz) has been utilized to mesh the GIS model. Consequently, a total number of 1,719,945 domain elements, 221,929 boundary elements, and 25,882 edge elements comprised the total number of elements required to model the GIS. Due to this vast number of elements, a total number of 8 frequency points has been simulated. The total simulation time is 1 hour, 29 minutes, and 35 seconds using Intel(R), Xeon(R), Gold 6138CPU @ 2GHz (40CPUs), 192GB RAM.

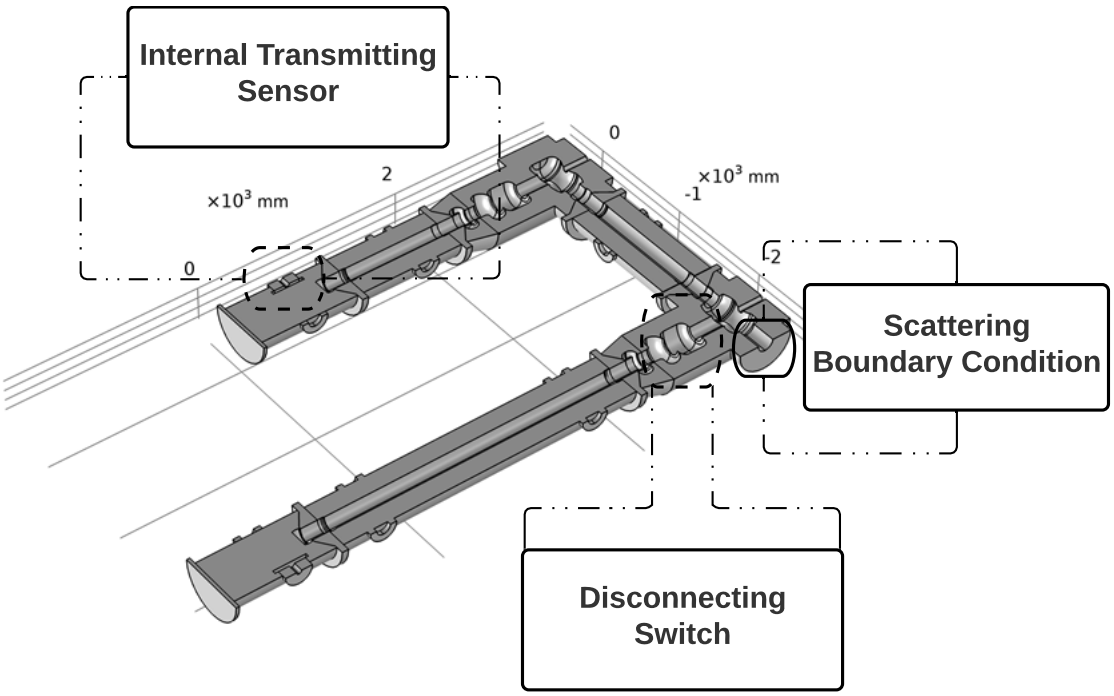

(a)

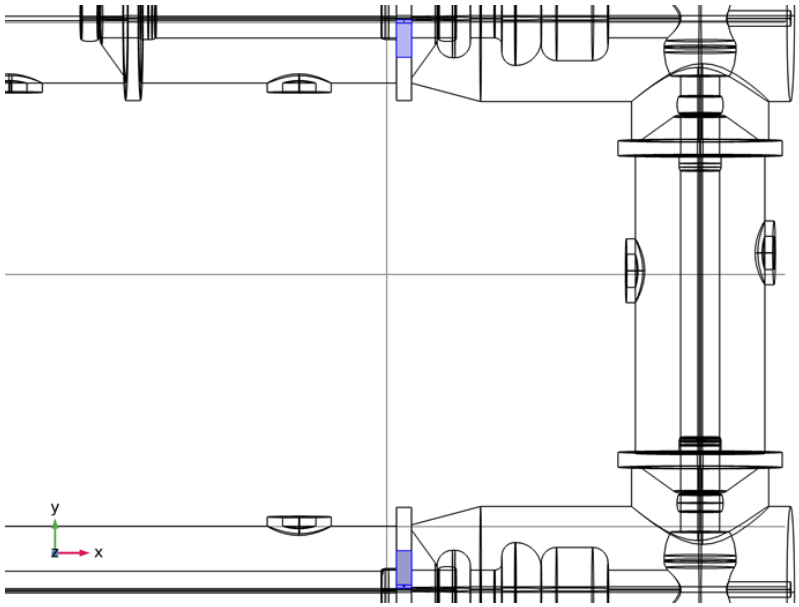

(b)

Figure 4.4: 3D schematic of the modeled GIS system. a) the full 3D structure, b) the external sensors placement (highlighted in purple).

4.3 FE Model Results

This section presents the electric field distribution at different frequencies inside the GIS chamber. Investigating the attenuation behavior at different frequencies helps determine the required distances between externally connected sensors to ensure that at least two UHF sensors can detect PD activities inside the GIS enclosure. Detecting PD activities using multiple sensors is significant to localize the source of PD defects using time difference of arrival (TDoA) or time of flight (ToF) localizing techniques. It should be noted that external sensors are usually placed on top of the dielectric spacers connecting the GIS tubes, limiting the locations at which UHF sensors are placed. Moreover, the electric field distribution helps show the frequency-dependent electric field intensity distribution inside the GIS enclosure. Finally, the resonances created within the GIS can also be visualized.

4.3.1 Closed Disconnecting Switch

In this section, the impact of opening and closing the disconnecting switches on the attenuation behavior of the EM waves is presented and discussed. Figures 4.5 - 4.8 show the electric field distribution at four different frequencies, namely 250MHz, 425MHz, 775MHz, and 1475MHz. The first cutoff frequency (TE11) for the simple tubes, where inner and outer diameters exist without sudden bends or radii change, is around 290MHz. The cutoff frequencies for the TE modes can be calculated using [96]:

$$f_c^{TE_{m1}} = \frac{v\ m}{\pi(a+b)}, \tag{4.5}$$

where v represents the propagating velocity within the space (close to the speed of light in SF6), a is the inner radius of the coaxial structure, and b is the outer radius.

Figure 4.5 represents the Transverse Electromagnetic (TEM) mode of the propagating EM waves. Minimal signal intensity can be observed from this figure as compared with the remaining plots near the internal (transmitting) sensor. It is seen that the transmitting signal is placed in a tube having a circular waveguide shape. TEM mode of propagation is not supported in such a waveguide

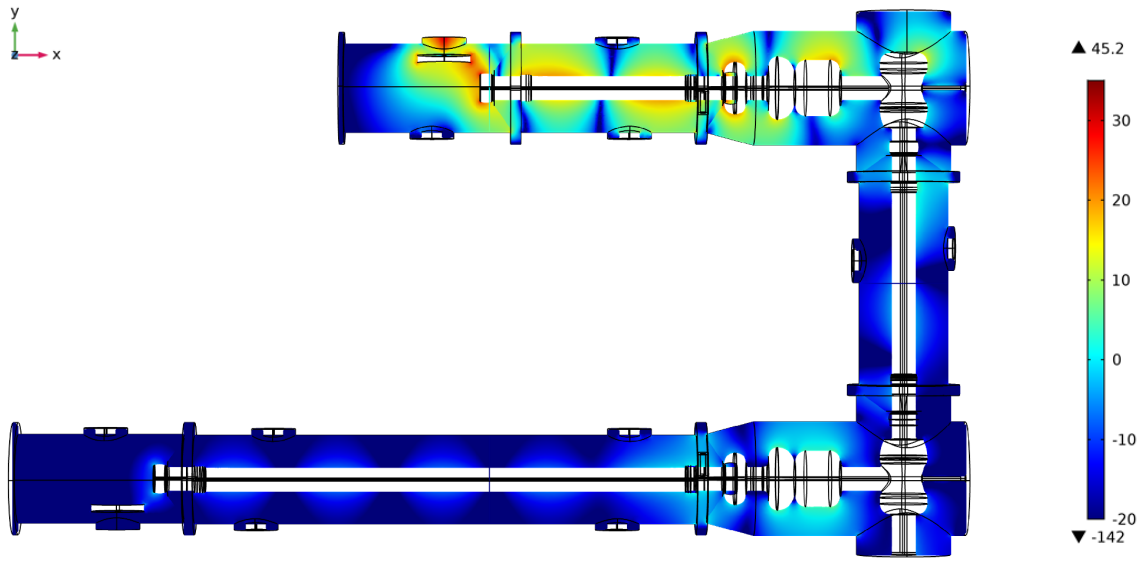

Figure 4.5: Electric field distribution inside the GIS model (closed disconnecting switch) at 250MHz.

since two electrodes are needed for TEM mode to propagate. Consequently, most of the signals at 250MHz would be attenuated as shown near the edge of the GIS (to the left of the transmitting sensor). It can be observed from Figure 4.5 that the intensity of the waves attenuates due to the bends and the dielectric spacers. This attenuation is also attributed to the many changes in the outer to inner diameters ratio within the GIS enclosure. All these factors cause multiple reflections within the GIS enclosure, weakening the signal as it propagates through the GIS. Nonetheless, the attenuation experienced by EM waves at this frequency due to the bends is not as significant as the 425MHz case where TE11 mode can be excited.

Figure 4.6 shows the electric field distribution at 425MHz. At such a frequency, TE11 mode can propagate within the GIS cavity. Circular waveguides support such a mode of propagation, and thus, the intensity of the EM signal is much higher than in the first case (Figure 4.5) near the transmitting sensor. Once EM waves reach the first bend, a considerable attenuation can be observed due to the significant reduction of the electric field intensity after the bend. TE11 mode is highly

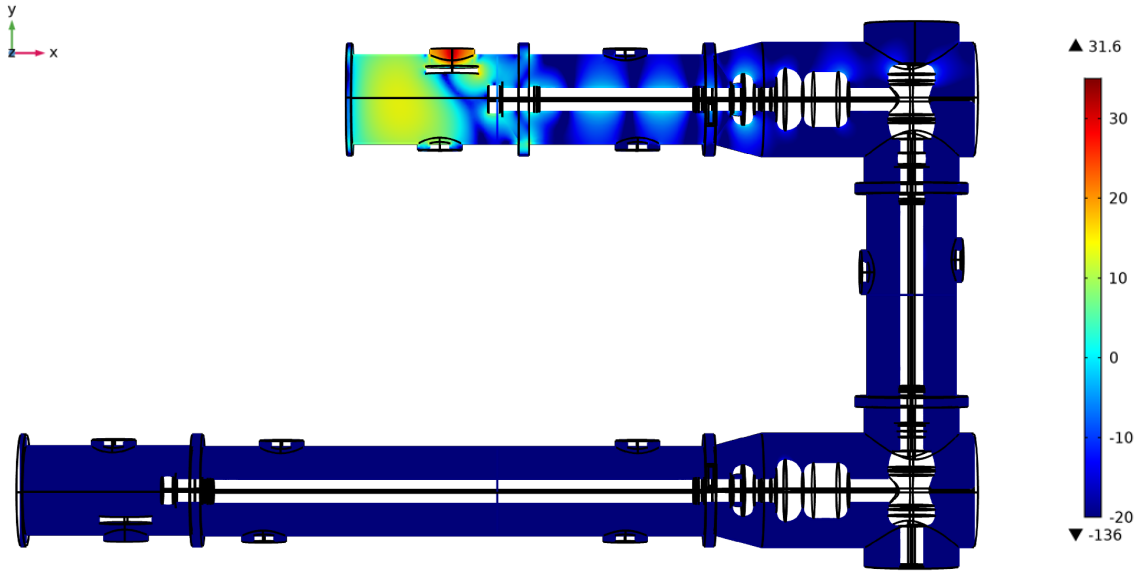

Figure 4.6: Electric field distribution inside the GIS model (closed disconnecting switch) at 425MHz.

dependent on the angular position between the PD source and sensor. When TE11 mode waves reach the bend, the inner conductor causes a significant reflection to such a mode of propagation, reducing its intensity after the bend.

Figure 4.7 shows the electric field distribution at a higher frequency. Many resonances are created within the GIS. Also, at higher frequencies, it becomes difficult to understand the behavior of such propagating waves. The two bends significantly impact EM waves at 775MHz, as depicted in Figure 4.7 (although not as significant as the 425MHz case). The dielectric spacers also affect the intensity of the waves in this case compared with the lower frequency ranges. The reduction of the EM waves due to the dielectric spacers is attributed to reducing the wavelength as the frequency increases. This would cause dielectric spacers to have a larger electrical length than the lower frequency ranges, trapping EM waves within the dielectric spacer and causing more reflections to the waves.

When the frequency is increased to 1475MHz, as depicted in Figure 4.8, the impact of the

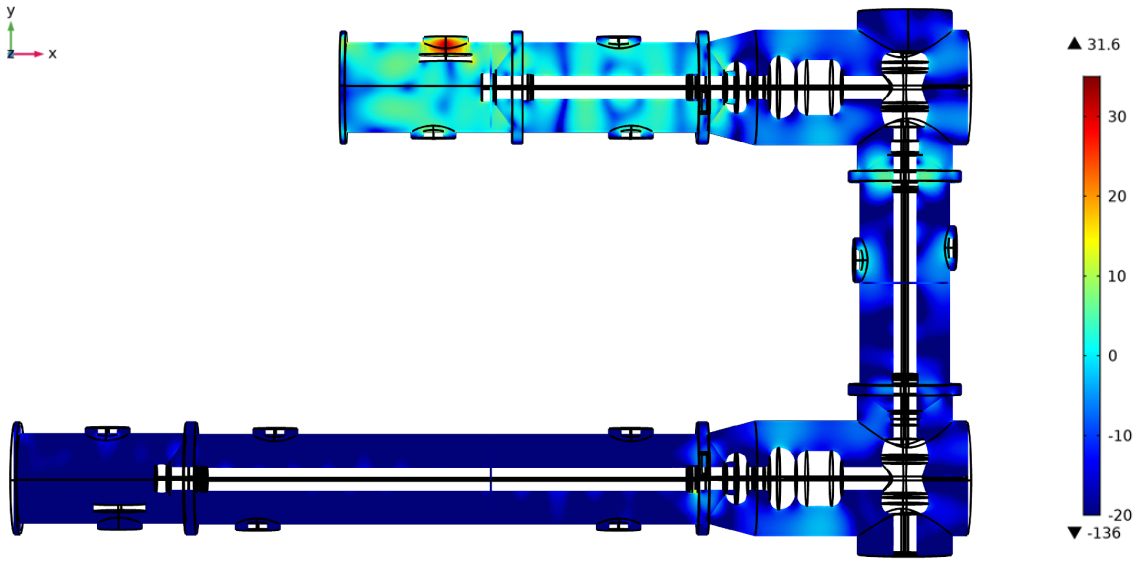

Figure 4.7: Electric field distribution inside the GIS model (closed disconnecting switch) at 775MHz.

first bend is vastly reduced. Such behavior is attributed to the propagation of Transverse Magnetic (TM) mode. In TM mode, longitudinal electric field components will be propagating, which acts as a source for the EM waves to propagate to the second part of the GIS. The large attenuation seen by the EM signals is mainly attributed to the dielectric spacers.

On the other hand, the EM wave intensity is largely reduced after the second bend, as can be perceived by Figure 4.8. This reduction is because most TM waves propagating before the first bend act as a source for the EM waves in the second section (between first and second bends). Nonetheless, most of the electric field components propagating in this section have radial electric field components. Hence, the second bend causes a significant reflection of the propagating waves before reaching the last section of the GIS (after the second bend).

Finally, it can be seen in Figures 4.5 - 4.8 that multiple changes in the outer to inner diameter ratios are taking place, especially near the bends and along the disconnecting switches. These changes contribute to the reflections happening within the GIS model due to the changes in the

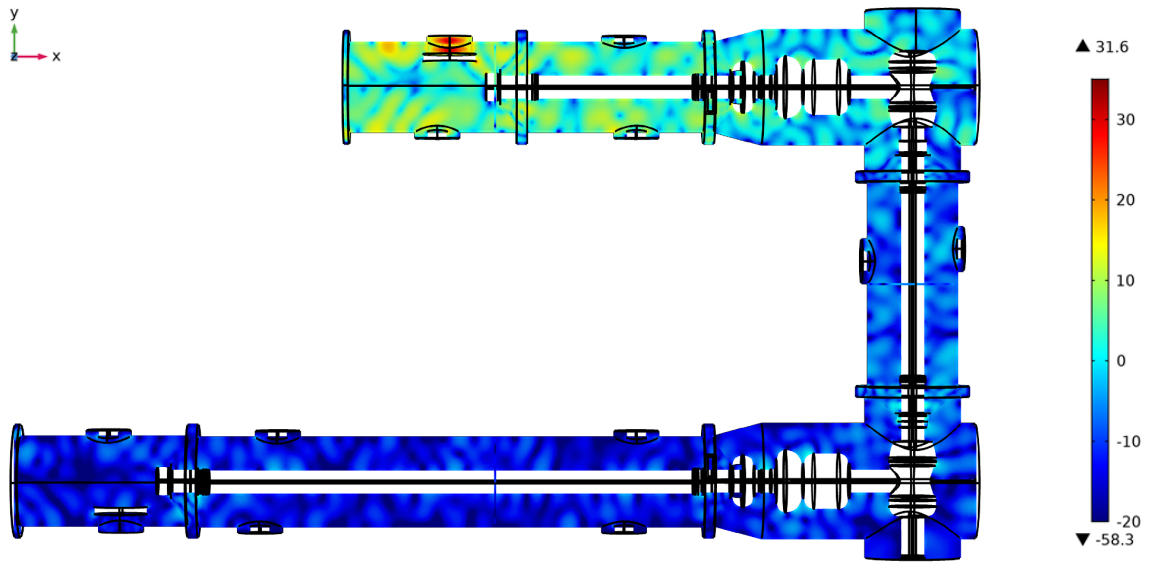

Figure 4.8: Electric field distribution inside the GIS model (closed disconnecting switch) at 1475MHz.

characteristic impedance of the coaxial cable. All these factors and the fact that the GIS is a metallic encapsulated structure contribute to the multiple resonances created within the GIS. Fully comprehending the propagation of EM waves within GIS structures can be cumbersome, and considering GIS systems as simple waveguides cannot provide accurate insight on the UHF wave analysis.

4.3.2 Open Disconnecting Switch

Figures 4.9 and 4.10 show the electric field distribution within the GIS when the disconnecting switch is open. The electric field is shown at two frequencies only: 250MHz and 1475MHz. The reason for not showing 425MHz and 775MHz is attributed to the fact that the EM wave intensity is low at these two frequencies even when the disconnecting switches are closed. Thus, no additional information has been added at these two frequencies.

Figure 4.9 shows that the intensity of the electric field at 250MHz. It is seen that a rapid attenuation to the EM waves has been experienced. When the disconnecting switches are open, the

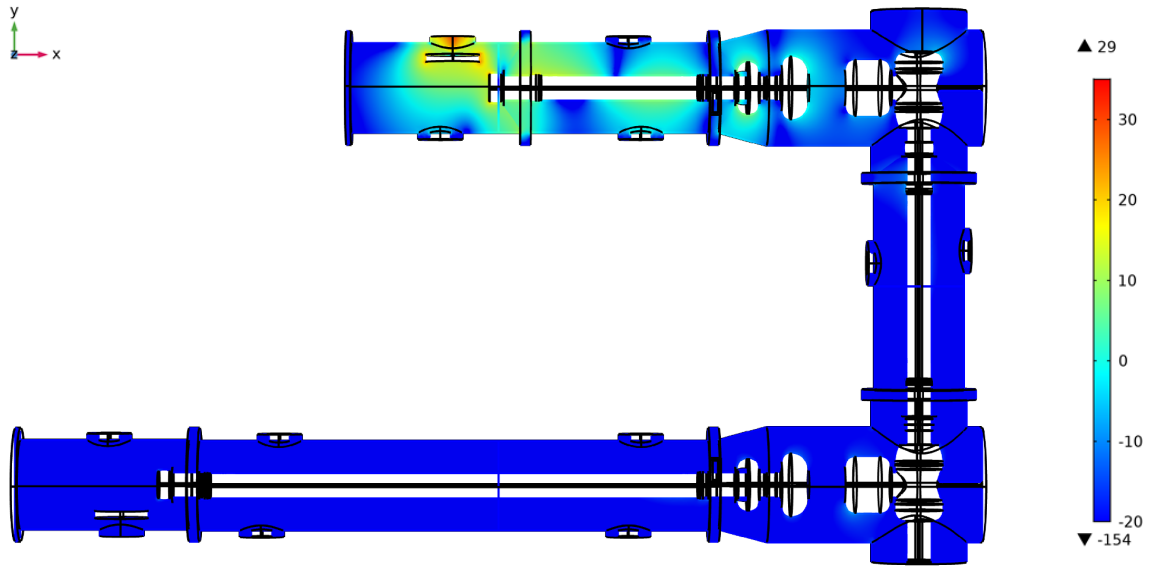

Figure 4.9: Electric field distribution inside the GIS model (open disconnecting switch) at 225MHz.

coaxial waveguide structure would be changed to a circular waveguide. TEM mode of propagation does not support the propagation of such waves. Thus, waves would experience reflections and attenuation when they reach a disconnecting switch. The electric field distribution before the first disconnecting switch is similar to that of the first scenario (closed disconnecting switch).

Figure 4.10, on the other hand, presents the electric field distribution at 1475MHz. The electromagnetic wave intensity is still high even after the disconnecting switch. This is attributed to the fact that at such a high frequency, higher-order modes will be propagating inside the GIS. Such modes of propagation can propagate in circular waveguides. Thus, the attenuation and reflections experienced by the TEM mode alone will not be clear in this case as in the previous case.

4.4 Impact of Barriers on EM Wave Propagation

To better understand the effect of the barriers mentioned above, their impact on the propagation of EM waves is discussed in this section. Time-domain simulations have been utilized in this section. Modulated Gaussian pulses at two different frequencies, namely 250MHz, and 800MHz

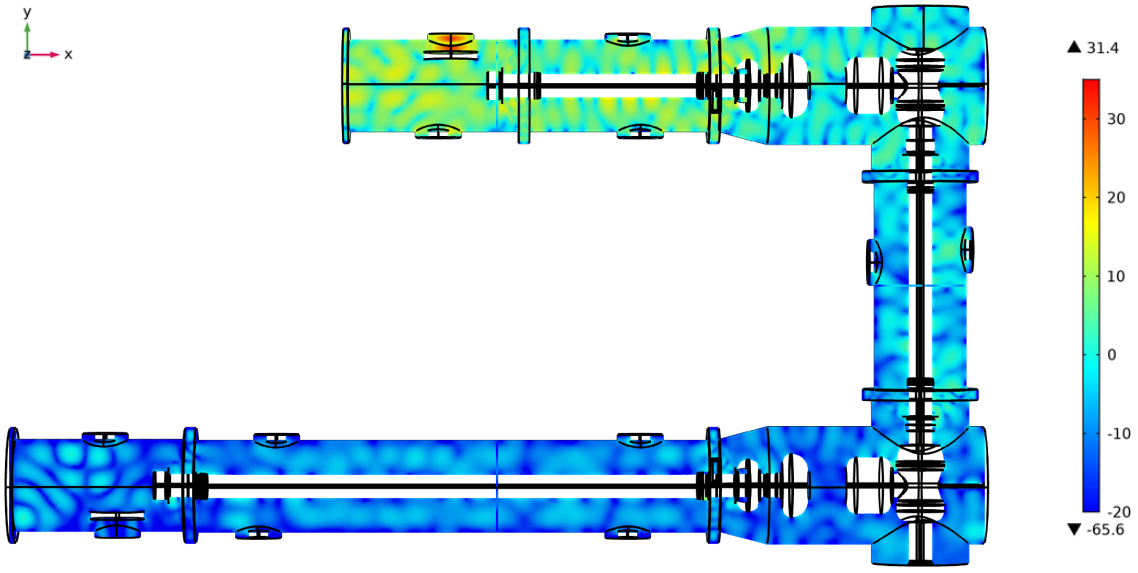

Figure 4.10: Electric field distribution inside the GIS model (open disconnecting switch) at 1475MHz.

are injected into the different GIS sections.

Figure 4.11 shows the modeled GIS sections. Port 1 is used as the input to the modulated Gaussian pulses, whereas port 2 is matched to the coaxial structure to absorb incoming waves. Each of the models shown in Figure 4.11 is discussed separately in this section. It should be noted that the utilized simulation time is 100ns to ensure that most of the signal has either been fully reflected or transmitted. Nonetheless, Figures 4.12-4.15 are plotted over 60ns to visualize the results properly. To have better quantitative measure of the obtained results, the cumulative energy of the reflected and transmitted signals are obtained using:

$$CE = \int_a^b p(t)\, dt \tag{4.6}$$

where a and b are 16ns and 100ns for all scenarios to measure the reflected signal. On the other hand, a is 0ns, and b is 100ns for evaluating the cumulative energy of the transmitted signals. Then, the reflected and transmitted portions of the different signals are obtained and tabulated in Table

4.2.

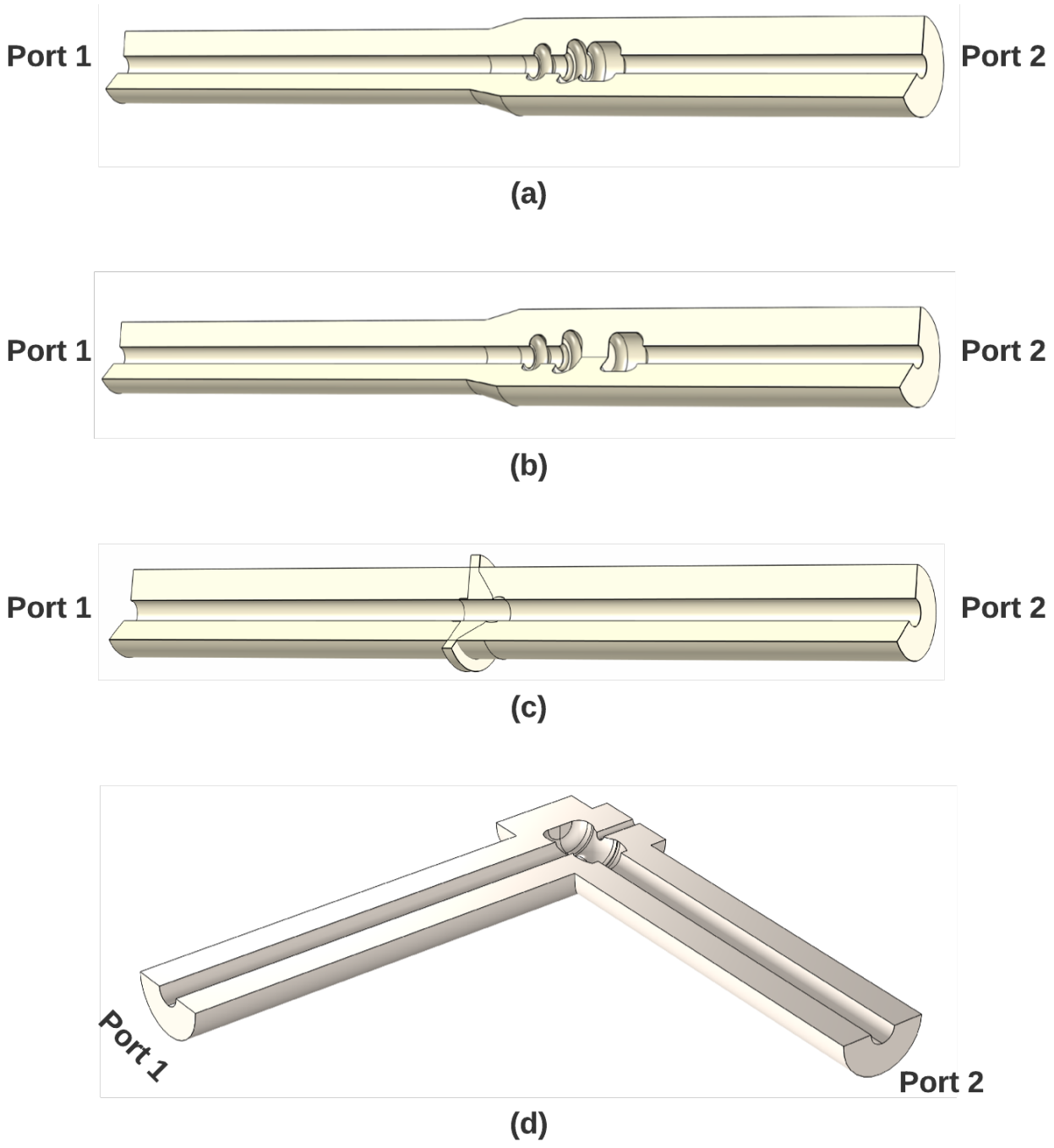

Figure 4.11: Modeled GIS sections with a) changes in the inner and/or outer diameters, b) open disconnecting switches, c) dielsctric spacers, and d) L-bend.

4.4.1 Change of Outer to Inner Diameter Ratios

Figure 4.12(a) and Figure 4.12(b) show the simulated power magnitude sensed at port 1 (upper plots), whereas Figure 4.12(c) and Figure 4.12(d) show the power magnitude sensed by port 2 (lower plots). It can be seen that reflections are taking place at all selected frequencies. The reflection is attributed to the change in the characteristic impedance of the coaxial transmission line, causing reflections to part of the signal. A large portion of the signal is transmitted at 250MHz. This can be attributed to the large electrical size associated with 250MHz. Hence, the multiple changes in the outer to inner diameter might not be fully perceived by the EM signal at such a frequency, and the reflected signal would be equivalent to minor changes in the characteristic impedance.

On the other hand, multiple reflections due to the changes in the characteristic impedance are seen when the frequency is increased. Having said that, many more reflections are perceived by the EM waves. The electrical size gets smaller at higher frequencies, causing more reflections due to the multiple changes in the characteristic impedance. Table 4.2 shows that the reflected portion of the signal is higher when the frequency is 800MHz.

4.4.2 Disconnecting Switch

Figure 4.13 shows the power magnitude sensed by the ports when a disconnecting switch exists (refer to Figure 4.13(b)). It can be seen that high portion of the EM waves are reflected for 250MHz. Moreover, a small portion of the signal will propagate after the switch to reach the second port (receiving end). TEM mode of propagation cannot freely propagate when a disconnecting switch exist since, as previously mentioned, circular waveguides do not support the propagation of TEM mode.

On the other hand, higher-frequency signals can propagate within the GIS, even if open disconnecting switches exist. When such waves hit the disconnecting switch, the reflected portion is lower than the first case since waves can, in this case, adapt to propagate even in the existence of circular waveguide structures. The transmitted portion is hence much higher as compared with the

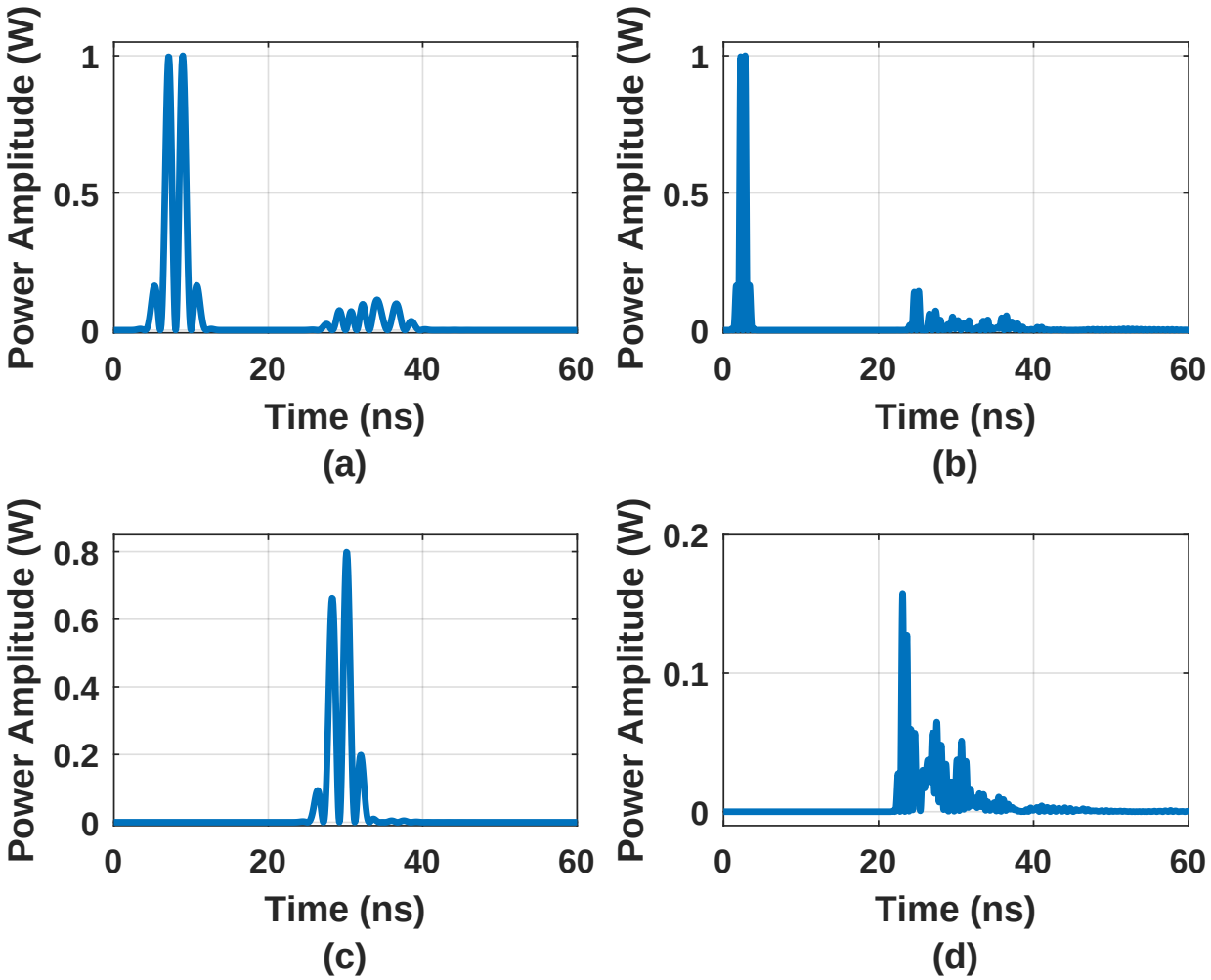

Figure 4.12: Power magnitude received by port 1 (upper plots) and port 2 (lower plots) at 250MHz, and 800MHz when a change of outer to inner diameter ratios exists. a) Input and reflected signal seen by port 1 at 250MHz, b) Input and reflected signal seen by port 1 at 800MHz, c) Transmitted signal seen by port 2 at 250MHz, and d) Transmitted signal seen by port 2 at 800MHz.

first case (250MHz). Although Figure 4.13 shows that the transmitted portion at 800MHz is low, this reduction is mainly attributed to the sudden changes in the characteristic impedance (as in the previous case). Table 4.2 shows the reflected and transmitted cumulative energy portion due to an open disconnecting switch. By comparing the results with the closed disconnecting switch (previous case), it can be seen that higher-frequency signals are not largely affected by the disconnecting switch, whereas the low-frequency EM waves experience significant reflection.

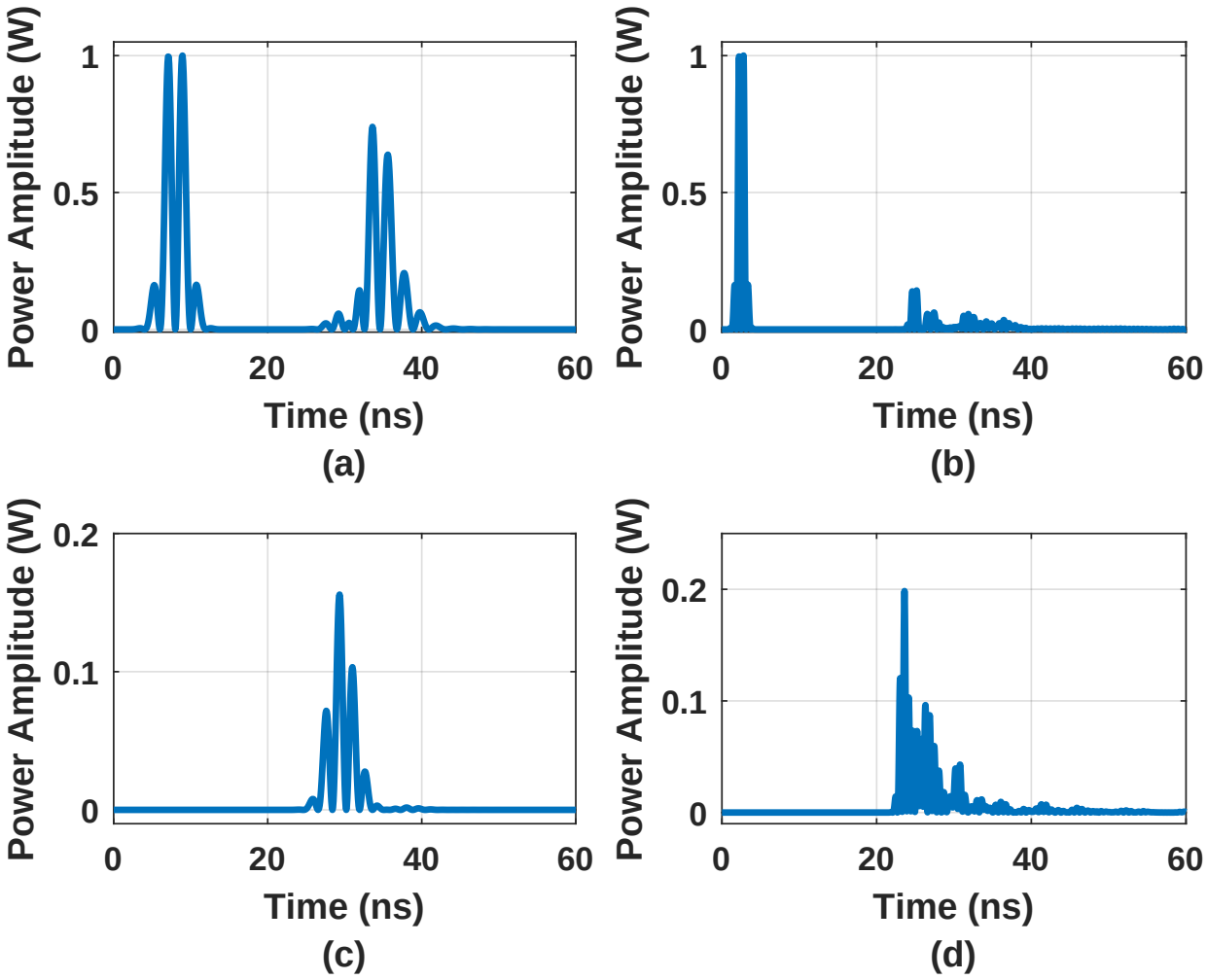

Figure 4.13: Power magnitude received by port 1 (upper plots) and port 2 (lower plots) at 250MHz, and 800MHz when a disconnecting switch exists. a) Input and reflected signal seen by port 1 at 250MHz, b) Input and reflected signal seen by port 1 at 800MHz, c) Transmitted signal seen by port 2 at 250MHz, and d) Transmitted signal seen by port 2 at 800MHz.

4.4.3 Dielectric Spacer

Figure 4.14 shows the impact of dielectric spacers on the reflected and transmitted power magnitude at different modulation frequencies (i.e., 250MHz and 800MHz). The permittivity of the dielectric spacer is different from SF6. Hence, the characteristic impedance will be different over the dielectric spacer as compared with the coaxial structure. Figure 4.14 shows that the Gaussian pulse at 250MHz and 800MHz is transmitted, and a small portion is reflected. The reflected por-

tion of the signal in both cases is proportional to the reflection coefficient due to the change in the characteristic impedance.

It should be noted that part of the signal is trapped inside the dielectric spacer causing multiple peaks to be detected by ports 1 and 2. The trapped portion stays longer inside the dielectric spacer at higher frequencies. Hence, the maximum sensed power amplitude is lower at higher frequencies, but the signal attenuates at a slower rate. Hence, high-frequency signals are more susceptible to dielectric spacers due to the smaller electrical size of waves. Table 4.2 shows that the reflected and

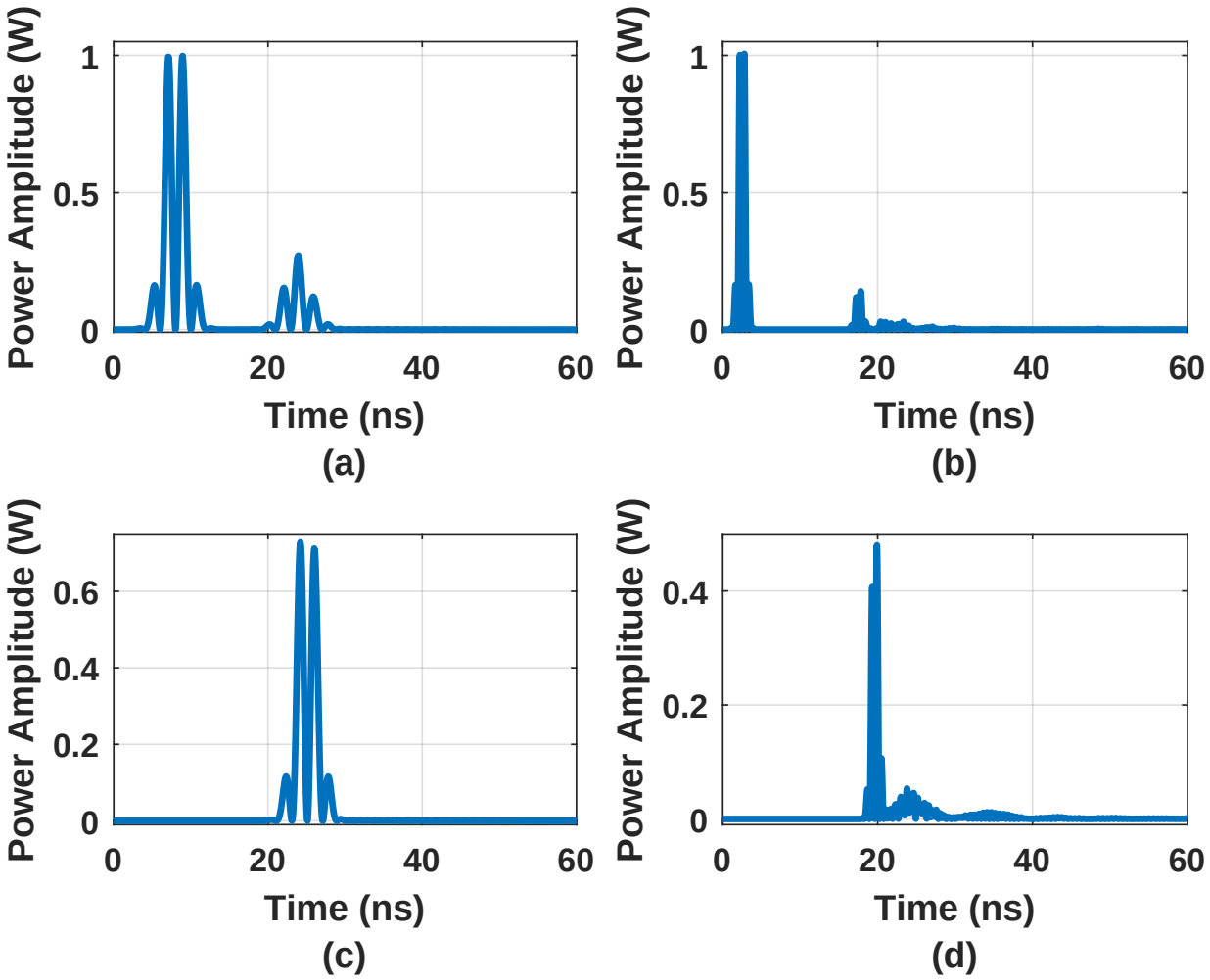

Figure 4.14: Power magnitude received by port 1 (upper plots) and port 2 (lower plots) at 250MHz, and 800MHz when a dielectric spacer exists. a) Input and reflected signal seen by port 1 at 250MHz, b) Input and reflected signal seen by port 1 at 800MHz, c) Transmitted signal seen by port 2 at 250MHz, and d) Transmitted signal seen by port 2 at 800MHz.

transmitted portions of EM signals are similar at 250MHz and 800MHz.

4.4.4 L-Bend

Finally, the impact of the L-Bend on the propagating EM waves is investigated using the modulated Gaussian pulses at the frequencies mentioned above. It can be seen that an L-bend has a significant impact on both low and high-frequency EM signals. This is mainly attributed to the metallic inner and outer conductors facing the propagating EM waves. An L-bend barrier causes the most significant overall attenuation to the EM waves compared with the barriers mentioned above (except the open disconnecting switch for TEM mode of propagation). Table 4.2 shows that the transmitted and reflected portions of the signal are similar for both 250MHz and 800MHz.

It can be observed that the reflected signal attenuation factor is, in general, slower at higher frequencies, as depicted from Figures 4.12-4.15. Such behavior can be attributed to different factors. Such factors include the electrical size of the EM waves. Smaller electrical size causes EM waves to detect smaller objects inside the enclosure. Hence, more reflections are perceived at higher frequencies. Another critical factor that causes the slower attenuation of EM waves is the dispersion effect. Higher-order EM waves can be slower than the TEM mode of propagation. The velocity of the TE modes is obtained using:

$$v_{\text{TE}} = c\sqrt{1 - \left(\frac{f_c}{f}\right)^2} \tag{4.7}$$

where f_c represents the cutoff frequency of a certain TE mode, f is the frequency of operation, and c is the speed of light.

4.5 Experimental Setup and Results

4.5.1 Experimental Setup

A 0dB wideband (0.250GHz-2GHz) input signal is injected into the internally connected sensor using a wideband RF signal generator, as shown in Figure 4.16. After injecting the input signals to the GIS, EM waves start propagating within the GIS enclosure. Then, the externally connected sensors (refer to Figure 4.2) will be used to detect the EM wave intensity to obtain the power (dBm)

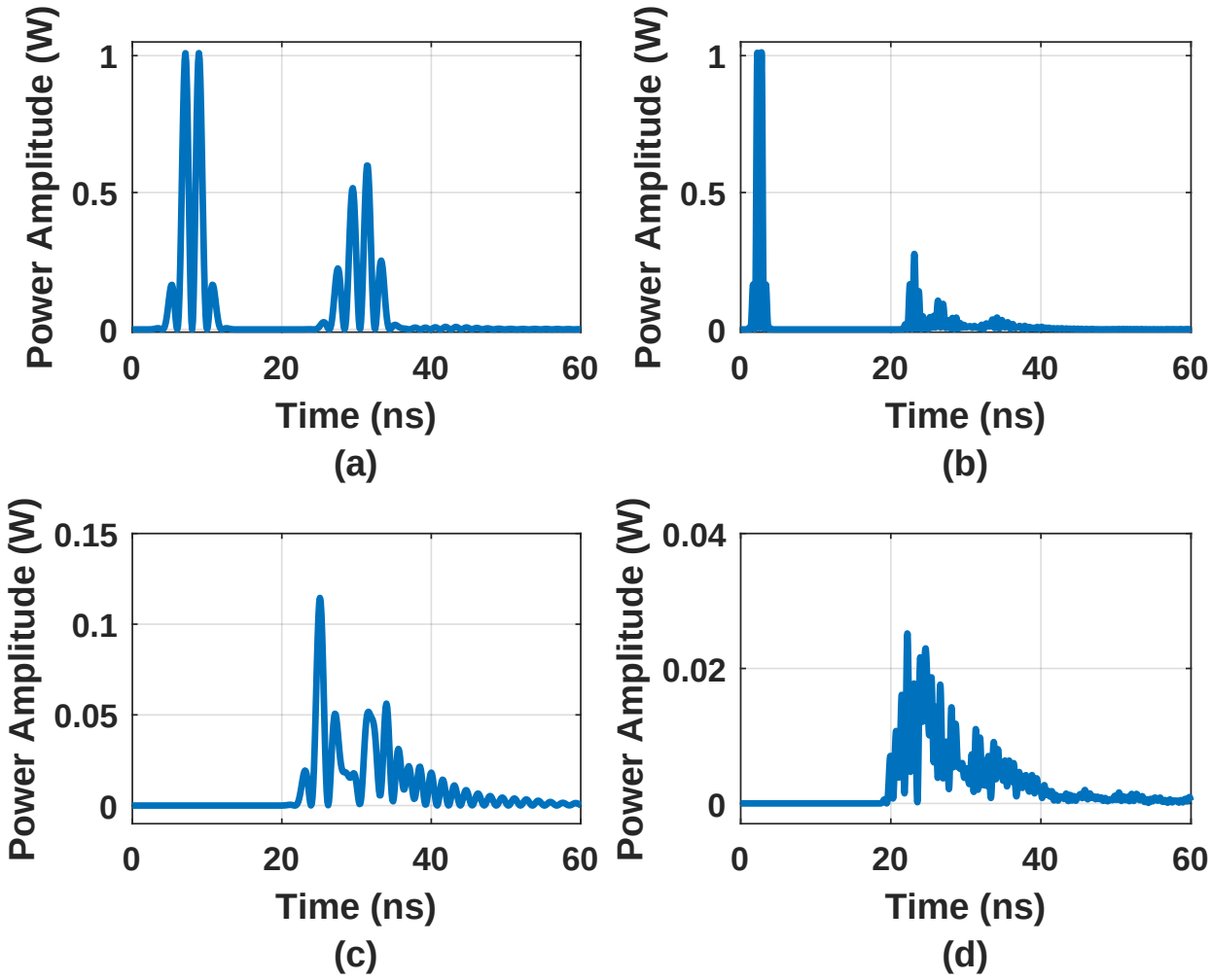

Figure 4.15: Power magnitude received by port 1 (upper plots) and port 2 (lower plots) at 250MHz, and 800MHz when an L-bend exists. a) Input and reflected signal seen by port 1 at 250MHz, b) Input and reflected signal seen by port 1 at 800MHz, c) Transmitted signal seen by port 2 at 250MHz, and d) Transmitted signal seen by port 2 at 800MHz.

as s function of frequency.

After injecting the EM waves to the internally connected signals, A network analyzer (Figure 4.16(a)) was used to display the obtained results. The power received by each sensor over frequencies ranging between 0.25GHz-2GHz has been obtained.

Table 4.2: Received EM Wave Intensity, Measured and Simulated Cases, under Different Disconnecting Switch States

Frequency (MHZ)	**Power Portion (%)**			
	Reflected Portion of Signals			
	Change of diameter ratio	Open Disconnecting Switch	Dielectric Spacers	L-Bend
250	21.54%	85.23%	26.03%	75.57%
800	50.69%	46.06%	25.83%	72.56%
	Transmitted Portion of Signals			
	Change of diameter ratio	Open Disconnecting Switch	Dielectric Spacers	L-Bend
250	77.24%	14.52%	72.27%	23.15%
800	46.82%	51.97%	72.24%	24.31%

Figure 4.16: Experimental Setup for injecting a 0dB input signal to the GIS. a) Wideband signal generator, and b) location of the internally connected sensor used to allow EM waves to propagate within the GIS.

4.5.2 Experimental Results and Discussion

The power received by UHF A and UHF B has been obtained and is presented in Figure 4.17 and Figure 4.18. Table 4.3 shows a comparison between measured and simulated power received by the two external UHF sensors. By inspecting the results of Table 4.3, a considerable agreement between most measured and simulated results is observed, which verifies the accuracy of the model. It should be noted based on Figure 4.17 and Figure 4.18 that the noise floor is around -55dBm. The simulated results showed that some values are lower than the noise floor since noise is not considered in the FE model. To avoid a large discrepancy in the obtained results, if the simulated value is less than the noise floor, the value is mentioned as less than -55dBm. On the other hand, the 600MHz frequency point has a sudden jump, as depicted in Table 4.3 and Figure 4.17. Such a jump results from external sources of interference. Nonetheless, the remaining readings show high agreement, which verifies the accuracy of the model. This also indicates that the obtained results are reasonably accurate even for the first few points since the external UHF sensor sensitivity is very low at frequencies below 500MHz. It should be noted that the measured values of Table 4.3 can be obtained from Figure 4.17 and Figure 4.18.

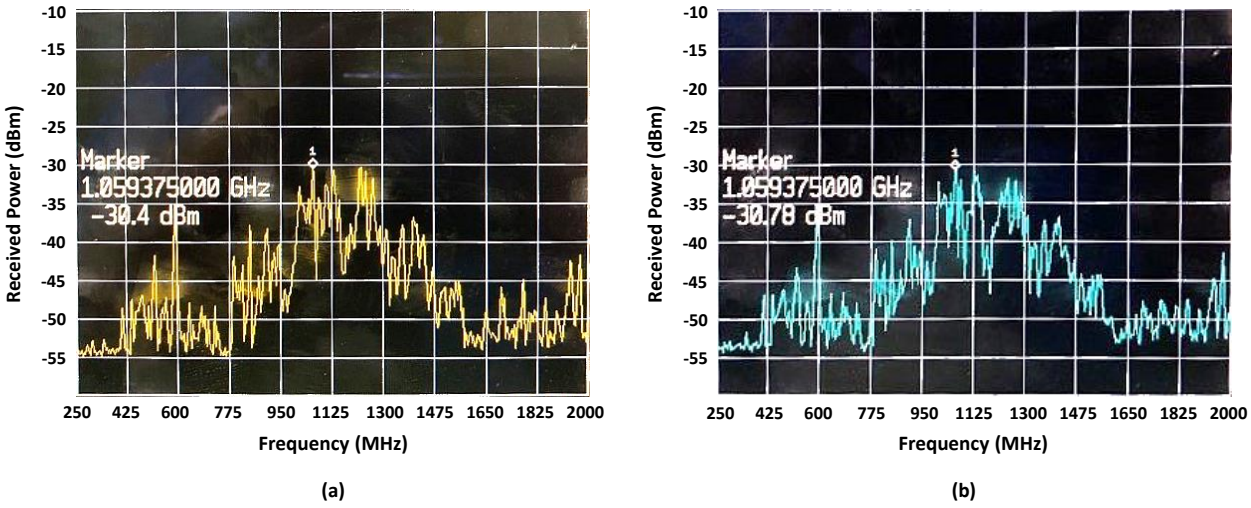

Figure 4.17: Captured EM wave intensity (dBm) by UHF A when a) disconnecting switches are closed, b) disconnecting switches are open.

Table 4.3: Received EM Wave Intensity, Measured and Simulated Cases, under Different Disconnecting Switch States

Frequency (MHZ)	**Acquired Power (dBm)**			
Closed Disconnecting Switch				
	UHF Sensor A		**UHF Sensor B**	
	Measured	Simulated	Measured	Simulated
250	-55	<-55	-54	<-55
425	-54	<-55	-54	<-55
600	-37	<-55	-54	<-55
775	-55	<-55	-54	<-55
950	-41	-49	-48	<-55
1125	-29	-29	-49	-40
1300	-42	-34	-45	-41
1475	-43	-34	-53	-47
Open Disconnecting Switch				
	UHF Sensor A		**UHF Sensor B**	
	Measured	Simulated	Measured	Simulated
250	-54	<-55	-54	<-55
425	-53	<-55	-54	<-55
600	-35	<-55	-45	<-55
775	-50	<-55	-54	<-55
950	-48	-49	-54	<-55
1125	-32	-30	-50	-36
1300	-40	-34	-49	-43
1475	-43	-43	-54	-51

By inspecting the results of Table 4.3, it can be seen that there are slight variations between the simulated and measured results. Many factors might contribute to such variations in the reported results. First, the electrical parameters reported in Table 4.3 might experience some slight variations in reality due to the temperature, pressure, or frequency variations (frequency-dependent electrical parameters are not considered). Such variations can cause slight alteration in attenuation, reflection, or transmission of the propagating EM waves. Moreover, some details of the external

and internal sensors were not fully provided (Like exact dimensions and shapes of the sensors, especially the internal sensor). Hence, some discrepancies in the sensitivity of the sensors exist, causing some variations in the obtained results. On the other hand, utilizing certain boundary conditions in the simulation model, which are used to simplify the FE model, is an essential factor contributing to the slight discrepancy in the obtained results. To exemplify, utilizing the SBC boundary condition absorbs most incident waves to model an open boundary (EM waves pass with no or minimal reflections). The actual GIS extends to reach the test transformer, as depicted in Figure 4.1. Although such parts are far from the PD source (input signal source), some reflections might exist due to such an extension. Finally, the complicated behavior of the EM waves within the GIS due to the multiple and sudden variation on the received power at different frequencies can also contribute to slight variations. In other words, a small change or variation in the frequency of operation can cause a significant change in the received power.

Figure 4.17 shows the power received by UHF A over frequencies ranging from 250MHz-2GHz when the disconnecting switches are closed (Figure 4.17(a)) and open (Figure 4.17(b)). The multiple peaks and dips seen on the received signals are attributed to the fact that a GIS acts as a cavity resonator since the GIS comprise an encapsulated hollow metallic structure.

As depicted from Figure 4.17, the overall behavior of the obtained results is similar, with variations in the amplitude depending on the state of the disconnecting switch. To illustrate, in both scenarios, an overall increase in the power above the noise floor can be seen at frequencies above 775MHz, reaching the maximum power at about 1125MHz. Then the overall power starts decreasing beyond 1125MHz. The similar overall behavior can be attributed to the location of UHF A with respect to the disconnecting switches. The UHF sensor lies before the disconnecting switches (refer to Figure 4.4). A significant signal attenuation is caused by the disconnecting switches (especially at lower frequencies). Hence, the power received by the UHF sensor, which lies before the disconnecting switches, is expected to be varied only due to the reflected portion of the EM waves. The reflected portion of the EM waves causes the differences in the peaks and dips amplitude perceived by Figure 4.17. Having said that, no significant change in the received

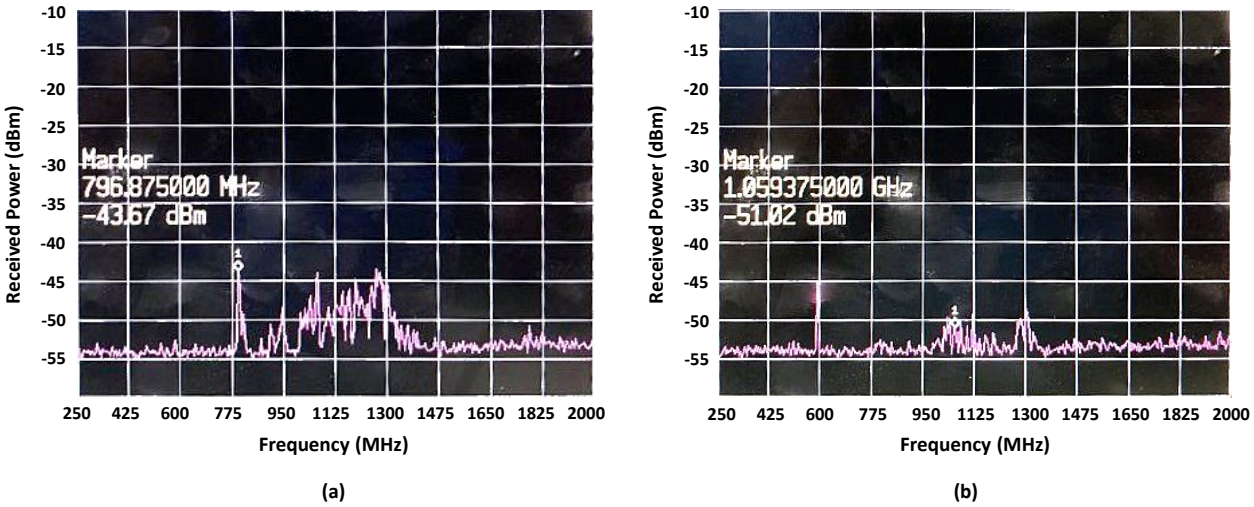

Figure 4.18: Captured EM wave intensity (dBm) by UHF B when a) disconnecting switches are closed, b) disconnecting switches are open.

power's overall behavior is expected, as seen in Figure 4.17.

It can also be seen that the sensor's frequency response is centered at around 1125MHz. The UHF sensor receives its maximum power at its center frequency, and an overall decay of the received power if it is more significant than or less than the center frequency. Moreover, a sudden peak at 600MHz can be seen as well. This peak can be attributed to different sources of external interference, including land mobile and broadcast applications.

Figure 4.18, on the other side, shows the power received by UHF B when the switches are closed (Figure 4.18(a)) and open (Figure 4.18(b)). A significant discrepancy in power can be seen by comparing Figure 4.18(a) and Figure 4.18(b). The main reason for such a difference is the attenuation experienced by the EM waves when the disconnecting switches are opened. Figure 4.18(b) shows that EM wave intensity is barely above noise floor over minimal frequency ranges. Based on these obtained results of Figure 4.17 and Figure 4.18, the impact of opening a disconnecting switch on the propagating EM waves for a sensor placed before the disconnecting switch is not as significant as that of a sensor located after the disconnecting switch.

By comparing the results of Figure 4.17 and Figure 4.18, it is seen that the EM wave intensity has experienced a significant attenuation. Such attenuation is attributed to the different barriers

seen by the EM waves before reaching UHF B. Such barriers include the two bends, two additional dielectric spacers, and multiple changes in the characteristic impedance of the GIS due to the changes in the outer to inner diameters ratios. These three factors have contributed to signal attenuation and multiple reflections to the propagating EM waves, reducing the signal intensity as depicted by the power received by the external couplers.

4.6 Conclusion

In this study, the impact of different barriers, including 90° bends, sudden changes in the outer to inner diameter ratios, dielectric spacers, and disconnecting switches on the attenuation properties of the EM signals, has been analyzed using a 550kV GIS. Experimental and simulated results have been presented and discussed to provide better insight into the propagating EM waves and improve the utilization of UHF sensors in PD detection. This work is the first trial to model a GIS to the full complexity while utilizing external UHF sensors, to the best of authors' knowledge. Most existing FE and FDTD based studies rely on internal detection in modeling. The following concluding remarks have been drawn based on this work:

- External sensors are more susceptible to noise as compared with the internally connected counterparts.
- External UHF sensors can be used in PD detection in both old and new GIS enclosures.
- The propagating waves experience multiple reflections and attenuation as they propagate within the GIS due to the different barriers within the GIS.
- Low frequencies are less susceptible to dielectric spacers as compared with the higher frequency ranges. This is attributed to the fact that when the frequency increases, the wavelength decreases and becomes more and more comparable to the size of the dielectric spacer. Hence, high frequency signals can be trapped within the dielectric spacers, causing more reflections over time.
- Sudden changes in the outer to inner diameters ratios cause changes in the characteristic

impedance, and thus, EM waves experience reflections. High-frequency EM waves experience higher reflection rate due to the electrical size.

- Disconnecting switches cause large attenuation to the TEM mode of propagation, and lower attenuation (or reflections) to the higher-order modes of propagation. When the disconnecting switch is open, the GIS is perceived by the EM waves as a circular waveguide rather than a coaxial waveguide, which does not support the propagation of TEM mode.

- L-bends have a significant impact on the propagating EM waves. Such reflections are usually high for both low-frequency and high-frequency waves (although it can be higher if TE11 mode is excited).

- GIS systems cannot be simply treated as simple coaxial/circular waveguides for UHF detection applications. The different existing barriers within such capital assets cause multiple reflections and attenuation within the GIS enclosure complicating the propagating EM wave behavior.

- As the frequency of operation increases, more resonances are created within the GIS, as perceived by the multiple dips and peaks seen in the captured EM waves by the external sensors and electric field distribution.

5. A SIZE REDUCTION METHODOLOGY FOR STRUCTURALLY SYMMETRICAL PD-BASED WIDEBAND UHF ANTENNAS

Testing high voltage (HV) devices using ultra-high frequency (UHF) sensors have been predominantly employed for decades due to the high sensitivity and immunity to the noise of UHF techniques in detecting, localizing, and classifying various partial discharge (PD) defects. This work reports on implementing and testing a coplanar waveguide (CPW)-fed annular monopole antenna for PD detection. The 3D Maxwell solver of COMSOL multi-physics has optimized the antenna parameters and improved its performance. The original size of the antenna has been reduced by about 47% utilizing structural symmetry and current resonances. The radiation pattern and the reflection coefficient of the proposed sensor are obtained using an anechoic chamber. The antenna exhibits a wide bandwidth over frequencies ranging between 0.5-3GHz with three notches at 0.6GHz, 1.2GHz, and 2.75GHz (based on measurements). The proposed sensor shows an overall increase, as a function of frequency, in the gain with a peak value of 6.25dBi at 2.75GHz. The antenna ability to detect external discharges has been tested against corona discharge, generated by applying 6-12kV between a sharp conductor and a ground plane. All obtained results show that the antenna is an effective tool in PD detection.

5.1 General Overview

Different types of UHF-based antennas have been proposed and used for PD detection. Horn antennas, log-periodic antennas, dipole antennas, and loop antennas comprise some examples of the most used UHF sensors [75]. On the other hand, the rapid growth of planar antennas as compact, efficient, and low-cost devices has dramatically increased their demand for PD detection. Nonetheless, patch antennas do not attain a large bandwidth (BW) required for the Ultra-Wide Band (UWB) applications. Thus, researchers have come up with many different approaches to increase the BW of such antennas. Spiral, Hilbert, and Moore fractal antennas exhibit wide bandwidth and have recently been utilized for PD detection [78, 104, 106]. For internal PD detection in

GIS and transformers, disk-type antennas are used, and the antenna factor (AF) is usually obtained to verify that the antenna sensitivity is sufficient to detect PD activities [91]. The AF is usually obtained using a gigahertz transverse electromagnetic test cell [102].

Unlike the miniaturized antennas utilized in communications, fulfilling the compact yet wide-band antenna requirements for PD detection is not an easily attainable task. This is attributed to the low starting frequency at which the antenna should be operating (300MHz to 3GHz). Tremendous efforts have been made to improve PD UHF antennas bandwidth and ascertain their robust PD detection performance [85]. Among these, L. Yang *et al.* proposed that using antenna arrays can improve the overall gain of antennas [107]. On the other hand, adding tuning nodules to the spiral antenna has recently shown a significant bandwidth improvement [104].

This chapter presents the development, implementation, and testing of a CPW-fed monopole antenna, which could be utilized for PD detection. The original antenna structure is taken from the disk-cone (DISCONE) antenna, known for its broad bandwidth properties [81]. The structural symmetry of planar antennas can reduce the size by 50% [108]. This technique has been applied to the proposed sensor. Nonetheless, a considerable degradation of the antenna performance was observed. Thus, the feedline of the antenna was modified to improve the bandwidth of the antenna. In fact, by reducing the antenna size, the directivity has been improved, as depicted by the H-plane radiation pattern. Although CPW-fed annular monopole antennas have been used in wireless communication applications, they were not utilized in PD applications, to the best of the authors' knowledge. The novelty of this work can be summarized as follows:

- Optimizing CPW-fed annular monopole antennas to utilize it for PD detection application.
- Utilizing the structural symmetry and improving the feedline width to improve the antenna's performance compared with the conventional size reduction.

5.2 Proposed Antenna Overview

The original antenna structure is taken from the DISCONE antenna [81]. The proposed sensor's first design was implemented and tested in 2007, exhibiting an ultra-bandwidth with a higher than

21:1 ratio [109]. In this work, the first step was optimizing the sensor to cover the UHF frequency range. The optimized antenna exhibits a large bandwidth extending from 0.53GHz exceeding 3GHz. Nonetheless, to ensure that the antenna operates at low frequencies, the optimized antenna size is 245mm $\times$ 300mm.

Due to the antenna's structural symmetry, a size-reduction technique has been utilized to reduce its size by 50% [108]. Nonetheless, this size reduction dramatically degrades the antenna's performance due to the reduced feed point width, increasing the observed input impedance. Thus, the new antenna size was slightly increased to ensure that the feed point width is maintained as in the original design. Figure 5.1 shows the development of the antenna implementation steps.

Although the modified antenna does not exhibit the same bandwidth as the original design, the radiation pattern has been improved for PD applications since the new design has a maximum gain in a single direction, whereas the original antenna gain is bi-directional.

5.3 Finite Element Model

3D Maxwell solver of COMSOL Multi-physics is used to implement the antenna designs. The frequency-domain interface of the RF module has been utilized to test the antenna's performance. The following equations are evaluated:

$$\nabla \times \frac{1}{\mu_r} (\nabla \times \mathbf{E}) - k_0 \left(\epsilon_r - \frac{j\sigma}{\omega \epsilon_0} \right) \mathbf{E} = 0, \tag{5.1}$$

$$Z_{port} = \frac{V_{\text{port}}}{I_{\text{port}}}, \tag{5.2}$$

$$\mathbf{n} \times \mathbf{E} = 0, \tag{5.3}$$

where $\mathbf{E}$ represents the electric field, k_0 represents the free space wavenumber, ϵ_r is the relative permittivity, ϵ_0 is the free space permittivity, μ_r is the relative permeability, and σ is the electrical conductivity. Equation (1) is used to solve for the time-harmonic electric field. On the other hand,

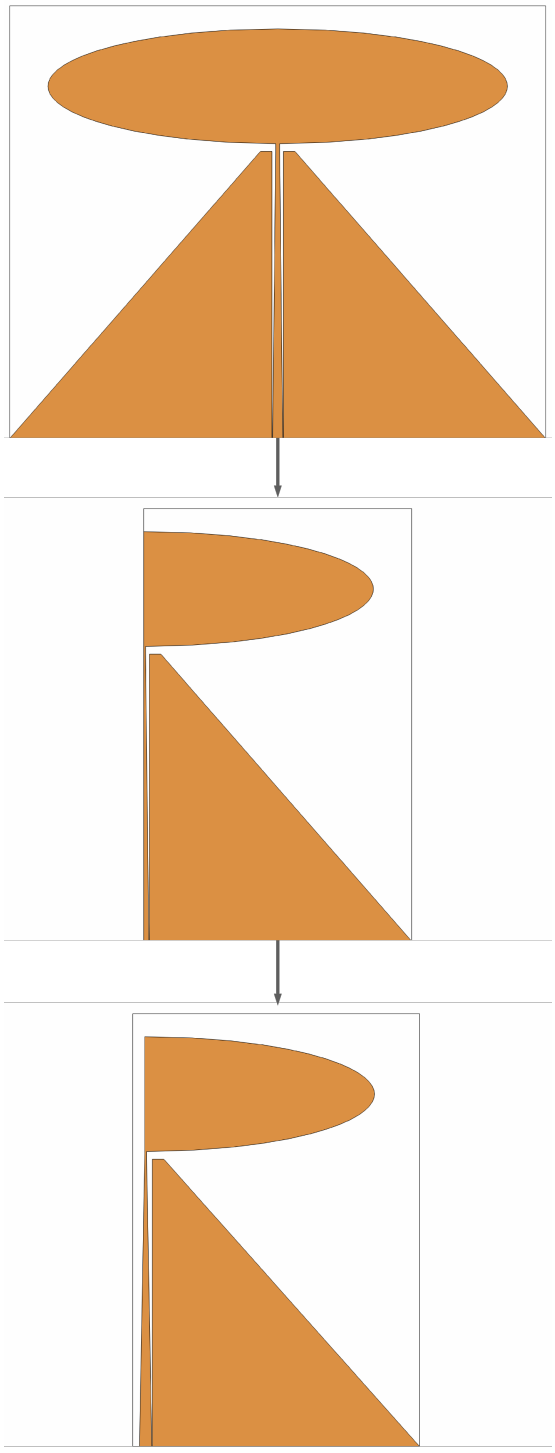

Figure 5.1: UHF antenna development. The original antenna size is 245mm $\times$ 300mm, whereas the modified size is reduced to 245mm $\times$ 160mm.

(2) is used to obtain the port impedance and the reflection coefficient (S11) (using the electric and magnetic fields), whereas (3) sets the tangential electric field to zero (i.e., perfect electric conductor (PEC)). PEC has been used to model all metallic parts in the model. "Uniform lumped port" is used to represent the port of excitation. The model has been excited with a 50 Ω impedance.

The antenna is built in a Rogers RO4003C substrate, whereas air has been used to model the surrounding domain. Moreover, a perfectly matched layer (PML) was used at the domain's outer surrounding area. Setting the maximum frequency to 3GHz, the wavelength for both air and the substrate was obtained to assign the mesh. Six elements per wavelength was used to ensure the accuracy of the obtained results. Table 5.1 summarizes the computational properties for the three antenna designs. All simulations were performed using Intel(R), Xeon(R), Gold 6138CPU @ 2GHz (40CPUs), 192GB RAM workstation. The simulation covers frequencies between 0.3GHz and 3GHz with a 0.01GHz frequency-step. Hence, a total of 271 points has been utilized for each simulation scenario. It is perceived by Table 5.1 that the computational time has experienced a significant improvement as the system's size is reduced. Figure 5.2 shows the geometry of the original design and the assigned dimensions. The remaining two designs are not given since they can be easily built based on the same given parameters.

5.4 Antenna Performance Results

5.4.1 Original Design

The original antenna exhibits the best performance when it comes to bandwidth. Figure 5.3 shows the reflection coefficient of the antenna. As depicted from Figure 5.3, the antenna covers frequencies between 0.53GHz-3GHz with a less than -10dB reflection coefficient, verifying the wide bandwidth of such antennas. Such wideband behavior is expected since the antenna's tapered ground helps maintain an oscillating input impedance around the 50Ω impedance over a wide frequency range [35]. Moreover, the antenna's H-plane radiation pattern at three different frequencies is shown in Figure 5.4. The antenna radiation pattern is symmetric about the y-axis contributing to two maxima at every single frequency point due to the antenna's structural symmetry. This can

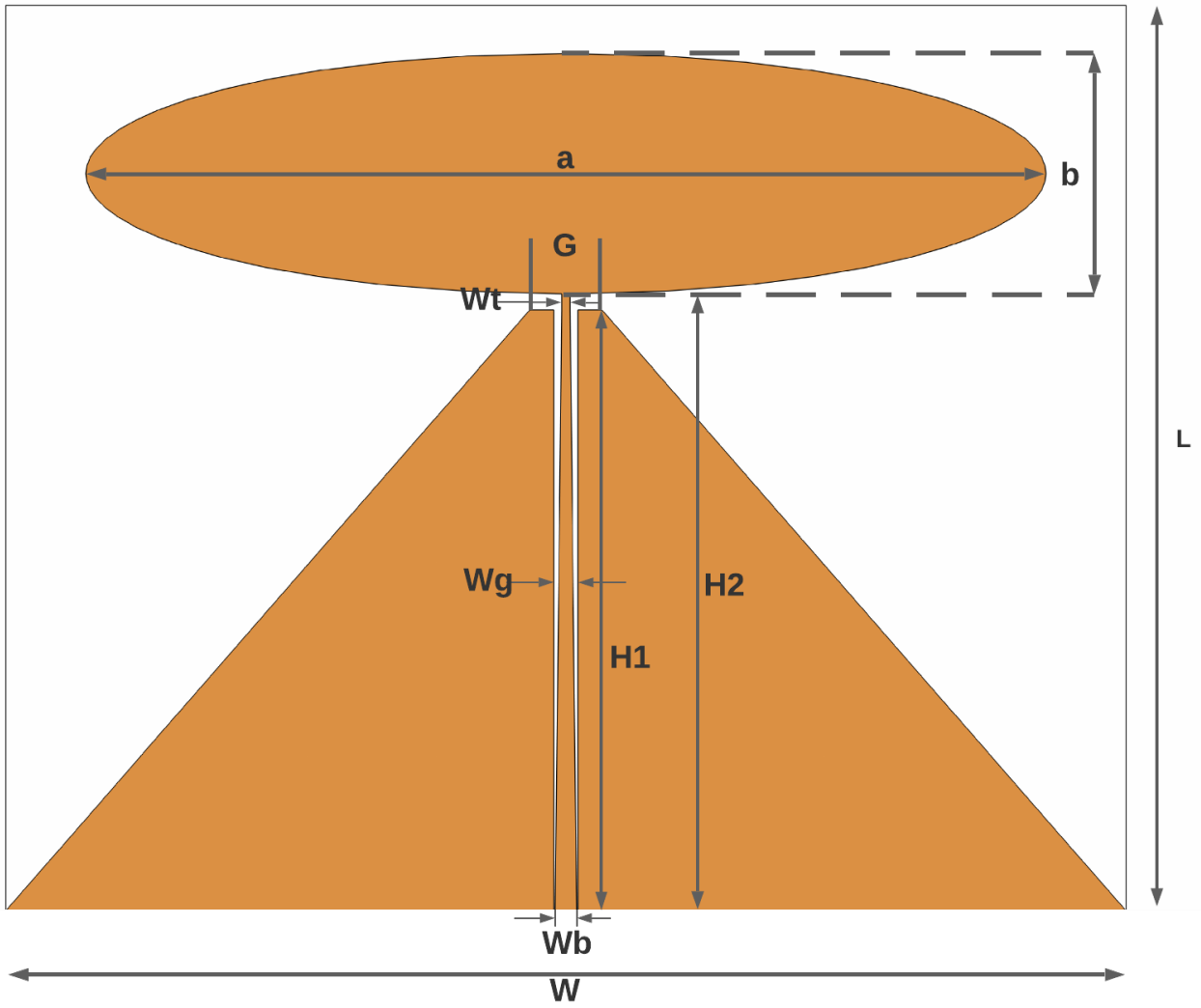

Figure 5.2: Geometry of the UHF sensor. $W = 300mm$, $L = 245mm$, $a = 257.2mm$, $b = 64.3mm$, $H1 = 160.8mm$, $H2 = 165.8mm$, $Wg = 6.42mm$, $Wt = 5.8mm$, $Wb = 2.15mm$, and $G = 19.3mm$.

increase the noise captured by the antenna from the environment.

5.4.2 Size-Reduced Antenna

The size of the antenna can be reduced by 50% when structural symmetry is utilized. Such size reduction does not affect the antenna's resonance frequencies if chopped along the magnetic wall axis. Figure 5.5 shows the current distribution before and after applying the size-reduction technique at 1GHz.

Table 5.1: Computational properties of the three simulated antennas

Antenna	Computational Time	Number of Elements
Original Antenna	10 Hours, 8 Minutes, and 43 Seconds	• 559940 Domain Elements • 53977 Boundary Elements • 2001 Edge Elements
Size-Reduced Antenna	4 Hours, 35 Minutes, and 28 Seconds	• 298318 Domain Elements • 29856 Boundary Elements • 1373 Edge Elements
Modified Feed Point Antenna	5 Hours, 0 Minutes, and 51 seconds	• 307794 Domain Elements • 31065 Boundary Elements • 1441 Edge Elements

Although applying the size-reduction technique on the antenna does not significantly affect the current distribution, the reflection coefficient experienced a major degradation, as depicted from Figure 5.6. The antenna, in this case, is operating properly over limited frequency ranges. This is attributed to the reduction of the feed point width when applying such dimensionality reduction. Thus, the antenna size has been slightly increased to allow the feed point width to be conserved.

Figure 5.6 shows the modified antenna performance as compared with the size-reduced antenna. A considerable improvement in the reflection coefficient is observed. The bandwidth of the antenna is still not as wide as that of the original design. Nevertheless, the reflection coefficient of the sensor is covering most of the UHF frequency range with few notches. In fact, if the -8dB limit is considered instead of the -10dB, the antenna would have a notch centered at 0.6GHz and it would cover frequencies below 2.75GHz.

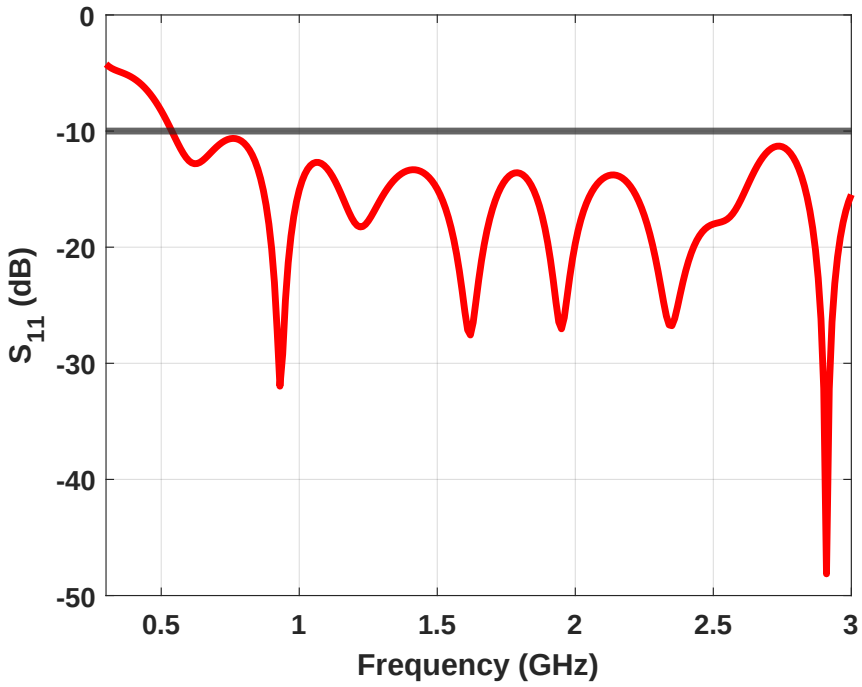

Figure 5.3: Reflection coefficient of the original antenna design.

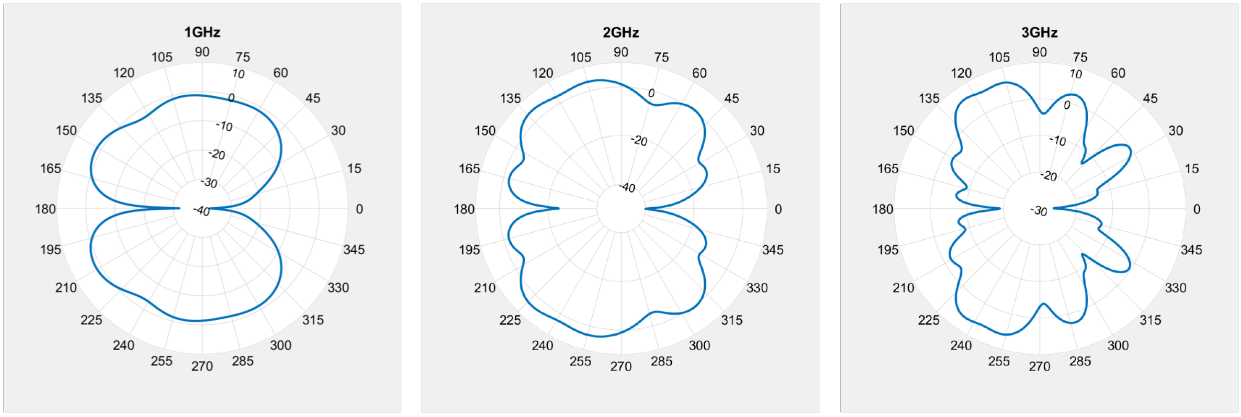

Figure 5.4: H-plane radiation pattern of the original antenna design.

Figure 5.7, on the other hand, shows the H-plane radiation pattern (simulated) of the modified antenna. It can be seen that the antenna radiation pattern has a maximum in a single direction in this case. This behavior reduces the captured noise from the environment when utilizing the UHF sensor in PD applications.

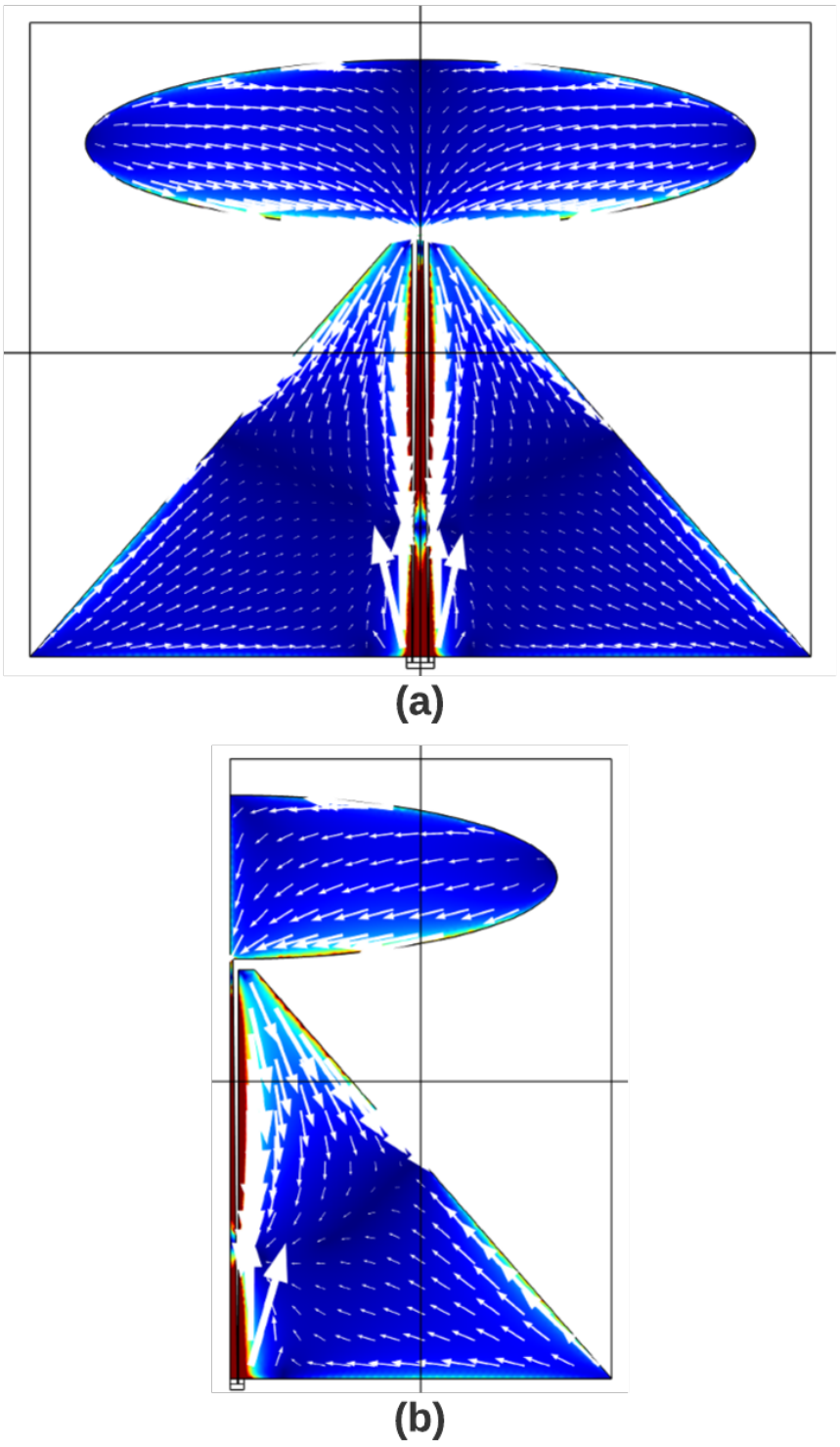

Figure 5.5: Surface current distribution a) before and b) after applying the size-reduction.

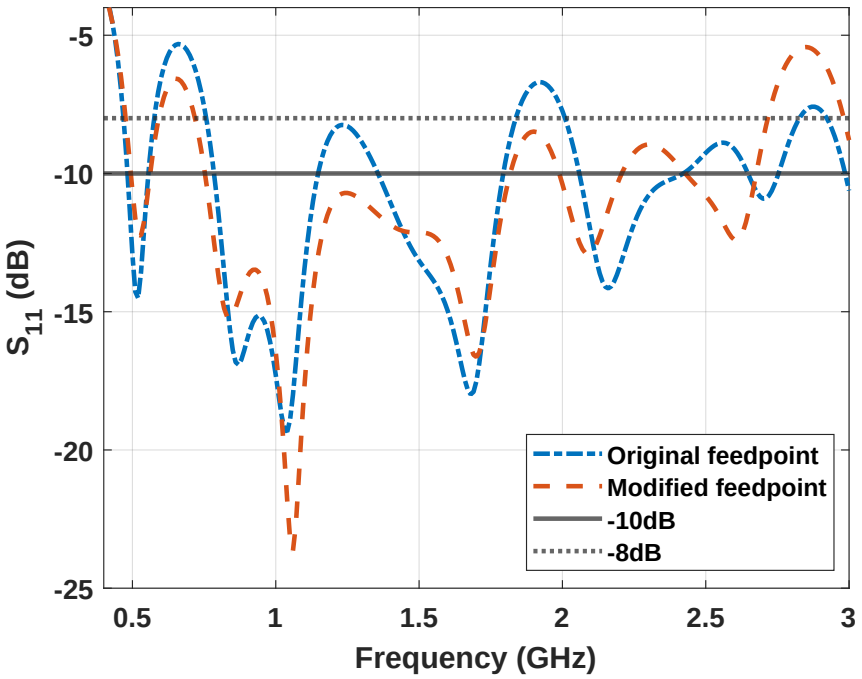

Figure 5.6: Impact of size reduction on the sensor's reflection coefficient.

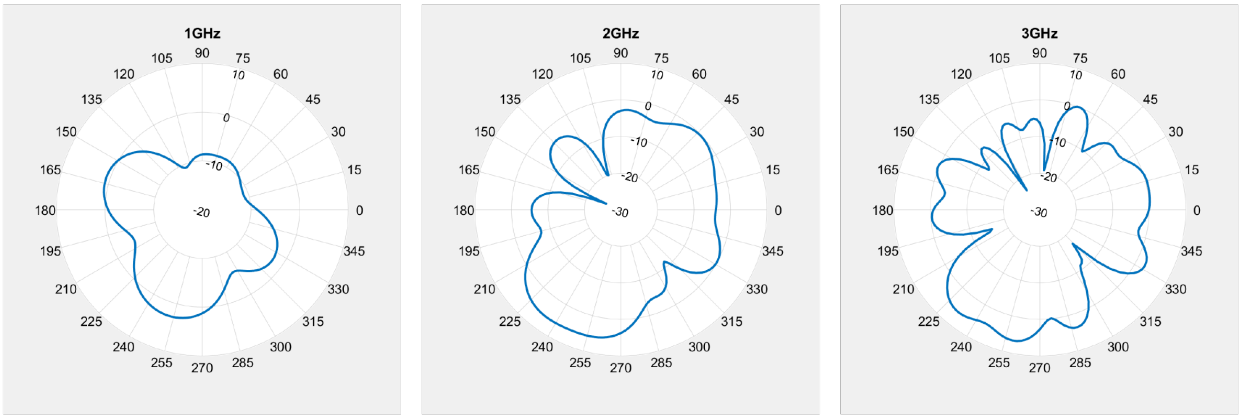

Figure 5.7: H-plane radiation pattern of the modifed antenna design.

5.4.3 Experimental Validation

Figure 5.8 shows the measured and simulated reflection coefficient of the proposed sensor. The sensor operates over frequencies ranging between 0.5GHz-3GHz, with notches centered at three frequencies as shown by the figure (0.6GHz, 1.2GHz, and 2.75GHz), considering the -10dB limit.

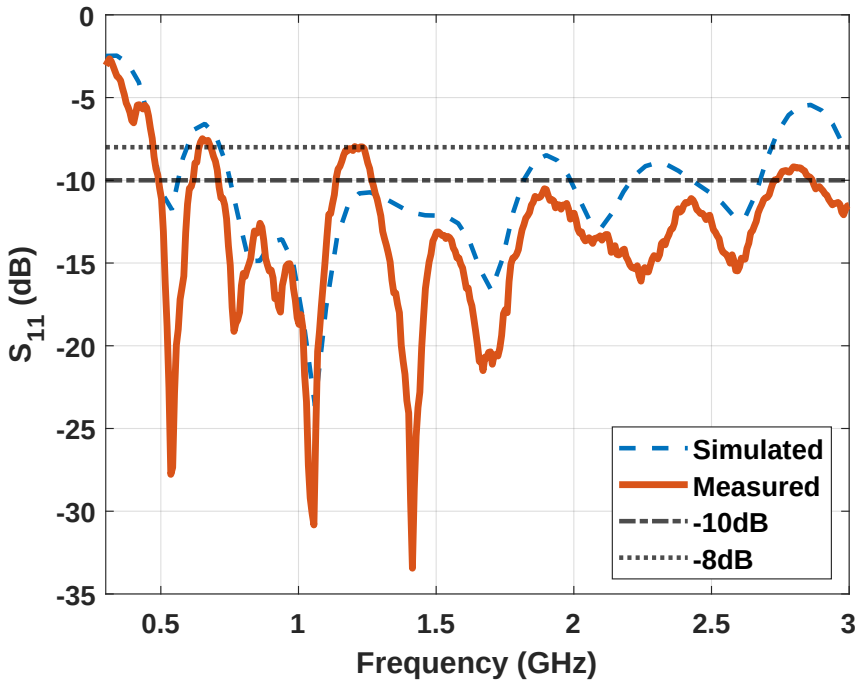

Figure 5.8: Measured and simulated reflection coefficient of the proposed sensor.

The anechoic chamber is used to obtain the proposed sensor's gain and radiation pattern, as shown in Figure 5.9. The gain of the antenna is plotted and shown in Figure 5.10. The gain increases with frequency, reaching a maximum gain of 6.25dBi at 2.75GHz. The antenna exhibits a relatively high gain as compared with other existing antennas.

On the other hand, Figure 5.11 shows the E-plane and H-plane radiation patterns of the proposed antenna. The E-plane radiation pattern shows that the antenna acts as a dipole antenna at low frequencies. At higher frequencies, the pattern has significantly deviated from the dipole behavior. This could be attributed to the impact of the feedline connecting the main radiating structure to the port of excitation. The wavelength would be large enough that the propagating waves do not see the feed point at low frequencies. At higher frequencies, the feed point could have an enormous impact on the propagating EM waves. Hence, a significant deviation from the dipole radiation pattern could be seen.

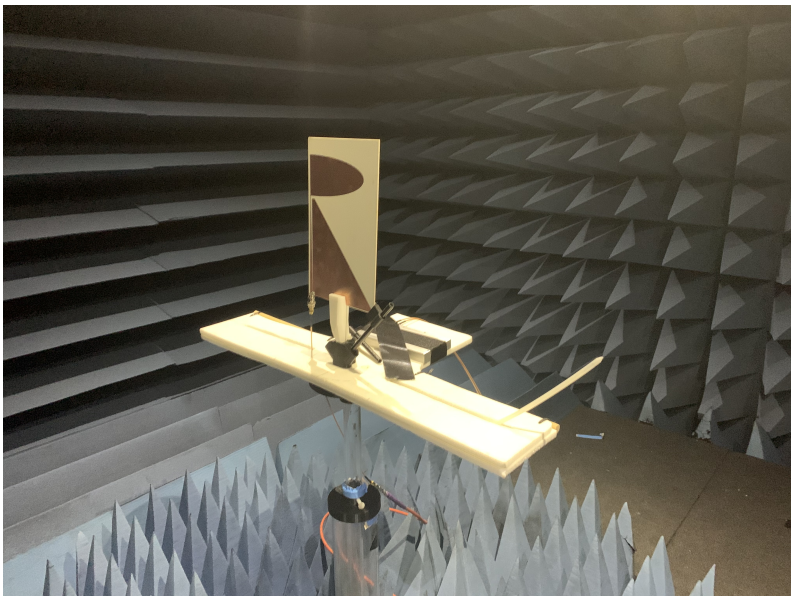

Figure 5.9: Modified UHF sensor setup in anechoic chamber. This setup is used to obtain the radiation pattern and gain.

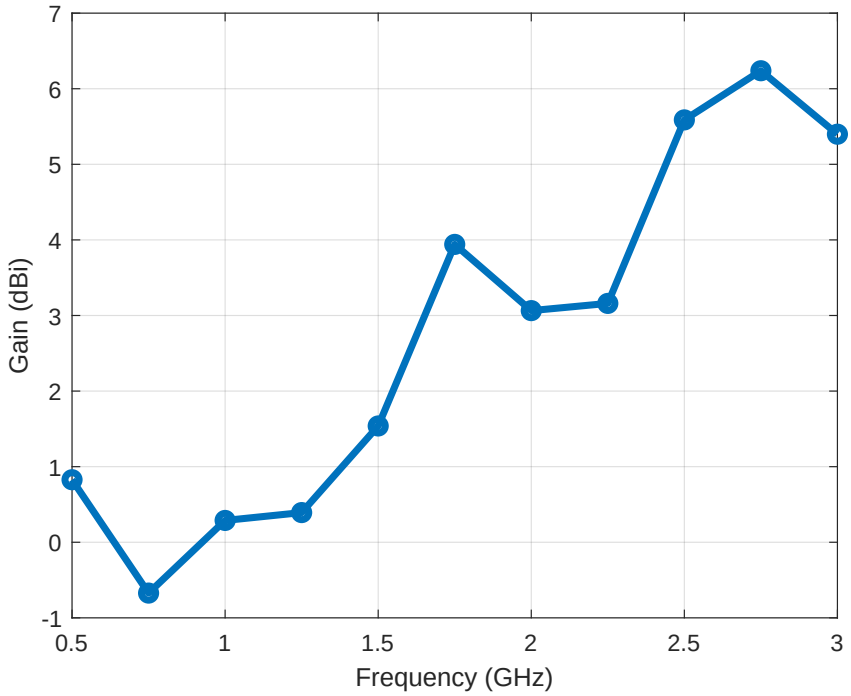

Figure 5.10: Measured gain of the modified UHF sensor.

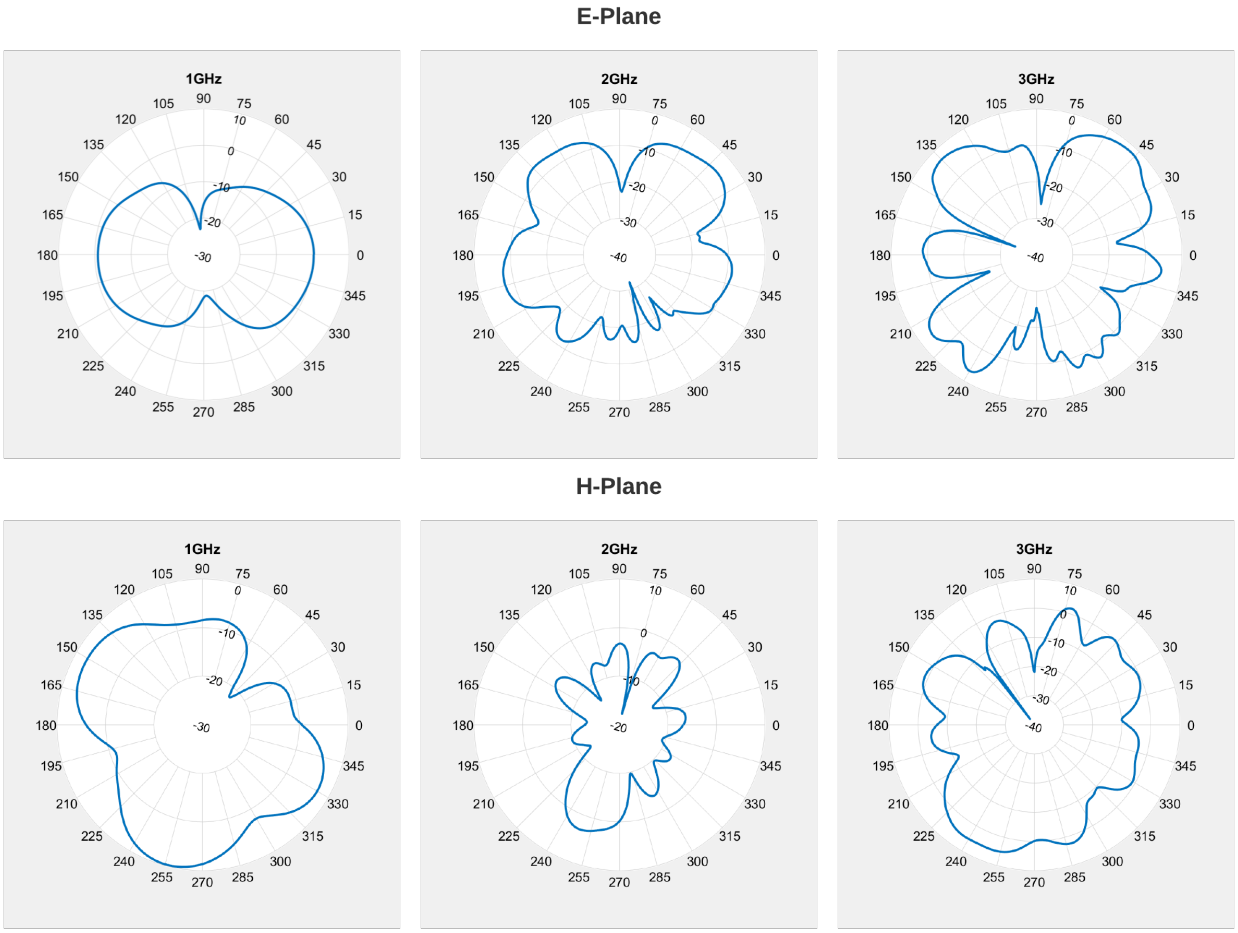

Figure 5.11: Measured E-Plane and H-plane radiation pattern of the implemented antenna.

5.5 PD Detection using the Proposed Antenna

5.5.1 PD setup and measurement using the proposed antenna

A PD test setup has been utilized to verify the effectiveness of the proposed sensor in PD detection. A sharp point to ground arrangement has been used to generate PD as depicted in Figure 5.12. The antenna has been placed so that the maximum gain direction is set towards the PD source. After that, a 150kV test transformer has been used to raise the voltage gradually to generate the PD pulses between the sharp electrode and the grounded electrode. The antenna is connected to a 2GHz oscilloscope to detect the time-domain radiated PD signals. It is worth mentioning that only at around 15kV a hissing sound, as an indication of corona, was noticeable

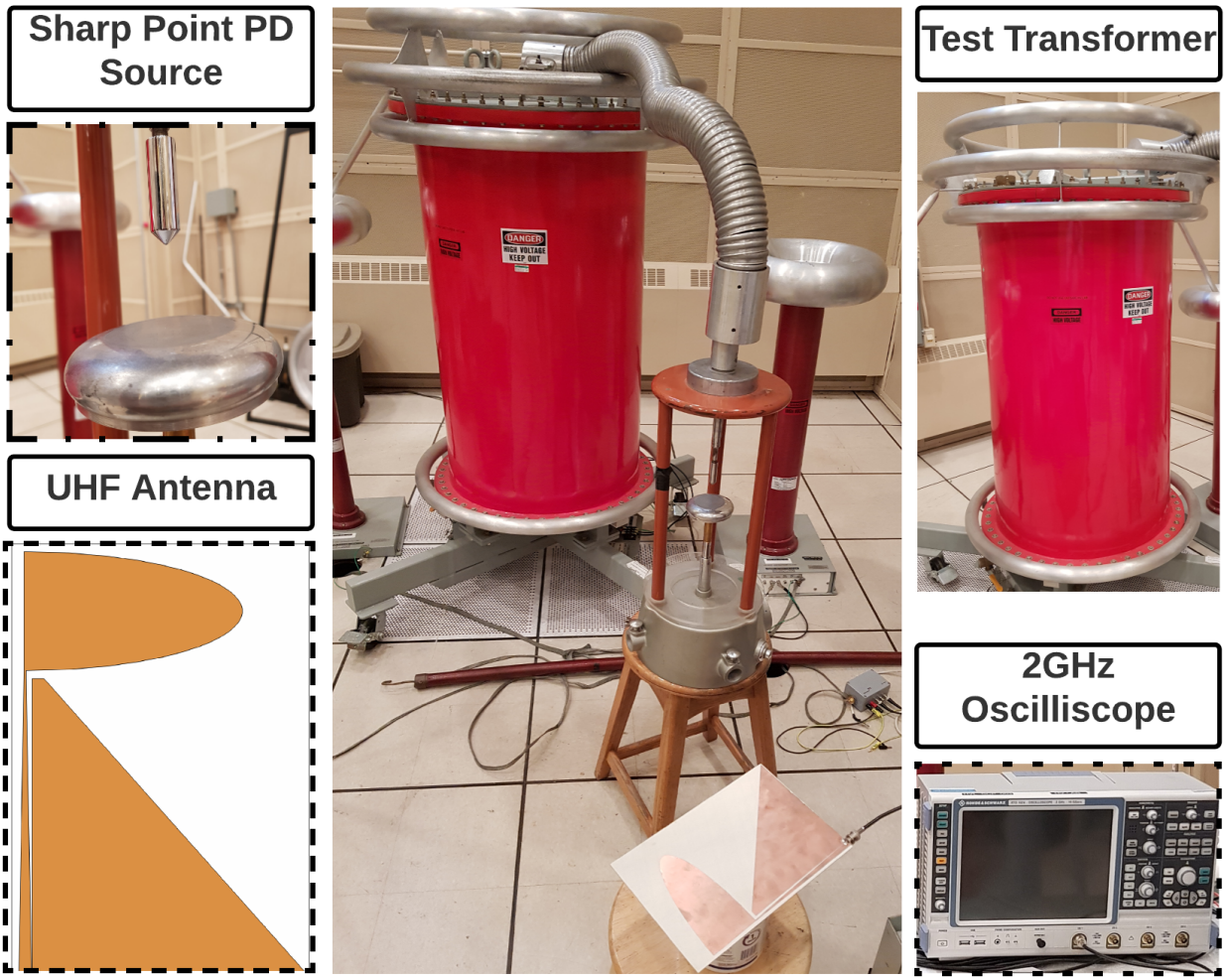

Figure 5.12: UHF sensor testing setup. Corona discharge is used by applying high potential difference between a sharp electrode, and a ground.

from the PD source. The antenna exhibits a good sensitivity by capturing PD signals when the voltage is raised to only 6kV.

Figure 5.13 shows the captured PD signals by the proposed UHF sensor when the applied voltage is set to 6kV (Figure 5.13(a)) and 15kV (Figure 5.13(b)).

5.5.2 Comparison with Other Existing Antennas

To explore the advantages and limitations of the proposed antenna. A comparative analysis between the proposed sensor and other commonly used sensors in PD applications is carried out and presented in Table 5.2 below. Based on the color coding used in this analysis, the proposed

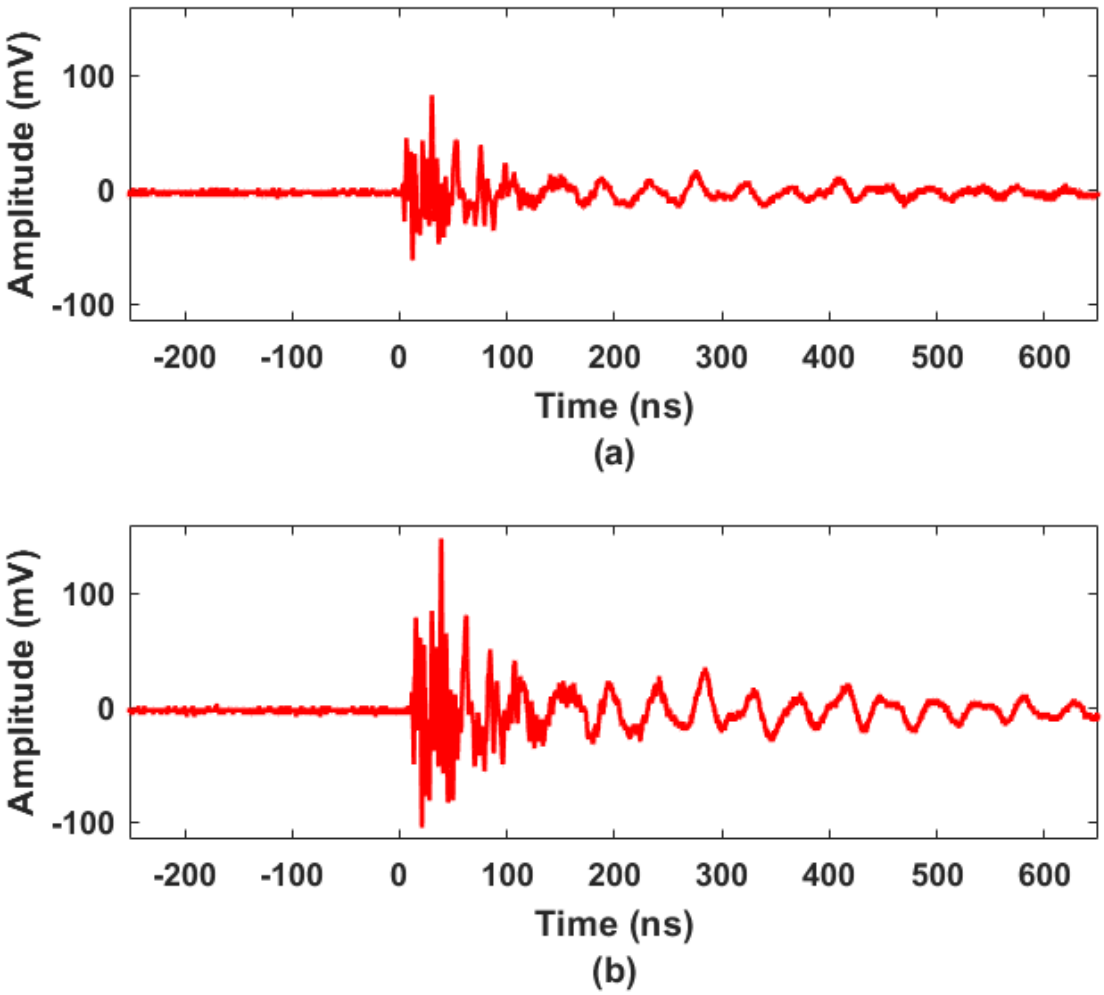

Figure 5.13: Captured time-domain signals by the UHF sensor due to corona discharge when a voltage of a) 6kV, b) 15kV is applied.

antenna outperforms most other sensors. The Spiral antenna is the only antenna that can potentially outperform the proposed UHF sensor (depending on the application).

By inspecting the different performance metrics separately, it can be seen from the obtained results that the proposed UHF sensor covers most of the UHF frequency range. Log-periodic and horn antennas have better bandwidth and gain but at the expense of size and cost. Hence, since the proposed sensor covers most of the UHF frequency and has a relatively moderate gain, it outperforms the two antennas mentioned above, especially since building such a sensor is cheaper.

Table 5.2: A Comparison between Different Types of Antennas Used for PD Applications

Antenna	Horn	Log Periodic	Loop	Dipole	Spiral	Micro strip	This Work
Bandwidth	Very Large	Very Large	Narrow	Narrow	Large	Narrow	Large
Gain	Very High	High	Small	Small	Moderate	Moderate	Moderate
Size	Very Large	Very Large	Very Small	Very Small	Moderate	Moderate	Moderate
Cost	Very High	Very High	Low	Low	Low	Low	Low
Polarization	Linear	Linear	Linear	Linear	Circular	Linear	Linear

Performance: Good Average Poor

On the other hand, dipole, loop, and microstrip antennas are usually limited in bandwidth and gain. Finally, the spiral antenna has a comparable overall performance to the proposed sensor, but it is circularly polarized. Thus, if the PD application requires a linearly polarized antenna, the proposed sensor is a better fit compared with the spiral counterpart. Such applications might include the external detection of PD in GIS and transformers [40].

5.6 Conclusion

In this work, a CPW-fed annular monopole antenna has been utilized for PD detection. A size reduction technique that utilizes the structural symmetry of the antenna has been applied. The following concluding remarks are drawn:

- CPW-Fed annular monopole antennas can be utilized in PD detection, given their large bandwidth.

- Planar antenna structural symmetry can reduce the antenna size by about 50
- Reducing the antenna size can improve such UHF sensors' PD detection capabilities (directivity).
- The proposed UHF sensor exhibits high sensitivity in detecting PD activities.
- The following specifications are obtained for the antenna:
    1. Antenna dimensions are (L$\times$W$\times$H) 245mm $\times$ 160mm $\times$ 1.524mm.
    2. Antenna bandwidth is 0.5GHz-3GHz with notches centered at 0.6GHz, 1.2GHz, and 2.75GHz.
    3. The proposed sensor gain reaches its peak value of 6.25dBi at 2.75GHz.

6. SUMMARY AND CONCLUSIONS

6.1 Concluding Remarks

This dissertation addresses the development of ultra-high frequency techniques in partial discharge detection, localization, and classification. Finite element analysis has been utilized to implement different gas-insulated switchgear models using the 3D Maxwell solver of COMSOL Multiphysics. This work proposes new modeling approaches for GIS systems based on the CIGRE sensitivity verification recommendations to understand the propagation behavior of electromagnetic waves within such capital assets. Hence, the implemented FE models can improve the utilization of UHF sensing techniques inside GIS systems. A new class of UHF antennas has also been proposed to detect PD activities within the insulation material of high voltage apparatuses.

In Chapter II, an extensive literature review on the propagation of electromagnetic waves within GIS systems has been presented. Different PD modeling approaches have been discussed. The three-capacitor model and the dipole model comprise the most common modeling approaches. The three-capacitor model suffers from the lack of geometries that such an approach can represent. On the other hand, the dipole or induced charge model accurately represents PD for many different geometries. The dipole model requires complicated field modeling and finding solutions to such models can be cumbersome.

The impact of different barriers in GIS has also been presented and discussed in Chapter II. Most existing works consider a single discontinuity within the GIS at a time. Such barriers include L bends, T bends, dielectric spacers, the relative angle between PD source and sensors, and disconnecting switches. FDTD has been predominantly used to model simplified GIS systems and discuss the impact of the barriers mentioned above. The implemented FDTD GIS models utilized the simplified dipole model to represent PD activities within the GIS. Such PD modeling does not take into consideration the treeing effect experienced by PD current pulsations. Hence, a significant discrepancy between measurements and simulations has been perceived. Finally, it

has also been concluded that the internal sensors used for PD in GIS have better sensitivity and better immunity against noise than their external counterparts. Nevertheless, reintegrating internal sensors in old GIS devices can be very costly. Thus, external detection is still used nowadays for PD monitoring in GIS devices.

Chapter III proposes the first GIS model built using the FEA tool. A 252kV L structure GIS model has been implemented using COMSOL multi-physics. To overcome the limitations of utilizing the simplified dipole model, CSVR has been used as the primary modeling approach. Analytical and experimental results from the literature have been initially utilized to verify the modeling accuracy. Then, four different simulation scenarios have been simulated. In the first scenario, the impact of disconnecting switches and L bends is considered. Multiple reflections due to the L bend are perceived, especially the TE11 mode of propagation. On the other hand, the dielectric spacers cause reflections to the higher-order mode frequencies. In the second and third simulation scenarios, the impact of a disconnecting switch is added to the model. Low-frequency (TEM) components experienced significant attenuation and reflection due to the switch. On the other hand, a minute attenuation has been perceived by the higher-order mode components. Finally, the last simulation scenario studies the impact of distance between PD source and sensors on the attenuation of EM waves. It has been shown that the TEM mode of propagation experience a small attenuation as a function of distance, whereas higher-order modes rapidly attenuate with distance.

In chapter IV, an extended-T (π) GIS system has been modeled. The utilized 550kV GIS has multiple barriers, including sudden changes in inner and outer diameters, disconnecting switches, bends, and dielectric spacers. In other words, the full complexity of a GIS has been considered in the model. Experimental results were used to verify the accuracy of the obtained simulated results, and considerable agreement has been perceived. This work is a first trial to model a GIS to the full complexity while simultaneously utilizing CSVR and externally connected sensors. The obtained results show that many resonances are created within the GIS enclosure. It has also been shown that a significant attenuation to the propagating EM waves is caused by the π bend, dielectric spacers, and disconnecting switches. In addition, time-domain results show that the TEM mode

of propagation experiences a significant reflection if disconnecting switches are opened. Higher-order modes are capable of propagating even in the existence of open disconnecting switches. This is because TEM mode cannot propagate inside circular waveguides, whereas higher-order modes can freely propagate.

In chapter V, a new class of UHF antennas to detect PD discharges has been proposed and tested. A CPW-fed annular monopole antenna has been initially implemented in COMSOL, and the antenna was optimized to cover the UHF range. The reflection coefficient of the optimized antenna showed an acceptable performance over frequencies ranging from 0.5GHz to 2.95GHz. The H-plane radiation pattern of the antenna showed that the antenna has two maxima over the frequency of operation. The size was reduced to 50% utilizing the structural symmetry of the antenna since current resonances were not affected. However, due to the reduction of the port of excitation width, the antenna performance degraded. The size of the antenna was slightly increased to ensure that the port of excitation width is not affected and reduce the performance degradation. The proposed sensor has been implemented, and the results show that it covers frequencies ranging between 0.5GHz and 3GHz with few notches centered at 0.6GHz, 1.2GHz, and 2.8GHz. The H-plane radiation pattern showed that the antenna has a maximum in a single direction, reducing the noise captured from the environment. Finally, the measured gain showed that the antenna has a steady increase in gain (with frequency), reaching a maximum gain of 6.25dBi at 2.75GHz.

6.2 Recommendations for Future Work

In this work, the main focus was on analyzing the propagation of EM waves within GIS systems. Similar analyses could also be applied in other high voltage devices including transformers, and electric machines. Transformers comprise a highly complex structure to the EM waves since a transformer tank is a metallic cage filled with multiple metallic and nonmetallic barriers. A minimal effort has been made thus far to analyze the EM waves within transformers, and hence, UHF detection within such devices is considered a hot topic to be tackled. On the other hand, electric machines are fully encapsulated devices with small openings at different places. Thus, employing UHF detection in electric machines can be potentially improved by understanding the propagation

of EM waves within electric machines.

Proposing new UHF sensors for PD detection is of paramount significance since many different antenna classes exist, and a minimal number of antennas are used in PD detection. In this work, a linearly polarized class of antennas has been proposed. Circularly polarized antennas are also essential in the internal detection of PD activities with GIS and transformers. Hence, proposing small, cheap, wideband, and easily fabricated class(es) of UHF sensors is very significant to improve the utilization of UHF sensors in PD detection.

This work focuses on improving the utilization of UHF detection techniques for PD detection. Although most existing techniques have been mainly investigated and analyzed, combining multiple techniques can improve PD detection in the different high voltage systems. To illustrate, Combining UHF and optical detection techniques can improve the detection sensitivity in GIS systems. Optical detection can detect the photons radiated during the electron attachment regardless of the current magnitude; hence, low-magnitude discharges can be detected. On the other hand, Optical detection might not correctly detect PD activities when the applied voltage is very high. At high applied voltage, the streamer discharge occurs, and UHF detection is very effective under such conditions. Other combinations might include acoustics with the UHF and acoustics with the optical detection techniques.

Machine learning has recently been extensively used to classify and localize different classes of PD defects. Nonetheless, the utilized machine learning algorithms in PD applications are very limited, even though many machine learning techniques are being proposed daily. Hence, there are potentially multiple techniques that might outperform most, if not all, utilized techniques for PD classification.

REFERENCES

[1] Q. Khan, S. Refaat, H. Abu-Rub, H. Toliyat, and A. Darwish, "Characterization of defects inside the cable dielectric with partial discharge modeling," *IEEE Transactions on Instrumentation and Measurement*, vol. 70, pp. 1–11, 2020.

[2] H. H. Sinaga, *Detection Identification and Localization of Partial Discharges in Power Transformers Using UHF Techniques*. PhD thesis, 2012.

[3] D. Dai, X. Wang, J. Long, M. Tian, G. Zhu, and J. Zhang, "Feature extraction of gis partial discharge signal based on s-transform and singular value decomposition," *IET Science, Measurement & Technology*, vol. 11, no. 2, pp. 186–193, 2017.

[4] M. D. Judd, Li Yang, and I. B. B. Hunter, "Partial discharge monitoring of power transformers using uhf sensors. part i: sensors and signal interpretation," *IEEE Electrical Insulation Magazine*, vol. 21, no. 2, pp. 5–14, 2005.

[5] M.-X. Zhu, Q. Liu, Y.-B. Wang, Y. Li, J.-B. Deng, H.-B. Mu, and G.-J. Zhang, "Optimisation of antenna array allocation for partial discharge localisation in air-insulated substation," *IET Science, Measurement & Technology*, vol. 11, no. 8, pp. 967–975, 2005.

[6] S. Masuda, T. Koga, M. Kozako, M. Hikita, H. Haruyama, I. Kato, H. Sato, and F. Aono, "Basic study on measurement of electromagnetic waves emitted by partial discharge in cable joint for high voltage overhead transmission," in *2017 International Symposium on Electrical Insulating Materials (ISEIM)*, vol. 2, pp. 547–550, 2017.

[7] G. Stone, E. Boulter, I. Culbert, and H. Dhirani, *Electrical insulation for rotating machines: design, evaluation, aging, testing, and repair*. Wiley-IEEE Press, 2004.

[8] S. Meijer, *Partial Discharge Diagnosis of High-Voltage Gas-Insulated Systems*. PhD thesis, 2001.

[9] X. Fan, L. Li, Y. Zhou, N. Tang, Z. Zou, X. Li, G. Huang, and M. Liu, "Online detection technology for sf6 decomposition products in electrical equipment: a review," *IET Science, Measurement & Technology*, vol. 12, no. 6, pp. 707–711, 2018.

[10] H. Guo, F. Fusheng Lü, and K. F. Ren, "Simulation and measurement of pd-induced electromagnetic wave leakage in gis with metal belt," *IEEE Transactions on Dielectrics and Electrical Insulation*, vol. 21, no. 4, pp. 1942–1949, 2014.

[11] X. Li, X. Wang, A. Yang, D. Xie, D. Ding, and M. Rong, "Propogation characteristics of pd-induced uhf signal in 126 kv gis with three-phase construction based on time–frequency analysis," *IET Science, Measurement & Technology*, vol. 10, no. 7, pp. 805–812, 2016.

[12] M. Hikita, S. Ohtsuka, G. Ueta, S. Okabe, T. Hoshino, and S. Maruyama, "Influence of insulating spacer type on propagation properties of pd-induced electromagnetic wave in gis," *IEEE Transactions on Dielectrics and Electrical Insulation*, vol. 17, no. 5, pp. 1642–1648, 2010.

[13] A. Sabot, A. Petit, and J. P. Taillebois, "Gis insulation co-ordination: on-site tests and dielectric diagnostic techniques. a utility point of view," *IEEE Transactions on Power Delivery*, vol. 11, no. 3, pp. 1309–1316, 1996.

[14] S. S. Refaat and M. A. Shams, "A review of partial discharge detection, diagnosis techniques in high voltage power cables," in *2018 IEEE 12th International Conference on Compatibility, Power Electronics and Power Engineering (CPE-POWERENG 2018)*, pp. 1–5, 2018.

[15] W. Gao, D. Ding, W. Liu, and X. Huang, "Analysis of the intrinsic characteristics of the partial discharge induced by typical defects in gis," *IEEE Transactions on Dielectrics and Electrical Insulation*, vol. 20, no. 3, pp. 782–790, 2013.

[16] R. Bartnikas, "Partial discharges. their mechanism, detection and measurement," *IEEE Transactions on Dielectrics and Electrical Insulation*, vol. 9, no. 5, pp. 763–808, 2002.

[17] e. a. M. M. Yacob, "Review on partial discharge detection techniques related to high voltage power equipment using different sensors," *Photonic Sens*, vol. 4, pp. 325–337, 2014.

[18] B. Qi, C. Li, Z. Hao, B. Geng, D. Xu, S. Liu, and C. Deng, "Partial discharge detection for gis: A comparison between uhf and acoustic methods," in *2010 IEEE International Symposium on Electrical Insulation*, pp. 1–5, 2010.

[19] M. Ren, J. Zhou, S. Yang, T. Zhuang, M. Dong, and R. Albarracín, "Optical partial discharge diagnosis in sf6 gas-insulated system with sipm-based sensor array," *IEEE Sensors Journal*, vol. 18, no. 13, pp. 5532–5540, 2018.

[20] F. Álvarez, F. Garnacho, J. Ortego, and M. Sánchez-Urán, "Application of hfct and uhf sensors in on-line partial discharge measurements for insulation diagnosis of high voltage equipment," *Sensors*, vol. 15, no. 4, pp. 7360–7387, 2015.

[21] E. Jennings and A. Collinson, "A partial discharge monitor for the measurement of partial discharges in a high voltage plant by the transient earth voltage technique," in *1993 International Conference on Partial Discharge*, pp. 90–91, 1993.

[22] G. Behrmann and J. Smajic, "Rf pd signal propagation in gis: Comparing s-parameter measurements with an rf transmission model for a short section of gis," *IEEE Transactions on Dielectrics and Electrical Insulation*, vol. 23, no. 3, pp. 1331–1337, 2016.

[23] M. Wu, H. Cao, J. Cao, H. Nguyen, J. B. Gomes, and S. P. Krishnaswamy, "An overview of state-of-the-art partial discharge analysis techniques for condition monitoring," *IEEE Electrical Insulation Magazine*, vol. 31, no. 6, pp. 22–35, 2015.

[24] Solanki, "Breakdown in gases," 2017.

[25] S. Korneliussen, "Partial discharges and breakdown voltage in designs with triple junctions under ac stress," Master's thesis, 2016.

[26] M. Abdel-salam, H. Anis, A. El-Morshedy, and R. Radwan, *High Voltage Engineering: Theory and Practice*. Marcel Dekker, Inc., 2^{nd} ed., 2000.

[27] Almatri, "Streamer theory," 2015.

[28] A. Pedersen, T. Christen, A. Blaszczyk, and H. Boehme, "Streamer inception and propagation models for designing air insulated power devices," in *2009 IEEE Conference on Electrical Insulation and Dielectric Phenomena*, pp. 604–607, 2009.

[29] X. Li, X. Wang, A. Yang, D. Xie, D. Ding, and M. Rong, "Propogation characteristics of pd-induced uhf signal in 126 kv gis with three-phase construction based on time–frequency analysis," *IET Science, Measurement & Technology*, vol. 10, no. 7, pp. 805–812, 2016.

[30] J. Dengwei, T. Cheng, and G. Wensheng, "Frequency spectrum properties and propagation features of typical pd in the gis," 2016.

[31] M. D. Judd and O. Farish, "High bandwidth measurement of partial discharge current pulses," in *Conference Record of the 1998 IEEE International Symposium on Electrical Insulation (Cat. No.98CH36239)*, vol. 2, pp. 436–439 vol.2, 1998.

[32] A. Reid and M. Judd, "High bandwidth measurement of partial discharge pulses in sf6," in *14th International Symposium on High Voltage Engineering*, vol. 1, 2005.

[33] Y. Qi, Y. Fan, B. Gao, Y. Mengzhuo, A. Jadoon, Y. Peng, and T. Jie, "Study on the propagation characteristics of partial discharge in switchgear based on near-field to far-field transformation," *Energies*, vol. 11, no. 7, 2018.

[34] M. Sadiku, *Elements of Electromagnetics*. Oxford University Press, 2007.

[35] C. A. Balanis, *Antenna theory: analysis and design*. John Wiley Sons, 2016.

[36] K. Lonngren and S. Savov, *Fundamentals of Electromagnetics with MATLAB*. SciTech Publishing, 2005.

[37] T. Johnson, "The larmor formula," tech. rep., KTH Royal Institute of Technology in Stockholm, 2017.

[38] Y. Shibuya, S. Matsumoto, M. Tanaka, H. Muto, and Y. Kaneda, "Electromagnetic waves from partial discharges and their detection using patch antenna," *IEEE Transactions on Dielectrics and Electrical Insulation*, vol. 17, no. 3, pp. 862–871, 2010.

[39] J. S. Stratton, *Electromagnetic theory*. Electromagnetic theory, 2007.

[40] H. Guo, H. Qiu, L. Yao, F. Huang, and K. F. Ren, "Investigation on polarization characteristics of pd-induced electromagnetic wave leakage in gis with metal belt," *IEEE Transactions on Dielectrics and Electrical Insulation*, vol. 23, no. 3, pp. 1475–1481, 2016.

[41] M. D. Judd, O. Farish, and B. F. Hampton, "The excitation of uhf signals by partial discharges in gis," *IEEE Transactions on Dielectrics and Electrical Insulation*, vol. 3, no. 2, pp. 213–228, 1996.

[42] T. Li, J. Pan, X. Li, X. Pang, C. Gu, M. Rong, and X. Wang, "The optimal circumferential angle position of uhf sensor for partial discharge detection in gis," in *2016 IEEE International Conference on High Voltage Engineering and Application (ICHVE)*, pp. 1–4, 2016.

[43] W. A. Putro, K. Nishigouchi, U. Khayam, M. Kozako, M. Hikita, K. Urano, and C. Min, "Sensitivity verification and determination of the best location of external uhf sensors for pd measurement in gis," in *2012 IEEE International Conference on Condition Monitoring and Diagnosis*, pp. 698–701, 2012.

[44] T. Li, X. Wang, C. Zheng, D. Liu, and M. Rong, "Investigation on the placement effect of uhf sensor and propagation characteristics of pd-induced electromagnetic wave in gis based on fdtd method," *IEEE Transactions on Dielectrics and Electrical Insulation*, vol. 21, no. 3, pp. 1015–1025, 2014.

[45] S. Okabe, S. Yuasa, S. Kaneko, M. Yoshimura, H. Muto, H. Yoshiyasu, C. Nishida, and M. Kamei, "Simulation of propagation characteristics of higher order mode electromagnetic waves in gis," *IEEE Transactions on Dielectrics and Electrical Insulation*, vol. 13, no. 4, pp. 855–861, 2006.

[46] S. Okabe, S. Yuasa, S. Kaneko, M. Yoshimura, H. Muto, H. Yoshiyasu, C. Nishida, and M. Kamei, "Simulation of propagation characteristics of higher order mode electromagnetic waves in gis," *IEEE Transactions on Dielectrics and Electrical Insulation*, vol. 13, no. 4, pp. 855–861, 2006.

[47] M. Hikita, S. Ohtsuka, T. Teshima, S. Okabe, and S. Kaneko, "Examination of electromagnetic mode propagation characteristics in straight and l-section gis model using fd-td analysis," *IEEE Transactions on Dielectrics and Electrical Insulation*, vol. 14, no. 6, pp. 1477–1483, 2007.

[48] X. Wang, T. Li, D. Ding, and M. Rong, "The influence of l-shaped structure on partial discharge radiated electromagnetic wave propagation in gis," *IEEE Transactions on Plasma Science*, vol. 42, no. 10, pp. 2536–2537, 2014.

[49] T. Li, M. Rong, D. Liu, and X. Wang, "Study on propagation characteristics of partial discharge-induced uhf signal in gis with l shaped structure," in *2013 2nd International Conference on Electric Power Equipment - Switching Technology (ICEPE-ST)*, pp. 1–4, 2013.

[50] T. Li, M. Rong, X. Wang, and J. Pan, "Experimental investigation on propagation characteristics of pd radiated uhf signal in actual 252 kv gis," *Energies*, vol. 10, no. 7, 2017.

[51] M. Hikita, S. Ohtsuka, J. Wada, S. Okabe, T. Hoshino, and S. Maruyama, "Propagation properties of pd-induced electromagnetic wave in 66 kv gis model tank with l branch structure," *IEEE Transactions on Dielectrics and Electrical Insulation*, vol. 18, no. 5, pp. 1678–1685, 2011.

[52] M. Hikita, S. Ohtsuka, T. Hoshino, S. Maruyama, G. Ueta, and S. Okabe, "Propagation properties of pd-induced electromagnetic wave in gis model tank with t branch structure," *IEEE Transactions on Dielectrics and Electrical Insulation*, vol. 18, no. 1, pp. 256–263, 2011.

[53] R. Collin, *Foundations for Microwave Engineering*. Wiley-IEEE Press, 2_{nd} ed., 2001.

[54] T. Li, M. Rong, and X. Wang, "The influence of t-shaped structure on partial discharge radiated electromagnetic wave propagation in gis," in *TENCON 2015 - 2015 IEEE Region 10 Conference*, pp. 1–4, 2015.

[55] M. RONG, T. LI, X. WANG, D. LIU, and A. ZHANG, "Investigation on propagation characteristics of pd-induced electromagnetic wave in t-shaped gis based on fdtd method," *IEICE Transactions on Electronics*, vol. E97.C, no. 9, pp. 880–887, 2014.

[56] X. Hu, M. D. Judd, and W. H. Siew, "A study of pd location issues in gis using fdtd simulation," in *45th International Universities Power Engineering Conference UPEC2010*, pp. 1–5, 2010.

[57] M. Yoshimura, H. Muto, C. Nishida, M. Kamei, S. Okabe, and S. Kaneko, "Propagation properties of electromagnetic wave through t-branch in gis," *IEEE Transactions on Dielectrics and Electrical Insulation*, vol. 14, no. 2, pp. 328–333, 2007.

[58] S. Kaneko, S. Okabe, M. Yoshimura, H. Muto, C. Nishida, and M. Kamei, "Partial discharge diagnosis method using electromagnetic wave mode transformation in actual gis structure," *IEEE Transactions on Dielectrics and Electrical Insulation*, vol. 15, no. 5, pp. 1329–1339, 2008.

[59] S. Okabe, G. Ueta, H. Hama, T. Ito, M. Hikita, and H. Okubo, "New aspects of uhf pd diagnostics on gas-insulated systems," *IEEE Transactions on Dielectrics and Electrical Insulation*, vol. 21, no. 5, pp. 2245–2258, 2014.

[60] S. Okabe, S. Kaneko, M. Yoshimura, H. Muto, C. Nishida, and M. Kamei, "Partial discharge diagnosis method using electromagnetic wave mode transformation in gas insulated switchgear," *IEEE Transactions on Dielectrics and Electrical Insulation*, vol. 14, no. 3, pp. 702–709, 2007.

[61] D. Cheng, *Field and Wave Electromagnetics*. Pearson Education and Tsinghua University Press, 2_{nd} ed., 2006.

[62] T. Li, M. Rong, and X. Wang, "Experimental investigation on uhf partial discharge sensor in gis," in *2015 3rd International Conference on Electric Power Equipment – Switching Technology (ICEPE-ST)*, pp. 46–49, 2015.

[63] M. Shi, X. Han, X. Zhang, Z. Zhang, and J. Li, "Effect of disconnector and high-voltage conductor on propagation characteristics of pd-induced uhf signals," *High Voltage*, vol. 3, no. 3, pp. 187–192, 2018.

[64] X. Li, X. Wang, D. Xie, X. Wang, A. Yang, and M. Rong, "Time–frequency analysis of pd-induced uhf signal in gis and feature extraction using invariant moments," *IET Science, Measurement & Technology*, vol. 12, no. 2, pp. 169–175, 2018.

[65] M. Hikita, S. Ohtsuka, S. Okabe, J. Wada, T. Hoshino, and S. Maruyama, "Influence of disconnecting part on propagation properties of pd-induced electromagnetic wave in model gis," *IEEE Transactions on Dielectrics and Electrical Insulation*, vol. 17, no. 6, 2010.

[66] T. Li, M. Rong, D. Liu, X. Wang, and J. Wu, "Experimental research on partial discharge radiated uhf signal attenuation characteristics in gis," in *2013 IEEE International Conference of IEEE Region 10 (TENCON 2013)*, pp. 1–4, 2013.

[67] K. Kaiser, *Transmission Lines, Matching, and Crosstalk*. Broken Sound Parkway, NW, Taylor and Francis, 2006.

[68] M. Hikita, "Fundamental principles and application of diagnosis for gis using partial discharge measurements," in *Proceedings of the 2011 International Conference on Electrical Engineering and Informatics*, pp. 1–6, 2011.

[69] M. Talaat, A. El-Zein, and M. Amin, "Developed optimization technique used for the distribution of u-shaped permittivity for cone type spacer in gis," *Electric Power Systems Research*, vol. 163, pp. 754–766, 2018. Advances in HV Transmission Systems.

[70] A. Cookson, "Review of high-voltage gas breakdown and insulators in compressed gas," in *IEE Proceedings A - Physical Science, Measurement and Instrumentation, Management and Education - Reviews*, vol. 128, pp. 303–312, 1981.

[71] V. Maller and M. Naidu, *Advances in High Voltage Insulation and Arc Interruption in SF6 and Vacuum*. Pergamon Press, 1981.

[72] S. Okabe, G. Ueta, T. Utsumi, and J. Nukaga, "Insulation characteristics of gis insulators under lightning impulse with dc voltage superimposed," *IEEE Transactions on Dielectrics and Electrical Insulation*, vol. 22, no. 6, pp. 1–9, 2015.

[73] M. Sawada, K. Omori, S. Isejima, S. Ohtsuka, H. Ikeda, M. Hikita, G. Ueta, S. Okabe, T. Hoshino, S. Maruyama, and T. Sakakibara, "Influence of metal flange cover of insulation spacers on propagation properties of pd-induced electromagnetic wave in gis," in *2008 International Conference on Condition Monitoring and Diagnosis*, pp. 437–442, 2008.

[74] G. Behrmann, K. Wyss, J. Weiss, M. Schraudolph, S. Neuhold, and J. Smajic, "Signal delay effects of solid dielectrics on time-of-flight measurements in gis," *IEEE Transactions on Dielectrics and Electrical Insulation*, vol. 23, no. 3, pp. 1275–1284, 2016.

[75] S. Kaneko, S. Okabe, M. Yoshimura, H. Muto, C. Nishida, and M. Kamei, "Detecting characteristics of various type antennas on partial discharge electromagnetic wave radiating through insulating spacer in gas insulated switchgear," *IEEE Transactions on Dielectrics and Electrical Insulation*, vol. 16, no. 5, pp. 1462–1472, 2009.

[76] S. Kaneko, S. Okabe, H. Muto, M. Yoshimura, C. Nishida, and M. Kamei, "Electromagnetic wave radiated from an insulating spacer in gas insulated switchgear with partial discharge detection," *IEEE Transactions on Dielectrics and Electrical Insulation*, vol. 16, no. 1, pp. 60–68, 2009.

[77] N. Behdad and K. Sarabandi, "Dual resonant slot antennas for wireless applications," in *IEEE Antennas and Propagation Society Symposium, 2004.*, vol. 2, pp. 1931–1934 Vol.2, 2004.

[78] Y. Wang, Z. Wang, and J. Li, "Uhf moore fractal antennas for online gis pd detection," *IEEE Antennas and Wireless Propagation Letters*, vol. 16, pp. 852–855, 2017.

[79] Tang Ju, Xu Zhongrong, Zhang Xiaoxing, and Sun Caixin, "Gis partial discharge quantitative measurements using uhf microstrip antenna sensors," in *2007 Annual Report - Conference on Electrical Insulation and Dielectric Phenomena*, pp. 116–119, 2007.

[80] A. N. Darwish, A. Zakaria, N. Qaddoumi, and L. Albasha, "Low-cost microwave security camera system," in *2016 16th Mediterranean Microwave Symposium (MMS)*, pp. 1–4, 2016.

[81] W. Stutzman and G. Thiele, *Antenna Theory and Design*. John Wiley and Sons, 3_{rd} ed., 2013.

[82] R. Alkadi, A. Shaath, F. Gefe, S. Jaber, N. A. Rayes, A. H. El-Hag, and N. Qaddoumi, "Smart antenna-based partial discharge detection and classification system," in *2016 16th Mediterranean Microwave Symposium (MMS)*, pp. 1–4, 2016.

[83] W. Yawei, W. Gaungming , and L. Jiangang, "Spiral antenna cuts low profile to 9.4 ghz," in *Microwaves and RF*, vol. 51, 2012.

[84] J. Li, T. Jiang, C. Cheng, and C. Wang, "Hilbert fractal antenna for uhf detection of partial discharges in transformers," *IEEE Transactions on Dielectrics and Electrical Insulation*, vol. 20, no. 6, pp. 2017–2025, 2013.

[85] J. Li, P. Wang, T. Jiang, L. Bao, and Z. He, "Uhf stacked hilbert antenna array for partial discharge detection," *IEEE Transactions on Antennas and Propagation*, vol. 61, no. 11, pp. 5798–5801, 2013.

[86] F. Bin, F. Wang, Q. Sun, S. Lin, Y. Xie, and M. Fan, "Internal uhf antenna for partial discharge detection in gis," *IET Microwaves, Antennas & Propagation*, vol. 12, no. 14, pp. 2184–2190, 2018.

[87] T. Li, M. Rong, C. Zheng, and X. Wang, "Development simulation and experiment study on uhf partial discharge sensor in gis," *IEEE Transactions on Dielectrics and Electrical Insulation*, vol. 19, no. 4, pp. 1421–1430, 2012.

[88] M. Hikita, S. Ohtsuka, T. Teshima, S. Okabe, and S. Kaneko, "Electromagnetic (em) wave characteristics in gis and measuring the em wave leakage at the spacer aperture for partial discharge diagnosis," *IEEE Transactions on Dielectrics and Electrical Insulation*, vol. 14, no. 2, pp. 453–460, 2007.

[89] T. Hoshino, S. Maruyama, S. Ohtsuka, M. Hikita, J. Wada, and S. Okabe, "Sensitivity comparison of disc- and loop-type sensors using the uhf method to detect partial discharges in gis," *IEEE Transactions on Dielectrics and Electrical Insulation*, vol. 19, no. 3, pp. 910–916, 2012.

[90] Jia-Ning Zhang, Ming-Xiao Zhu, Qing Liu, Xian-Jun Shao, Wen-Lin He, Hui Yao, Jun-Bo Deng, and Guan-Jun Zhang, "Design and development of internal uhf sensor for partial discharge detection in gis," in *2016 International Conference on Condition Monitoring and Diagnosis (CMD)*, pp. 709–712, 2016.

[91] A. M. Ishak, M. T. Ishak, M. T. Jusoh, S. F. Syed Dardin, and M. D. Judd, "Design and optimization of uhf partial discharge sensors using fdtd modeling," *IEEE Sensors Journal*, vol. 17, no. 1, pp. 127–133, 2017.

[92] T. Hoshino, S. Maruyama, and T. Sakakibara, "Simulation of propagating electromagnetic wave due to partial discharge in gis using fdtd," *IEEE Transactions on Power Delivery*, vol. 24, no. 1, pp. 153–159, 2009.

[93] L. Niemeyer, "A generalized approach to partial discharge modeling," *IEEE Transactions on Dielectrics and Electrical Insulation*, vol. 2, no. 4, pp. 510–528, 1995.

[94] G. Crichton, P. Karlsson, and A. Pedersen, "Partial discharges in ellipsoidal and spheroidal voids," *IEEE Transactions on Electrical Insulation*, vol. 24, no. 2, pp. 335–342, 1989.

[95] G. Behrmann, S. Franz, J. Smajic, Z. Tanasic, and R. Christen, "Uhf pd signal transmission in gis: Effects of 90° bends and an l-shaped cigre step 1 test section," *IEEE Transactions on Dielectrics and Electrical Insulation*, vol. 26, no. 4, pp. 1293–1300, 2019.

[96] A. Darwish, S. S. Refaat, H. A. Toliyat, and H. Abu-Rub, "On the electromagnetic wave behavior due to partial discharge in gas insulated switchgears: State-of-art review," *IEEE Access*, vol. 7, pp. 75822–75836, 2019.

[97] C. Zachariades, R. Shuttleworth, and R. Giussani, "A dual-slot barrier sensor for partial discharge detection in gas-insulated equipment," *IEEE Sensors Journal*, vol. 20, no. 2, pp. 860–867, 2020.

[98] M. M. O. Harbaji, A. H. Zahed, S. A. Habboub, M. A. AlMajidi, M. J. Assaf, A. H. El-Hag, and N. N. Qaddoumi, "Design of hilbert fractal antenna for partial discharge classification in oil-paper insulated system," *IEEE Sensors Journal*, vol. 17, no. 4, pp. 1037–1045, 2017.

[99] A. Wadi, W. Al-Masri, W. Siyam, M. F. Abdel-Hafez, and A. H. El-Hag, "Accurate estimation of partial discharge location using maximum likelihood," *IEEE Sensors Letters*, vol. 2, no. 4, pp. 1–4, 2018.

[100] T. F. Cigre, "Partial discharge detection system for gis: Sensitivity verification for the uhf method and the acoustic method," *Electra*, vol. 183, pp. 75–87, 1999.

[101] U. Schichler, W. Koltunowicz, D. Gautschi, A. Girodet, H. Hama, K. Juhre, J. Lopez-Roldan, S. Okabe, S. Neuhold, C. Neumann, J. Pearson, R. Pietsch, U. Riechert, and S. Tenbohlen, "Uhf partial discharge detection system for gis: Application guide for sensitivity verification: Cigre wg d1.25," *IEEE Transactions on Dielectrics and Electrical Insulation*, vol. 23, no. 3, pp. 1313–1321, 2016.

[102] A. M. Ishak, P. C. Baker, W. H. Siew, and M. D. Judd, "Characterizing the sensitivity of uhf partial discharge sensors using fdtd modeling," *IEEE Sensors Journal*, vol. 13, no. 8, pp. 3025–3031, 2013.

[103] M. Siegel, S. Coenen, M. Beltle, S. Tenbohlen, M. Weber, P. Fehlmann, S. M. Hoek, U. Kempf, R. Schwarz, T. Linn, and J. Fuhr, "Calibration proposal for uhf partial discharge measurements at power transformers," *Energies*, vol. 12, no. 16, 2019.

[104] C. Zachariades, R. Shuttleworth, R. Giussani, and T.-H. Loh, "A wideband spiral uhf coupler with tuning nodules for partial discharge detection," *IEEE Transactions on Power Delivery*, vol. 34, no. 4, pp. 1300–1308, 2019.

[105] T. Zhao, M. Judd, and B. G. Stewart, "Attenuation characteristics and time delay of pd electromagnetic wave propagation in gis systems," *IEEE Transactions on Power Delivery*, pp. 1–1, 2021.

[106] J. Li, T. Jiang, C. Wang, and C. Cheng, "Optimization of uhf hilbert antenna for partial discharge detection of transformers," *IEEE Transactions on Antennas and Propagation*, vol. 60, no. 5, pp. 2536–2540, 2012.

[107] L. Yang, N. Ito, C. W. Domier, N. C. Luhmann, and A. Mase, "18–40-ghz beam-shaping/steering phased antenna array system using fermi antenna," *IEEE Transactions on Microwave Theory and Techniques*, vol. 56, no. 4, pp. 767–773, 2008.

[108] A. T. Mobashsher and A. Abbosh, "Utilizing symmetry of planar ultra-wideband antennas for size reduction and enhanced performance," *IEEE Antennas and Propagation Magazine*, vol. 57, no. 2, pp. 153–166, 2015.

[109] S.-S. Zhong, X.-L. Liang, and W. Wang, "Compact elliptical monopole antenna with impedance bandwidth in excess of 21:1," *IEEE Transactions on Antennas and Propagation*, vol. 55, no. 11, pp. 3082–3085, 2007.

[110] W. J. K. Raymond, H. A. Illias, A. H. A. Bakar, and H. Mokhlis, "Partial discharge classifications: Review of recent progress," *Measurement*, vol. 68, pp. 164–181, 2015.

[111] X. Peng, F. Yang, G. Wang, Y. Wu, L. Li, Z. Li, A. A. Bhatti, C. Zhou, D. M. Hepburn, A. J. Reid, M. D. Judd, and W. H. Siew, "A convolutional neural network-based deep learning methodology for recognition of partial discharge patterns from high-voltage cables," *IEEE Transactions on Power Delivery*, vol. 34, no. 4, pp. 1460–1469, 2019.

[112] J. Brownlee, "Tour of evaluation metrics for imbalanced classification," 2020.

[113] J. Li, T. Jiang, S. Grzybowski, and C. Cheng, "Scale dependent wavelet selection for denoising of partial discharge detection," *IEEE Transactions on Dielectrics and Electrical Insulation*, vol. 17, no. 6, pp. 1705–1714, 2010.

[114] F. Pedregosa, G. Varoquaux, A. Gramfort, V. Michel, and B. Thirion, "Scikit-learn: Machine learning in python," *Journal of Machine Learning Research*, vol. 12, pp. 2825–2830, 2011.

[115] F. Chollet, "Keras," 2015.

[116] M. Massaoudi, A. Darwish, S. S. Refaat, H. Abu-Rub, and H. A. Toliyat, "Uhf partial discharge localization in gas-insulated switchgears: Gradient boosting based approach," in *2020 IEEE Kansas Power and Energy Conference (KPEC)*, pp. 1–5, 2020.

[117] K. X. Lai, B. T. Phung, T. R. Blackburn, and N. A. Muhamad, "Classification of partial discharge using pca and som," in *2007 International Power Engineering Conference (IPEC 2007)*, pp. 1311–1316, 2007.

APPENDIX A

IMPACT OF DIMENSIONALITY-REDUCTION TECHNIQUES ON THE CLASSIFICATION ACCURACY OF PD DEFECTS IN DISK-CERAMIC INSULATORS*

UHF-based testing of disc ceramic insulators has been predominantly used to detect and classify PD defects. The initiated electromagnetic waves due to PD currents can be captured using UHF antennas. In this chapter, three ceramic insulator defects, namely corona discharge, cracks on insulator, and voids, are classified using machine learning (ML) techniques. The classification accuracies are presented with and without the use of two-dimensionality reduction techniques, i.e., principal component analysis (PCA) and recursive feature elimination (RFE). A total of 322 signals were obtained from laboratory tests using a wideband Horn antenna. Then, wavelet decomposition was applied to the obtained signals, and some statistical features, which were fed to the ML algorithms, were obtained at each decomposition level. Four score metrics are used for the classification, namely accuracy, precision, recall, and f1-score. Recall (sensitivity) and f1-score are essential metrics when dealing with imbalanced data. It has been shown that although PCA is very efficient in reducing the number of input features, it reduces the classification score metrics. This is attributed to the loss of important information associated with the use of PCA. On the other hand, RFE does not have a significant impact on the different score metrics. In other words, the impact of feature selection (RFE) and feature extraction (PCA) on the classification metrics is discussed and analyzed in this chapter of the thesis.

A.1 General Overview

Generated PD pulses can be classified based on the different sources of defects on the power apparatuses. Various machine learning (ML) models have been built to localize and classify PD defects for different medium and high voltage devices. To obtain accurate prediction of PD classes,

*Reprinted with permission from "Impact of Dimensionality Reduction Techniques on the Classification of Ceramic Insulators Defects" by A. Darwish, A. H. El-Hag, S. S. Refaat, H. A. Toliyat and H. Abu-Rub, 2021. Conference on Electrical Insulation and Dielectric Phenomena (CEIDP), copyright [2021] by IEEE.

different ML techniques have been proposed in the literature. Such techniques include the integration of classifiers such as support vector machine (SVM), artificial neural network (ANN), and random forest, in addition to some deep networks including convolutional neural networks (CNN) [110, 111].

In this chapter, three different PD types are obtained and used for the classification. Corona discharge (225 samples), cracks in insulators (85 samples), and voids inside the disc insulators (12 samples) comprise the utilized dataset. Dealing with imbalanced data requires using the f1-score metric since it provides an equal balance between precision and recall (sensitivity), which is considered an important metric when dealing with imbalanced data [112]. Thus, the main contributions of this chapter are:

- Studying the impact of integrating two dimensionality reduction techniques with the ML algorithms on classification accuracy, precision, recall, and f1-score.
- Examining the performance of four ML techniques namely ANN, SVM, random forest (RF), and adaptive boosting (AdaBoost) on classifying PD based disc insulators defects.

A.2 Methodology

Figure A.1 shows the flowchart of the proposed PD classification approach, which was initially performed using the dataset without any dimensionality reduction techniques. After that, RFE and PCA were used to reduce the input feature dimensions. The four classification metrics were computed for the different scenarios, and results are represented and discussed in the next section.

A.2.1 Experimental Setup

Three different defective disc insulators comprise the test samples used in the experiment. The first class is the internal discharge produced by creating a hole through the cap of the ceramic insulator. A cracked disc insulator is used as the 2nd class of defects. Corona discharge, obtained using sharp points, comprises the 3rd defective class. Such defects arise either during the manufacturing of the insulators or due to the exposition of high electrical and mechanical stresses when they are

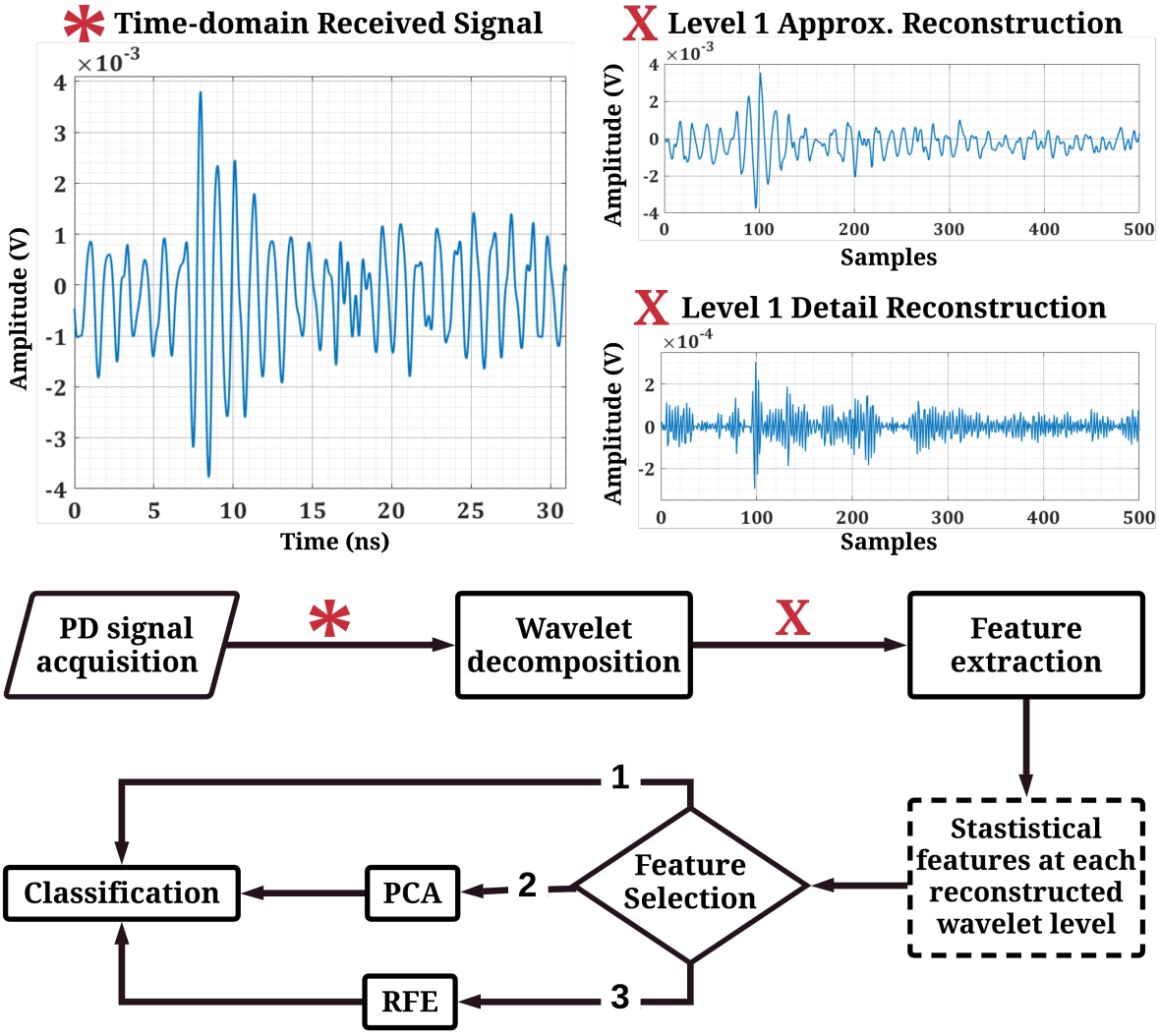

Figure A.1: Flowchart of the used classification techniques.

in service. The dataset used in this chapter is imbalanced since there exists a large discrepancy between the obtained number of samples for the corona (225 samples), cracks (85 samples), and internal discharges (12 samples). In addition, healthy data is not utilized since there are no associated UHF PD signals. This is because PD signals are generated due to the current pulses associated with PD activities.

Raw UHF PD signals are captured using a wideband horn antenna. The antenna is connected to a wideband oscilloscope to acquire the captured UHF signals. To initiate PD defects, samples

are connected to a $300kV$ test transformer at the pin (lower part) and grounded at the cap (upper part). A maximum applied voltage of $13kV_{rms}$ is used to conduct the experiments. Figure A.2 shows the experimental setup used to initiate and acquire the PD signals.

A.2.2 Feature Extraction

After obtaining the UHF signals, discrete wavelet transform (WT) was applied to obtain the decomposed levels. Each input signal is decomposed to five different levels using the Daubechies mother wavelet. A comparative study on the correlation between the original signal and the decomposed outputs was initially performed using Db-2 to Db-6 and revealed that Db-4 achieved the highest correlation [113]. Then, the decomposed layers were reconstructed using the obtained wavelet coefficients.

The obtained PD signals were considered in terms of the following features: maximum voltage amplitude, minimum voltage amplitude, average power, variance, kurtosis, skewness, and cumula-

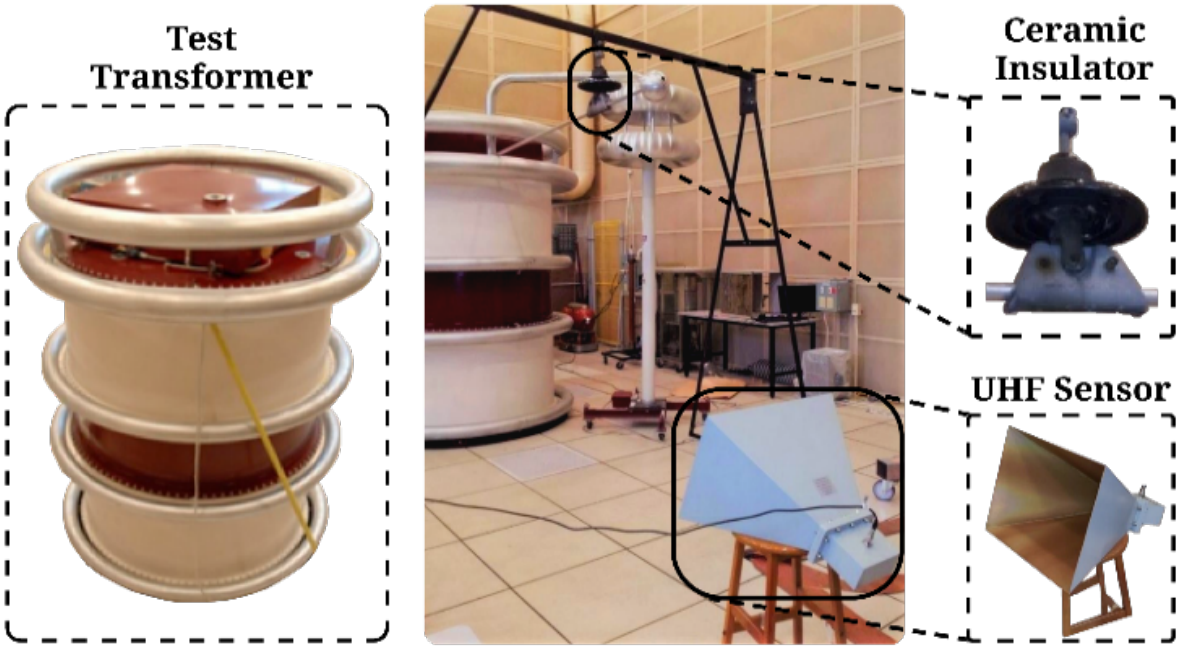

Figure A.2: UHF PD signals acquisition setup. The UHF horn antenna is connected to the digital oscilloscope via a 50Ω coaxial cable.

tive energy. The reason for choosing these seven features is related to the significant discrepancies found on these features between the three defect classes, as shown and discussed in section 6.3. These features were obtained for the original signals and the approximate (app) and detail reconstructed signals at each wavelet-decomposed layer. Thus, a total of 77 different features were initially chosen for the classification.

To study the impact of the dimensionality reduction techniques on the classification, RFE and PCA were used. The impact of deploying PCA and RFE will be discussed in the next section.

A.2.3 Machine Learning

After the extraction of the input features, four ML algorithms were used to train and test the data, namely ANN, SVM, random forest, and AdaBoost [114, 115]. The reason for choosing these ML techniques is that they have been used in PD classification and localization and showed high levels of effectiveness [116, 117]. 10-fold cross-validation is used to obtain the classification metrics due to the limited amount of utilized data. This ensures that the obtained classification metrics are not biased.

To choose the optimal hyperparameters, the "GridSearchCV," an exhaustive search technique in Scikit-learn library over specified values of parameters, was used [115]. The features were initially preprocessed through the random shuffling and scaling of the dataset using features standardization. The used ANN has an input layer, two hidden layers, and an output layer. The number of hidden layers was chosen such that deep learning (more than three layers other than the input later) is avoided since deep learning requires larger data sets. ANN is used due to the simplicity of implementation and the robust performance exhibited by such ML techniques in classifying PD defects. The number of layers has been defined based on a predefined search space with the grid search method. Then, the number of layers was decided by choosing that with the highest obtained accuracy. The classification results are obtained using PYTHON programming language in a Windows 7 system, Intel (R) Core (TM) i7-7700HQ CPU, and a memory size of 16 GB.

A.3 Results and Discussion

Figure A.3 shows typical UHF PD signals for the three different defects, i.e., internal void, cracks on insulator surface, and corona discharge. It can be seen that the internal discharge has

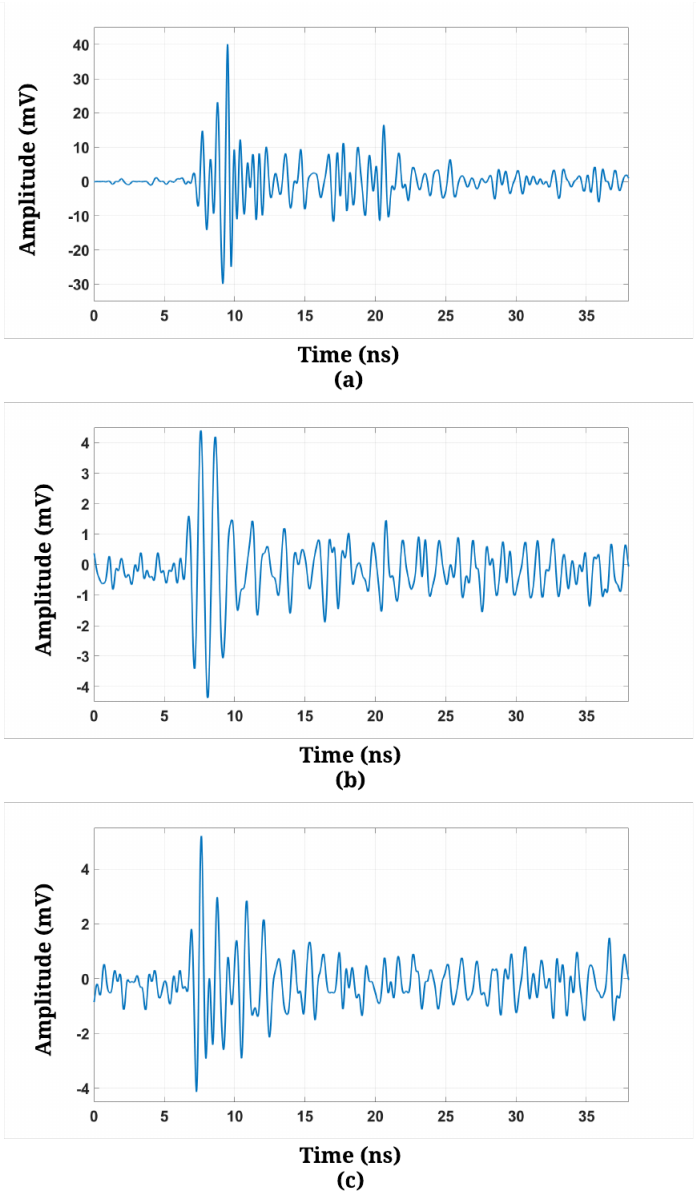

Figure A.3: Typical UHF PD signals for a) Internal void, b) Cracks on insulator, c) Corona discharge.

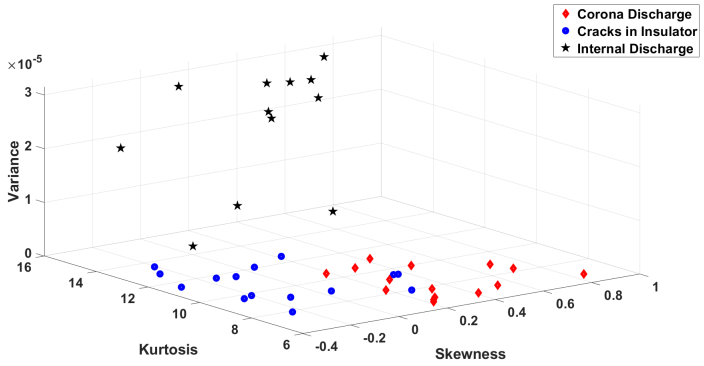

Figure A.4: 3D Visualization of the three PD defects against skewness (x-axis), kurtosis (y-axis), and variance (z-axis).

higher maximum and minimum voltages as compared with the other two defects. Such a significant difference in the amplitude also affects the total cumulative energy and the average power received by the UHF antenna for the different defects. On the other hand, by comparing the cracks on insulator and corona discharges, the former's attenuation is faster than the latter, causing a significant discrepancy on the features mentioned above. Figure A.4 shows a visualization of the three defects against the variance, kurtosis, and skewness. It can also be seen that the three different defects can be easily classified or clustered into different categories, although some points overlap. Using the seven features, an accuracy of more than 96% was achieved using both ANN and SVM. Thus, the number of statistical features used in this study was limited to the discussed features.

Table A.1 shows the obtained accuracy, precision, recall, and f1-score using the four ML algorithms. Results validate that wavelet decomposition along with the statistical parameters is an effective tool to obtain distinct features. The score metrics were obtained by taking the average of running each ML algorithm 20 times to ensure that the obtained results are not biased. F1-score is an important metric when dealing with imbalanced datasets since it combines the significance of both precision and recall.

On the other hand, the use of RFE did not significantly impact the score metrics in any of the ML algorithms, as depicted in Table A.1. The use of RFE has reduced the number of features to 69. Table A.2 shows the features that were dropped allaying the use of RFE. Finally, the utilized

Table A.1: Summary of the ML Results

Without RFE and PCA				
ML Technique	**Accuracy**	**Precision**	**Recall**	**F-Score**
ANN	96.25%	96.62%	95.34%	95.54%
SVM	96.56%	93.83%	94.43%	93.98%
Random Forest	93.41%	92.40%	91.09%	91.55%
AdaBoost	91.25%	91.59%	90.04%	90.34%
RFE				
ML Technique	**Accuracy**	**Precision**	**Recall**	**F-Score**
ANN	97.18%	97.02%	95.65%	96.03%
SVM	96.49%	93.38%	94.32%	93.74%
Random Forest	91.98%	91.80%	91.47%	91.35%
AdaBoost	94.38%	92.82%	91.19%	91.76%
PCA				
ML Technique	**Accuracy**	**Precision**	**Recall**	**F-Score**
ANN	93.44%	92.25%	89.71%	90.41%
SVM	95.05%	91.85%	93.02%	92.15%
Random Forest	87.88%	74.99%	68.90%	70.55%
AdaBoost	84.69%	83.46%	77.34%	78.99%

Table A.2: Dropped RFE Features

Level	**Category**	**Feature**	**Level**	**Category**	**Feature**
1	app	kurtosis	4	app	energy
2	app	Min. Voltage	4	app	skewness
2	app	skewness	4	detail	energy
2	app	kurtosis	5	app	skewness

PCA retained 95% of the variance and reduced the input features from 77 to 14. Nonetheless, a reduction in all score metrics can be observed.

Utilizing RFE did not significantly impact the score metrics since RFE caused a minor vector feature reduction on the input dataset (77 to 69). It improved the accuracy and f1-score for ANN and AdaBoost since RFE reduces any potential overfitting in the dataset. On the other hand, PCA caused a degradation in the accuracy of the different ML algorithms due to the loss of important information associated with reducing the number of features. This is because PCA might sometimes drop principal components (PC) that are important for distinguishing the different classes if such PC contributes to a minimum variance. Also, since the utilized PCA retained 95% of the variance, a reduction in the precision and recall, and thus, on f1-score can also be perceived.

A.4 Conclusion

In this chapter, the classification of three different defects in ceramic insulators has been carried out. The classification utilized two dimensionality-reduction techniques: principal component analysis and recursive feature elimination to investigate their impact on imbalanced datasets. The following remarks are concluded:

- The use of wavelet decomposition and statistical parameters can provide distinct features to obtain high classification accuracy.
- Although RFE might not largely reduce the number of input features, utilizing such technique can improve the classification score metrics since such technique can reduce overfitting.
- PCA degrades the classification score metrics when dealing with imbalanced datasets since it has a large impact on the precision and recall, and thus, the f1-score.